Inorganic lone pair materials for photovoltaic applications

Matthew James Smiles

A thesis presented for the degree of
Doctor of Philosophy

Department of Physics
University of Liverpool
September 2022

Abstract

The GeS_xSe_{1-x} and $Sb_2(S_xSe_{1-x})_3$ alloy series are explored with a focus on the implications for photovoltaic application. These are earth-abundant materials with stereochemically active lone pairs and high optical absorption that have the potential to make thin film solar cells with shorter energy payback times than silicon-based solar technologies. Bulk crystals of nine compositions have been grown for each alloy series and the bulk crystals have been used as source material for thin film depositions.

The thermal, structural and optical properties of the GeS_xSe_{1-x} alloy series are investigated. The melting point is shown to bow between 665°C and 647°C for GeSe and GeS, respectively, with the minimum at $GeS_{0.766}Se_{0.234}$. The lattice parameters decreased linearly with S-content, whereas the band gap is shown to increase linearly between 1.30 eV and 1.64 eV for GeSe and GeS, respectively. Both lattice parameter and band gap changes show good agreement when compared to density functional theory (DFT) calculations. This includes a specific case study correcting the GeSe band gap values reported in the literature, which involved low temperature band gap measurements that show excellent agreement with the highest level of DFT at 1.33 eV.

Photoemission spectroscopy is used to study GeS and GeSe. Ionisation potentials of 5.74 and 5.48 eV are measured for GeS and GeSe which, with previous band gap measurements, are used to show, from a band alignment perspective, both TiO_2 and CdS are viable choices for window layers in a solar cell. Furthermore, in conjunction with DFT, photoemission measurements are used to show the presence of the Ge 4s orbital at the valence band maximum, thus providing evidence for active lone pairs in both GeS and GeSe.

The incorporation of silver as a dopant in GeSe is investigated and shown to increase the hole density from $5.2\times10^{15}\text{cm}^{-3}$ to $1.6\times10^{16}\text{cm}^{-3}$. Using both the undoped and Ag-doped GeSe as source materials for devices, it is found that the highest power conversion efficiency of 0.260% is achieved using undoped GeSe with an Sb_2Se_3 interfacial layer.

Finally, a systematic study of the lattice parameters of $Sb_2(S_xSe_{1-x})_3$ shows that the lattice parameter decreases linearly as S-content increases. The band gap varies across the series according to $E_g(x) = 1.707x + 1.191(1\text{-}x) - 0.237x(1\text{-}x)$. Both show reasonable agreement when compared with DFT. The Kraut method of the valence band offset measurement is used to show CdS is a better window layer than TiO_2 for $Sb_2(S_xSe_{1-x})_3$ from a band alignment perspective.

These results improve our understanding of the properties of these lone pair chalcogenide materials for use as absorber layers in a photovoltaic cell.

Declaration

All measurements, analysis and interpretation presented in this thesis were carried out by the author apart from the following, separated by institution:

Stephenson Institute for Renewable Energy, University of Liverpool:

1. Chris J. Gannon who assisted in making five films for Chapter 4
2. Philip A. E. Murgatroyd who helped perform the measurements and analysis of the GeSe band gap in Chapter 4
3. Theodore D. C. Hobson who assisted in the preparation of samples for ICP-OES in Chapters 4, 5 and 6
4. Oliver S. Hutter who assisted in the preparation of samples for ICP-OES in Chapter 4
5. Leanne A. H. Jones, Huw Shiel, Jack E. N. Swallow, Holly Edwards, Thomas Featherstone and Chris Don took part in beam times as well as assisting in taking XPS measurements for Chapters 5 and 6
6. Thomas P. Shalvey deposited the TiO_2 and Sb_2Se_3 layers in Chapter 5 and CdS and TiO_2 layers for Chapter 6
7. Luke Thomas deposited the CdS layer for Chapter 5
8. Tim D. Veal performed the calculations to solve the Poisson equation for Chapter 5
9. Jonathan D. Major performed and analysed the capacitance-voltage measurements in Chapter 5

Other institutions

1. Jonathan M. Skelton from the University of Manchester did the density functional theory calculations for Chapters 4 and 5 (with the exception of the GeSe band gap case study)
2. Christopher N. Savoury from the University College London did the density functional theory calculations for the GeSe band gap case study
3. Seán Kavanagh from Imperial College London did the density functional theory calculations for Chapter 6
4. Pardeep K. Thakur and Tien-Lin Lee from Diamond Light Source helped with hard x-ray photoemission spectroscopy measurements for Chapters 5 and 6

Parts of this work have been published elsewhere:

- P. A. E. Murgatroyd, M. J. Smiles, C. N. Savory *et al.*. GeSe: Optical Spectroscopy and Theoretical Study of a van der Waals Solar Absorber. *Chem. Mater.* 32(7):3245-3253 (2020); DOI:10.1021/acs.chemmater.0c00453
- M. J. Smiles *et al.*. Ge $4s^2$ lone pairs and band alignments in GeS and GeSe for photovoltaics. *J. Mater. Chem. A* 9:22440-22452 (2021); DOI:10.1039/D1TA05955F
- M. J. Smiles *et al.*. GeSe photovoltaics: doping, interfacial layer and devices. *Faraday Discussions*; DOI:10.1039/D2FD00048B

The remaining work on GeS_xSe_{1-x} is currently under review and the work on $Sb_2(S_xSe_{1-x})_3$ is in the process of being prepared for publication.

Acknowledgements

There are a lot of people I need to thank for helping me achieve this PhD. The first is of course my primary supervisor Tim. I consider myself to be incredibly lucky to have had Tim as my supervisor, although anyone that knows the Veal group well knows that his students sometimes have to supervise him. He was brilliant at keeping me on track and helping me adapt my planned work when the pandemic hit. Without doubt his publishing ability is the best I've come across which has helped me get a google scholar profile so thank you for that Tim.

I was lucky enough to work with some of the other excellent academics in the SIRE. I'd like to give a special thanks to Jon Major, Vin Dhanak and Ken Durose who have all helped me out with different aspects of my work throughout. And one of the best things about working in the SIRE is that you get to work with lots of excellent PhD students and postdocs. I won't list exactly what you've all done but these people have all directly helped with this research and I will be forever grateful for all their help. The amazing PhD students and postdocs that helped are Jack, Phil, Leanne, Huw, Shalvey, Holly, Theo, Chris, Nicole, Luke, Oliver and Featherstone.

And though I didn't get to work with all the students in the SIRE for my research, I did get to spend plenty of time with the rest and have lots of great memories with all of them. Along with the above listed people they made me look forward to coming into work every day so thank you to Dan, Alex, Jacob, Joe, Kieran, Laurie, Beanie, Olivia, Rob, Nick and Ollie. And though he wasn't in the SIRE, a thank you to Rob O'Neill for the many lunch time catch ups. I haven't even mentioned any of the chemists from the SIRE and I'm sure I'll have missed someone so if you overlapped with me in the SIRE at any point thank you for making it such a great place to work.

Luke, Jacob and myself had a very unusual first year because we were all members of the CDT-PV. We got to go to six other universities and learn about different areas of PV and see all the amazing PV research going on in the UK. In my cohort, C5, I have made some amazing friends and some great memories. Thank you to the CDT-PV for funding my PhD and inviting me to so many amazing events. And thank you to Luke, Jacob and the rest of C5 for making that first year so enjoyable.

A special thank you also has to go to Huw and Dan, the Birstall Boys. We were all living together during the first lockdown and the two of them kept me sane. It was great to have other PhD students with me helping to keep me motivated. Given what was going on in the world it seems strange to say anything positive about the time, but I hope you both look back on the time as fondly as I do.

Of course I wouldn't have been able to do it without my family. So thank you to Mum, Dad, Ollie, Maddie, Daisy and Roxie. I also need to thank the Condells, the rest of the Smiles's and all the partners. Thank you all for asking about what I was up to and trying to understand it all, even if my explanations weren't always the best. And thank you all for taking up my new found passion for spotting PV.

And finally there's two special people in my life who helped me get through all this. Josh Cavie who is the most amazing friend and got incredibly passionate about all my work. He has proofread all of my papers plus most of this thesis and always does a great job at correcting my writing (he did go to the best school in the country). And then there's my brilliant girlfriend Chelsi Burns. She has listened to me moan about lab equipment not working, worry about how bad my papers are going and my endless lectures about different aspects of my work. I managed to avoid all the difficulties PhD students face because of the support that you offered me. I'll also always remember how happy you were when you first saw my Mario graphs. Thank you for being so great, they do say doctors and nurses make great couples.

Contents

Chapter 1

Introduction

1.1 Need for renewable energy

The greenhouse effect is vital to keeping the Earth warm enough to sustain life. The concept is simple: when sunlight reaches the Earth it is either absorbed and re-radiated as heat or the sunlight is reflected back into space. Greenhouse gases in the atmosphere absorb some of this reflected or re-radiated heat, which can then be radiated once again, keeping some of the heat in the atmosphere. Without this greenhouse effect, it has been predicted that temperatures on Earth would be -19°C, whereas with the greenhouse effect, in the 1850-1900 time period, the average global surface temperature was 13.6°C. [1]

In the Intergovernmental Panel on Climate Change's (IPCC's) sixth report on the physical basis of climate change, it concluded that the average global surface temperature had increased by 1.09°C (0.95-1.10°C) in the decade starting 2010 compared with the previously mentioned period. [2–7] Since the 1970s, this temperature rise has been at 1.7°C per century compared with a decrease of 0.01°C per century in the past 7000 years.

The cause for this could, crudely speaking, be two things: an increase in solar irradiation or more greenhouse gases in the atmosphere. As can be seen in Figure 1.1, evidence suggests that there has been minimal change in solar irradiation in the last 170 years. [8] On the other hand, there is strong evidence for rising concentrations of greenhouse gases during that same time period. Before 1850, the largest known increase in carbon dioxide (CO_2) concentration in the atmosphere was 9.6ppm per century. Since 1850, the CO_2 levels in the atmosphere have risen by around 125ppm. [11–15] Similar unprecedented rises have been shown for other greenhouse gases. [4, 16, 17]

This increase in average global surface temperature is causing numerous physical changes in the climate. One of the physical results described by the IPCC was the

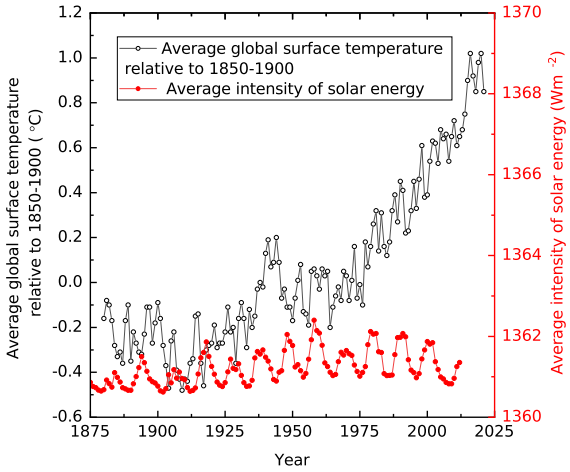

Figure 1.1: *The increase in average global surface temperature since 1875 compared with the lack of change in average intensity of solar energy. [8–10]*

increase in extreme trends of the global hydrological cycle, i.e. the dry regions get drier and the wet regions get wetter. [18–21] Extremities in either direction are dangerous. Extreme precipitation and monsoons can destroy homes and livelihoods and lead directly to deaths. [22, 23] Droughts can lead to difficulties having enough water to live, as well as drying out land, increasing the likelihood of forest fires, further endangering lives. [24] Both reduce crop yields, which worsens world hunger and leads to more deaths. [25–27] And both can lead to the destruction of habitats vital for endangered ecosystems, worsening the current biodiversity loss. [28–31]

Another physical result described by the IPCC is the melting of glaciers and the arctic ice cap. There is evidence that the arctic sea ice is at its lowest levels in one thousand years and the retreat in glaciers is unprecedented in the last two thousand years. [32–39] This endangers vital ecosystems, as well as increases the rate of increase of the average global surface temperature (ice reflects sunlight away from the surface more efficiently than land or water). [40, 41]

Furthermore, due to the extra heat on the surface of the planet, the upper surface of the oceans is increasing in temperature. [42–50] A warmer ocean will have a larger volume and combined with the melted sea ice has led to sea levels rising. [45, 51–55] This means land close to sea level will be highly susceptible to temporary or even permanent flooding and all the issues associated with that as discussed above for extreme precipitation. Furthermore, some of the excess carbon dioxide in the atmosphere has been absorbed by the ocean, leading to unusually low pH levels (i.e. higher levels of acidification) in the last two million years. [56–59] The rising, warming and increasingly acidic ocean conditions have contributed to the destruction of marine ecosystems and further biodiversity loss. [60–62]

All of these effects reported above are projected to get worse as the average global surface temperature increases further. As a result, almost every nation in the world

signed the Kyoto protocol in 1997 (plus the Doha amendment in 2001), which meant they agreed to monitor (and reduce) the emissions of the greenhouse gases CO_2, methane (CH_4), nitrous oxide (NO_2) and the F-gases, which are hydrofluorocarbons (HFCs), perfluorocarbons (PFCs), sulfur hexafluoride (SF_6) and nitrogen trifluoride (NF_3).

In Figure 1.2(a), a breakdown of global greenhouse gas emissions by sector is shown for 2016 (the most recent year for which reliable data could be found). [63] The variety of sources of greenhouse gas emissions show the challenge it takes to reach net zero greenhouse gas emissions. Transportation as well as energy use in industry and buildings contribute over half the total emissions. The greenhouse gas emissions from energy use in industry and buildings can predominantly be attributed to heating and electricity. Direct emissions from any industrial process (such as making cement) are included separately. To produce the fuel for transportation and for use in building and industry requires further fugitive emissions (i.e. emissions such as extracting the fuels), meaning that nearly three quarters of all emissions are related to generating energy for society to use. The remaining greenhouse gas emissions come predominantly from agriculture, forestry and land use, with small contributions from waste and the previously mentioned industrial processes.

The solution to removing all these sources of greenhouse gas emissions is not currently understood. One thing that is known is that electrification can be a large part of the solution for reducing the greenhouse gas emissions of society's energy usage. One example is heating buildings (particularly residential ones) using electric heat pumps and another is the take-up of electric cars to replace cars that burn petrol and diesel. Therefore, the amount of electricity society will need is expected to increase. One study looking at three different scenarios projects an increase from 78 exajoules per year (EJ) in 2020 to 127-236EJ by 2050 and 238-387EJ of electricity by 2100. [64]

1.2 Electricity options

If a lot of the sources of greenhouse gas emissions are to be electrified, then it is vital that we generate electricity in a way that does not emit greenhouse gases. Currently, the vast majority of electricity is generated using coal, oil and natural gas (see Figure 1.2(b)). [65] The fuels are burnt and the resulting heat is used to boil water into steam. This steam is used to turn a turbine and the kinetic energy of the rotating turbine can be converted to electricity using a generator. The initial burning of the fossil fuels releases carbon dioxide and other gases. Additionally, there are other emissions related to the extraction and refining of these fossil fuels that make them significant sources of greenhouse gases. A proposed way to resolve

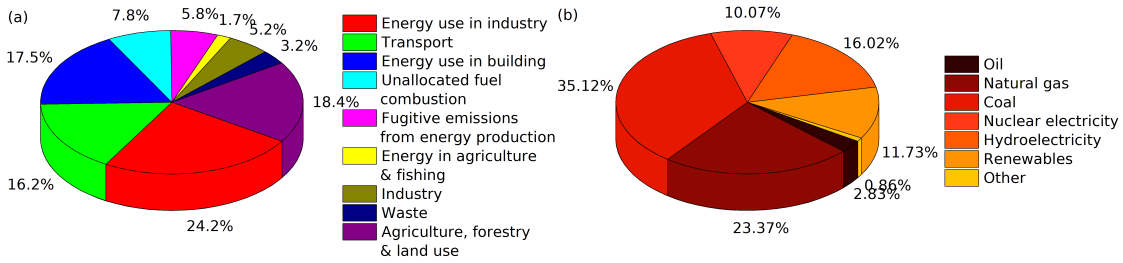

Figure 1.2: *(a) Summary of the sources of the global greenhouse gas emissions for 2016. [63] (b) Breakdown of the primary energy source for the globe taken from the BP statistical world energy review 2021 for the global energy usage in 2020. [65]*

these issues is carbon capture and storage, i.e. separating the carbon dioxide as it is emitted during the process and then storing it before it is released into the atmosphere. However, this process is not perfect and inevitably some emissions still occur. [66, 67] Furthermore, this does not solve some of the other issues related to using fossil fuels, including the fact that they are non-renewable, as well as the recent geopolitical issues associated with relying on countries that produce some fossil fuels.

One alternative to fossil fuels is bioenergy which can be split into two types: biomass and biogas. Biomass is dry and combustible fuels (such as wood pellets) burnt like fossil fuels. The fuel can be grown specifically for a biomass generator or can be taken as waste products from other industries. One advantage is that old coal power stations can be converted into biomass stations so much of the infrastructure already exists. [68] Alternatively, biogas is made from wet feedstock (such as food waste) sealed in tanks that eventually produce the methane that can be used as an alternative fuel. Both biomass and biogas are in principle carbon neutral since the greenhouse gases emitted when the biomass and biogas are burned is equal to that absorbed by the feedstock when it is being grown. However, if feedstock growth replaces a more effective carbon sink (such as an ancient woodland) then the results can end up being worse for the environment. [69–71] Furthermore, the feedstock grown specifically for bioenergy will often be in competition for land from areas that would otherwise be used to grow food. This has ethical difficulties given that people are struggling for food already and this is likely to get worse due to deteriorating conditions to grow crops, as discussed above. [72, 73]

Another option is nuclear energy, undoubtedly the most divisive of the electricity options, being nicknamed everything from the messiah of clean energy to a doomsday machine. Nuclear energy works by firing neutrons at uranium-235 nuclei to make it unstable, which then splits into lighter nuclei, as well as releasing neutrons and

heat. This heat is then used in a similar way as described above. Given how energy-dense the nuclear fuel is compared with fossil fuels and bioenergy, a lot less fuel is needed compared with the alternatives discussed above. Additionally, it has the advantage of being unaffected by weather conditions, meaning it can act as a baseload for the grid. However, nuclear power is unpopular due to well-publicised accidents (particularly Chernobyl and Fukishima), as well as the links to atomic bombs. As a result, people are greatly opposed to living near to them, which makes it incredibly difficult to find a site to build them on. [74] Those in favour of nuclear power argue Chernobyl happened due to political reasons and a flawed design that has since been rectified. [75] The Fukishima disaster was blamed on leaving too many decisions in critical moments to people not prepared for such extreme events. [76] Nuclear power is considered a sustainable technology because no carbon is released during the running of the power plant. Even considering the life cycle assessment, nuclear power has one of the lowest greenhouse gas emissions of any option listed here. [77, 78] Others argue that beyond the greenhouse gas emissions, the overall environmental impact of nuclear power, considering the nuclear waste and the decommissioning of the plant, is the worst option for the environment. [79] There are no reliable options for disposing of highly radioactive nuclear waste currently, though deep geological sites are thought to be the best option. [80–82] Nuclear power plants have a median construction time of seven and a half years, but have been known to take as long as thirty-six years, which suggests they cannot be a quick solution to lowering greenhouse gas emissions from electricity. [83] Furthermore, the initial construction costs are prohibitively expensive, limiting who will actually take on the upfront cost, which leads to a high electricity cost. [84–86]

Another alternative for electricity generation is hydropower. Hydropower relies on damming water and, dropping the water from a height and using the kinetic energy of the falling water to turn turbines, which can then generate electricity as described above. This is a renewable energy and, furthermore, it has the advantage of being able to use energy to pump water to the top of the dam when electricity demand is low, the system acts as an energy storage system, which is beneficial considering the intermittency of some of the options below. [87, 88] One problem with building dams is that the diverted waterflow means ecosystems are unsettled, particularly for migratory fish species (though redirecting solutions to this have been found). [89, 90] Another issue is linked to difficulty in finding sites with sufficient water; this has in the past led to whole communities being displaced. [91–94] Damming water has implications for water availability downstream, which has contributed to international conflicts when the river crosses national borders. [91, 95–99] The issue will worsen as droughts become more common and extreme. A final drawback is linked to methane emissions that are emitted from microbes that form in standing

water that reduce the environmental credentials of the technology. [78, 100, 101]

Geothermal is another way to generate electricity. Geothermal electricity involves taking water deep underground and pumping it to the surface under a high pressure. When the water reaches the surface, the pressure drops and the water turns to steam which can then be used to generate electricity as above. This is another form of renewable energy provided the steam is pumped back underground at the same rate it is used at the surface. [102] There are no greenhouse gas emissions during the running of the geothermal plant and life cycle assessment shows a low overall greenhouse gas footprint. [78] Using geothermal electricity requires holes of at least one mile deep so there are only limited locations with the right conditions for geothermal electricity. [103, 104] This is further restricted by minor risks of earthquakes, meaning the sites cannot be too close to human settlements. [105–109]

Wind energy is another form of electricity generation that has become increasingly popular, with wind farms now generating similar scales of electricity to fossil fuel stations. Wind energy involves using an aerofoil blade to convert the kinetic energy of the wind to kinetic energy of a rotor, which is connected to the generator that converts the kinetic energy to electrical energy. The wind is renewable and free, making it an attractive energy source. To properly locate the wind turbines, the site should have high wind speeds but low turbulence to maximise electricity generation. [110] The turbines can be located offshore or onshore. Onshore wind turbines have the advantage of being the cheapest form of electricity and can be integrated into existing farmland. However, onshore wind is less reliable and there are concerns about noise and visual pollution. [111–114] Offshore wind turbines have the advantage of a more reliable wind but are more expensive to install. Both onshore and offshore wind turbines have been shown to be a small risk to wildlife (particularly birds and bats), though this can be mitigated. [112, 115, 116] The biggest problem is that wind turbines can only generate electricity while the wind is blowing, which might not coincide with when the grid demands it. Energy storage is needed to ensure the electricity is not wasted and makes sure the intermittent electricity generation does not damage the grid. [117–120]

Solar photovoltaics (PV) is the final electricity generation technology considered to be feasible to scale up to the capacities needed by society. PV is the topic of this thesis and will be explored more in the following chapter. Like wind, PV has the advantage of being a renewable source of energy. A further similarity is that the panel can only generate electricity when the sun is shining, which again may not coincide with when the grid demands it, so solar panels also require a form of energy storage. An advantage of solar over wind is the panels can be placed anywhere that gets sun and will generate electricity whenever exposed to sunlight. PV and wind are projected to be the main sources of electricity for the net zero future, with the

two tending to peak annually at opposite times, meaning they work well together. [121] The previously mentioned study predicts scenarios where the 4EJ of PV in 2020 rises to 40-127EJ in 2050 and 189-660EJ in 2100. [64] Similarly, one study predicts the primary energy supply from PVs will rise from less than 1% currently to 69% by 2050, while another projects PV to rise from 0.00234EJ installed capacity in the present to 93.6-347.4EJ in 2050 and then 374.4-795.6EJ in 2100. [122, 123] In this thesis, studies are presented showing new materials for PV applications to try and improve a technology that is projected to be so important as society tries to reach net zero greenhouse gas emissions. In the next chapter, how PV works will be explained and the motivation behind the materials discussed in this thesis will be explored.

Chapter 2

Photovoltaics

2.1 Material types

2.1.1 Categorising materials with the band gap

To begin to understand photovoltaics, it is important to distinguish between different types of materials. A standard way to discern between material types is their band gap. The band gap is defined as the energy difference between the top of the valence band and the bottom of the conduction band, a range in which no electronic states exist (this is an ideal case and assumes no states from defects or dopants).

The band gap can be separated into two different types, direct and indirect, as shown in Figure 2.1(a) and 2.1(b), respectively. If an electronic structure is mapped out, then each possible electronic state will have a value for the wavevector momentum space within the Brillioun zone. If the highest point of the valence band (the valence band maximum or VBM) and the lowest point of the conduction band (the conduction band minimum or CBM) both have the same value for the wavevector momentum space, then the band gap is direct. On the other hand, if the wavevector momentum space of the VBM and CBM is different then the band gap is indirect.

It is worth noting here that there is a subtle difference between an optical and electronic band gap. When an electron jumps from the VBM to the CBM, it leaves behind a hole. When the electrons and holes are still bound together as an exciton, the energy required for the electron to perform this transition is the optical band gap. If the electrons and holes become unbound by overcoming the exciton binding energy, then the combined energy for the optical band gap and the exciton binding energy is the electronic band gap. Within this thesis, the exciton binding energy is generally too small to need to differentiate between the optical and electronic band gaps.

To categorise the materials, the magnitude of the band gap (without any con-

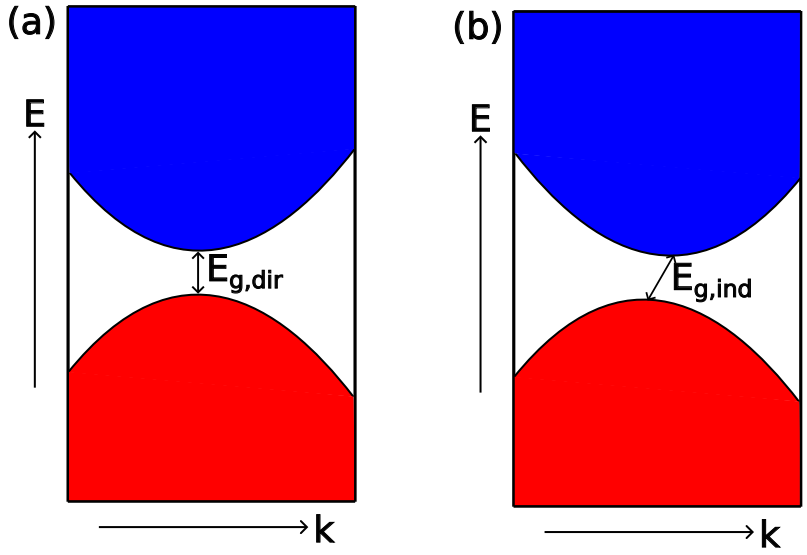

Figure 2.1: *The difference between direct ($E_{g,dir}$) (a) and indirect ($E_{g,ind}$) (b) band gaps.*

sideration for the wavevector momentum space change) is required. Materials with large band gaps are insulators, small to medium band gaps are semiconductors, very small band gaps are semi-metals, and no band gaps are metals. Putting an exact value of the band gap on the crossovers between material types (i.e. the difference between insulators and semiconductors) is subjective.

2.1.2 Doping semiconductors

Within a semiconductor there are other important concepts to define, as shown in Figure 2.2(a). The band gap, E_g, is defined above. The remaining energy levels are defined relative to the vacuum level, which is the energy of a free electron at rest immediately outside the surface of the atom. [124] The electron affinity (E_a) and ionisation potential (IP) is the energy separation between the vacuum level and the CBM and VBM, respectively.

The final energy shown on Figure 2.2(a) is the work function (W), which is the energy separation between the Fermi level and the vacuum level. The Fermi level (for any category of material) is the maximum electron energy level that any electron will occupy at 0K. Generally, it would be expected that the Fermi level for a semiconductor would lie within the band gap (with the exception being degenerately doped semiconductors).

A semiconductor can be classed as p-type or n-type. If the separation between the valence band and Fermi level is less than half the band gap, it is said to be p-type. On the other hand, if the Fermi level for the semiconductor is closer to the conduction band, then it is said to be n-type. In a p-type semiconductor, the majority carriers are the holes, whereas in an n-type semiconductor the majority

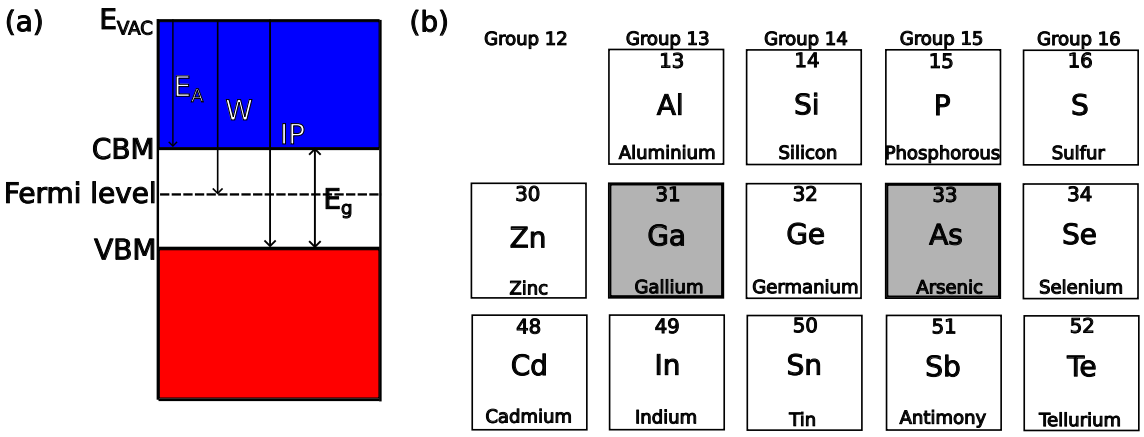

Figure 2.2: *(a) Demonstrates the electron affinity (E_A), work function (W), and the ionisation potential (IP) relative to the vacuum energy (E_{VAC}). The band gap (E_g) is the difference between the valence band maximum (VBM) and conduction band minimum (CBM). (b) Shows a small area of the periodic table with the element of interest, Ga and As, highlighted with some potential dopants on either side.*

carriers are the electrons.

A semiconductor can be p-type or n-type due to the presence of naturally occurring defects. However, if control of the level of p-type or n-type is required then introducing impurities (or dopants) can shift the majority carrier concentration and thus the Fermi level. To dope a material, p-type or n-type, requires the introduction of more holes or electrons, respectively. For a binary inorganic semiconductor, the doping can happen either on the cation or anion site. The cation (the positive ion) donates electrons to the anion (the negative ion) leaving behind holes. To dope the binary semiconductor p-type, the atoms on the cation or anion site would need to have less electrons, and to dope it n-type, the atoms on the cation or anion site would need to have more electrons. One example of a binary semiconductor is gallium arsenide (GaAs) with gallium and arsenic on the cation and anion site, respectively, highlighted in Figure 2.2(b). On the gallium site, potential p-type or n-type dopants include zinc and tin, respectively. On the other hand, the arsenic site has potential p-type or n-type dopants including tin and tellurium, respectively. Note, in this scenario, there are potential elements in Group 14, such as tin, that can be a p-type or n-type dopants depending on which site the element ends up on. Which site the dopant ends up on depends on what will be the lowest overall chemical potential for the material or the kinetics of the growth method. [125, 126]

2.2 Photovoltaic effect and the p-n junction

The photovoltaic effect is a simple concept. An incoming photon is absorbed by an electron in the valence band. If the incoming photon energy ($h\nu$) is enough for the

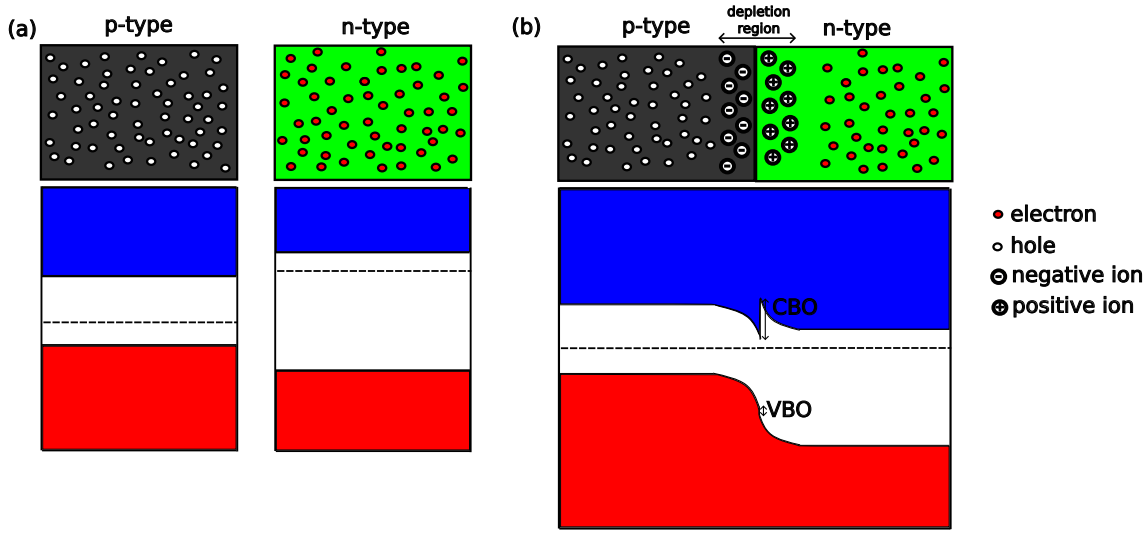

Figure 2.3: *(a) On top is the free electrons and holes for the p-type and n-type regions, respectively. Underneath the charge carrier diagram is a band diagram with the valence and conduction band region in red and blue respectively. The dashed lines are used to represent the Fermi level. (b) The charge carriers in the p-n heterojunction including the formation of the positive and negative ions which make up the depletion region. On the band diagram, the valence band offset (VBO) and conduction band offset (CBO) are labelled.*

electron to be excited across the conduction band (i.e. hν is greater than E_g), then an electron-hole pair is created. If the electron-hole pair can be extracted before they recombine, then a photocurrent can be collected. An electric field is required to separate the electron-hole pair.

A p-n junction forms, as the name suggests, when the separate p-type and n-type semiconductors are brought into contact with each other. The electrons from the n-type region diffuse across the junction and they recombine with the holes within the p-type region. This then leaves behind positive ions in the n-type region and negative ions in the p-type region. This area is known as the depletion region, with an electric field forming across the depletion region. The process is shown in Figure 2.3. Shown here is the formation of a heterojunction, which involves two different materials, whereas there is an alterative p-n junction that uses one material doped n- and p-type, which is called a homojunction. This electric field can then be used to extract the photocurrent from the photovoltaic effect. Within this thesis, the p-type semiconductor is normally referred to as the absorbing layer (which absorbs the light) and the n-type semiconductor is normally referred to as the window layer (which transmits the light) that allows the p-n junction to form. The reason the p-type and n-type region are normally the absorber and window layer, respectively, is due to the difficulty in finding a contact for an n-type absorber layer. Some work has been done on n-type CdTe recently; a full discussion into these differences is considered to be beyond the scope of this thesis. [127]

2.3 Detailed balanced limit

The power conversion efficiency (PCE) of a solar cell is the proportion of the energy from the solar spectrum that is converted into electrical energy. There is an upper limit on the PCE, mainly limited by the factors of the band gap and thermalisation. The band gap limitation is energy that cannot be extracted because the incoming photons are too low in energy to overcome the band gap. When an electron is excited beyond the CBM, it will go through a process called thermalisation where the electrons relax down to the CBM. This energy lost during the thermalisation is the second major factor limiting the PCE.

A systematic study of the upper limit of the PCE was published in 1961. [128] The study states that the maximum possibly efficiency for a p-n junction exposed to blackbody radiation is 30% for a material with a 1.1 eV band gap. It does this by considering the three limiting factors: the band gap and thermalisation factors as discussed above, as well as a geometric factor. However, the sunlight reaching the surface is not blackbody radiation so losses from the atmosphere need to be considered. The angle of the sunlight incident on the solar panels will change the amount of atmosphere the sunlight goes through, and the associated losses. The standard intensity for measuring solar cells assumes an incident angle of 48.19° and the equivalent of going through an absolute air mass of 1.5, which is called AM(1.5), with an integrated intensity of 1000 Wm^{-2}. Shown in Figure 2.4(a) is a comparison of the intensity from blackbody radiation and the intensity from AM(1.5). Assuming AM(1.5) rather than blackbody radiation slightly alters the incident solar spectrum and the resulting ideal band gap changes to between 1.3 eV to 1.5 eV, as shown in Figure 2.4(b). [129]

The study never claims that this is an achievable PCE. The methodology makes a series of assumptions that the authors accept are unrealistic. One is that all photons incident on the solar cell with energy above the band gap will be absorbed. This is of course not the case and will be dependent on the thickness of the solar cell and the absorption coefficient (the amount of light absorbed per unit length of material). Determining the band gap and absorption coefficient of the materials are key parts of this thesis.

Another relevant limitation is losses at the p-n junction interface. An important contribution to this is the CBO. If the p-type material has a conduction band lower than the n-type material, then the CBO is negative and the band alignment is cliff-like. On the other hand, if the p-type has a conduction band higher than the n-type material, then the CBO is positive and the band alignment is spike-like. For a cliff-like junction, recombination at the interface becomes a limiting factor on the PCE of the cell. For a spike-like junction, the electrons have to overcome an energy

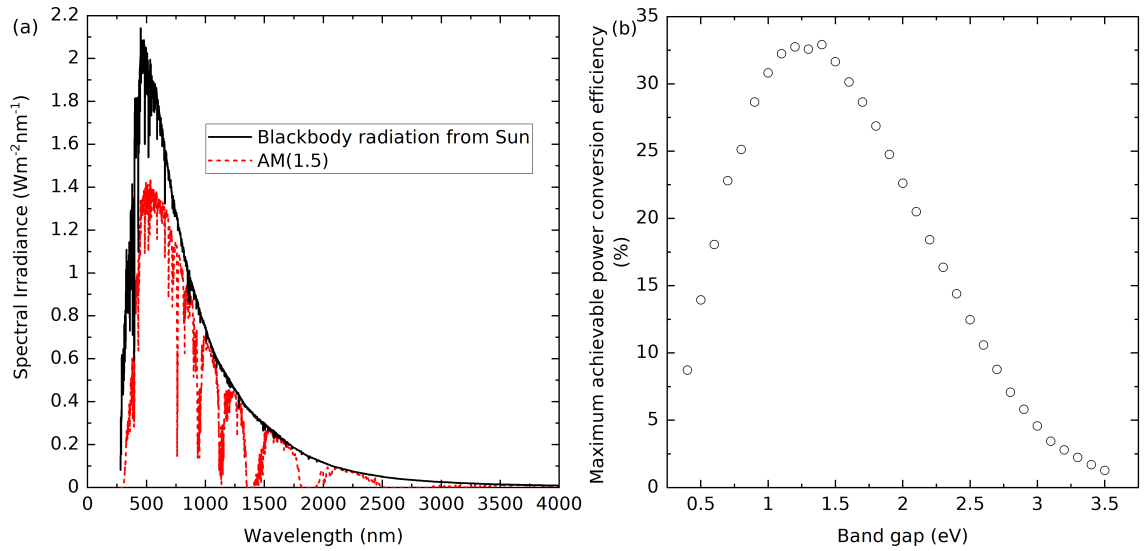

Figure 2.4: *(a) Irradiation from a blackbody compared with the standard irradiation used to assess solar cell performance (AM 1.5). (b) The detailed balance limit which states the maximum possible power conversion efficiency possible for every band gap under the solar spectrum at the surface of the Earth. [129]*

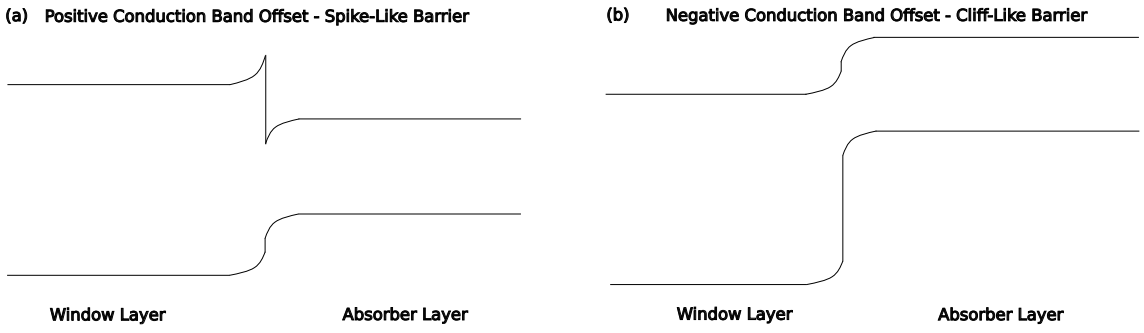

Figure 2.5: *The difference between a positive and negative conduction band offset.*

barrier, which reduces the electrical energy output. [130–133] Both of these CBOs are shown in Figure 2.5.

2.4 Solar materials

The photovoltaic effect was first reported by Bequerel in 1839 using AgCl or AgBr coated on platinum electrodes. [134] After Willoughby Smith in 1872 showed that selenium is photoconductive, William Grylls Adams and Richard Evans Day managed to produce a selenium solar cell in the late 1870s. [135, 136] This progressed into a working selenium solar module made by Charles Fritts in 1884. [137] Unfortunately, the research stalled as selenium solar cells struggled to improve in efficiency.

The turning point came in 1954 when Chaplin, Fuller and Pearson created a silicon solar cell with ∼6% efficiency. [138] Silicon solar cells have constantly improved since then, achieving efficiencies of 26.7%, and in the process have become the dominant technology in the photovoltaic industry. [139] Alternatives to silicon solar cells are being researched because of the high energy costs to make them and because silicon has a less than ideal 1.1 eV indirect band gap.

The only single junction material (see below) that has managed to beat the efficiencies of silicon solar cells is the gallium arsenide (GaAs) solar cell. The technology was developed during the 1970s and 1980s in the USSR and has since achieved an efficiency of 29.1%. [140] Unfortunately, the price of GaAs solar cells is prohibitively expensive so there is very limited commercial application. The difference in costs to manufacture single crystal wafers of GaAs rather than Si is the main cause of the price difference. [141]

There are ways being researched to exceed the detailed balance limit so more light can be converted to electricity from a single solar panel. One of the most promising methods being researched is the tandem solar cell. Multiple different layers with different band gaps are used to absorb different parts of the solar spectrum which minimises losses from both thermalisation and from light not being absorbed. Under the AM(1.5), the detailed balanced limit for a two, three, or four junction solar cell is 42%, 49%, and 53%, respectively. [142] The highest efficiency currently reported for a three junction solar cell is 39.5%. [143]

Another method currently being investigated is concentrating the incoming sunlight onto the solar cell. This means that more light hits the solar cell so more electricity can be generated. For concentrated light, the detailed balance solar cell efficiencies for one, two, three, and four junction solar cells are 40%, 55%, 63%, and 68%. [142] The highest recorded efficiency currently is 47.1%, which is a six junction tandem solar cell under concentrated light. [144]

However, concentrated and tandem solar cells still have a way to go before being

commercially viable in most applications. Therefore, much of the current research is aiming to find alternative single junction materials. One of the areas that has been researched for a number of years is organic solar cells. Good reviews of the topic are available elsewhere and so the full details are not covered here. [145] Despite a few decades of research, the material has only just achieved an efficiency of 18.2%. [146] Commercially, organic solar cells have not achieved similar efficiency to other materials, which has led to alternatives being investigated.

One type of photovoltaic solar cell currently attracting the most interest is the perovskite solar cell. The perovskite solar cell refers to the category of absorber material with the perovskite crystal structure, which has the general formula ABX_3. The most promising from a photovoltaics perspective is MAPI ($CH_3NH_3PbI_3$), which has methylammonium (CH_3NH_3), lead (Pb) and iodine (I) on the A, B and X sites, respectively. Efficiencies have increased from 3.8% in 2009 to 25.7% today, an unprecedentedly quick rise. [147, 148] There is growing evidence to suggest that a large part of the high performance of this material is due to the Pb $6s^2$ lone pair, which is thought to underpin some of its desirable PV properties. [149]

In a lone pair material, the cation in the material has an oxidation number two less than what would be expected for the group that it is in. For example, in MAPI, Pb is in the 2+ rather than 4+ oxidation state despite having 4 valence electrons. These materials come from Group 13 to Group 17 and Period 4 to 6 in the periodic table. The original theory of the lone pair model stated that the outer cation s orbital did not get involved in the bonding. [150, 151] However, growing evidence suggested that this was not the case. Walsh *et al.* reported the revised lone pair model, which shows the cation s orbital interacts with the anion p orbital to create bonding and antibonding states. In order for this hybridization process to occur, the crystal structure must be distorted as a stabilisation process. [152] The antibonding states in the VBM should lead to shallow rather than deep states, the formation of benign grain boundaries, and strong defect tolerance. The $6s^2$ orbital also results in band edges with greater dispersion, leading to smaller carrier effective masses and enhanced carrier mobility, both of which are favourable for PV applications. [153] However, perovskite solar cells are unstable with rapidly decreasing efficiency under light and air exposure, a problem for any solar material. [154]

The only material group that has achieved any inroads into the silicon market share is CdTe, an inorganic semiconductor. Thin film cadmium telluride (CdTe) has been a major success in achieving an efficiency of 22.1%, similar to silicon. [140] However, there are issues with CdTe, including concerns regarding the toxicity of cadmium and the scarcity of tellurium, the latter of which in particular will limit the extent to which CdTe can meet the challenge of scaling up PV for terawatt energy generation. [155, 156]

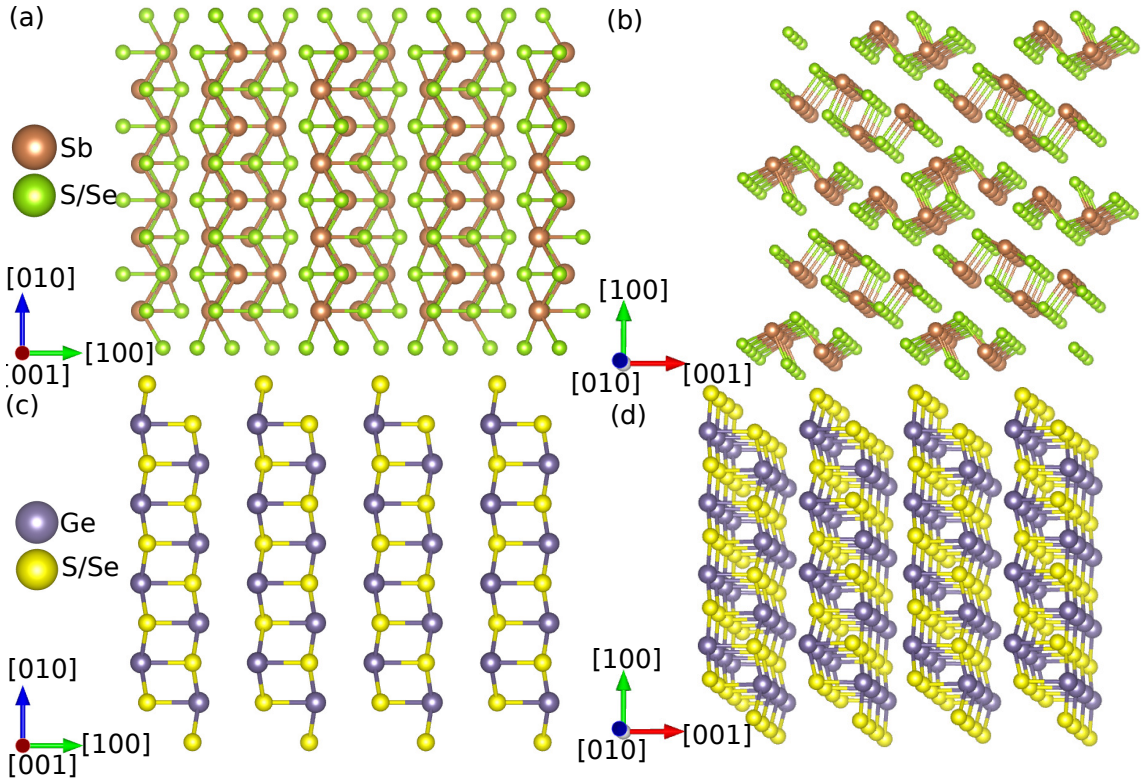

Figure 2.6: *The crystal structure of Sb_2S_3/Sb_2Se_3 (a) along the [001] direction and (b) rotated slightly to highlight the nanorods. The crystal structures of GeS/GeSe (c) along the [001] direction and (d) rotated slightly to highlight the nanosheets are shown for comparison. All three structures are orthorhombic with the Pnma space group, but Sb_2Se_3 is composed of nanoribbons whereas GeS and GeSe are composed of nanosheets. These images were prepared using the VESTA software.[157]*

An alternative series of inorganic semiconductors are antimony sulfide (Sb_2S_3), antimony selenide (Sb_2Se_3), and the alloy $Sb_2(S_xSe_{1-x})_3$. Antimony, sulfur and selenium are all more commonly occuring in the Earth's crust than cadmium and tellurium. [158] The materials also have the lone pair effect with the Sb $5s$ orbital. [159] The $Sb_2(S_xSe_{1-x})_3$ solar cell has just reached an efficiency of over 10% despite limited research into the material. [160] Another interesting feature of the Sb-chalcogenide alloy series is its orthorhombic *Pnma* crystal structure, which comprises 1D ribbons of covalent Sb-Se bonds extending along the [010] direction, with van der Waals interactions between the ribbons along the [001] and [100] directions (Figure 2.6(a) and (b)). We note that some reports use the alternative *Pbnm* space group setting, but we use the *Pnma* setting for consistency. [161] The difference between *Pbnm* and *Pnma* involves how the axes are defined. Theoretical studies suggest strong conductivity parallel to the ribbons but weak conductivity in the perpendicular directions, where the electrons have to hop between ribbons, making growth orientation an important factor in solar cell design. [162, 163] This is supported by experimental evidence. [164] Within this thesis, the $Sb_2(S_xSe_{1-x})_3$ alloys are the focus of Chapter 6.

The related series of germanium sulfide (GeS), germanium selenide (GeSe), and the alloy GeS_xSe_{1-x}, share a lot of the same properties as the Sb-chalcogenide alloy series. Ge is less toxic than both Sb and Cd. Ge is also over six times more Earth-abundant than Sb and Cd, and both S and Se are considerably more abundant than Te. [158] While the Ge-chalcogenide alloy series share the same *Pnma* space group as Sb_2Se_3, they have covalent bonds in the [001] and [010] directions, creating sheets rather than ribbons, with van der Waals interactions along the [100] direction (Figure 2.6(c) and (d)). As noted above, studies on Sb_2Se_3 suggest strong conductivity in the direction of the covalent bonds but weak conductivity in the directions of the van der Waals interactions. Having covalent bonds along two directions could therefore be beneficial for cell design, whilst also benefiting from the benign grain boundaries. Finally, Ge is in the 2+ oxidation state in both GeS and GeSe and adopts a distorted local structure, which suggests they may have stereochemically active lone pairs. [152, 165, 166] These properties, along with the recently reported 5.2% power conversion efficiency for a GeSe solar cell [167], demonstrate the potential of these materials. Within this thesis, GeS, GeSe and the GeS_xSe_{1-x} alloy are the focus of Chapters 4 and 5.

Chapter 3

Methodology

In this chapter, the physical principles and data analysis about the experimental techniques used in chapters 4 to 6. This includes details about how samples were prepared as well as the various characterisation techniques used.

3.1 Material growth and deposition

3.1.1 Crystal growth

The technique used throughout this research to grow bulk crystals is a melt growth technique. The first step is to calculate the molar mass (m_r) of the target crystal. For example, calculating the $GeS_{0.5}Se_{0.5}$ molar mass would be:

$$GeS_{0.5}Se_{0.5}\ m_r = 72.63 + 0.5 \times 32.06 + (1 - 0.5) \times 78.971 = 128.1455 \text{ g mol}^{-1} \quad (3.1)$$

where 72.63, 32.06, and 78.971 are the molar masses of germanium (Ge), sulfur (S), and selenium (Se) in g mol^{-1}, respectively. Using this value, the moles are calculated as the ratio of target mass over molar mass. Continuing the $GeS_{0.5}Se_{0.5}$ example, and with a target mass of 3g, the number of moles (n) is:

$$n = \frac{3}{128.1455} = 0.023411 \text{ mol} \quad (3.2)$$

The molar ratio of the chemical reaction is used to find the number of moles of Ge, S, and Se, respectively. Finally multiplying the number of moles by the molar mass of the element allows for the calculation of the mass of each element needed in the melt growth. For example, the mass of germanium (m_{Ge}) in $GeS_{0.5}Se_{0.5}$ would be:

$$m_{Ge} = 0.023411 \times 72.63 = 1.7003 \text{ g} \quad (3.3)$$

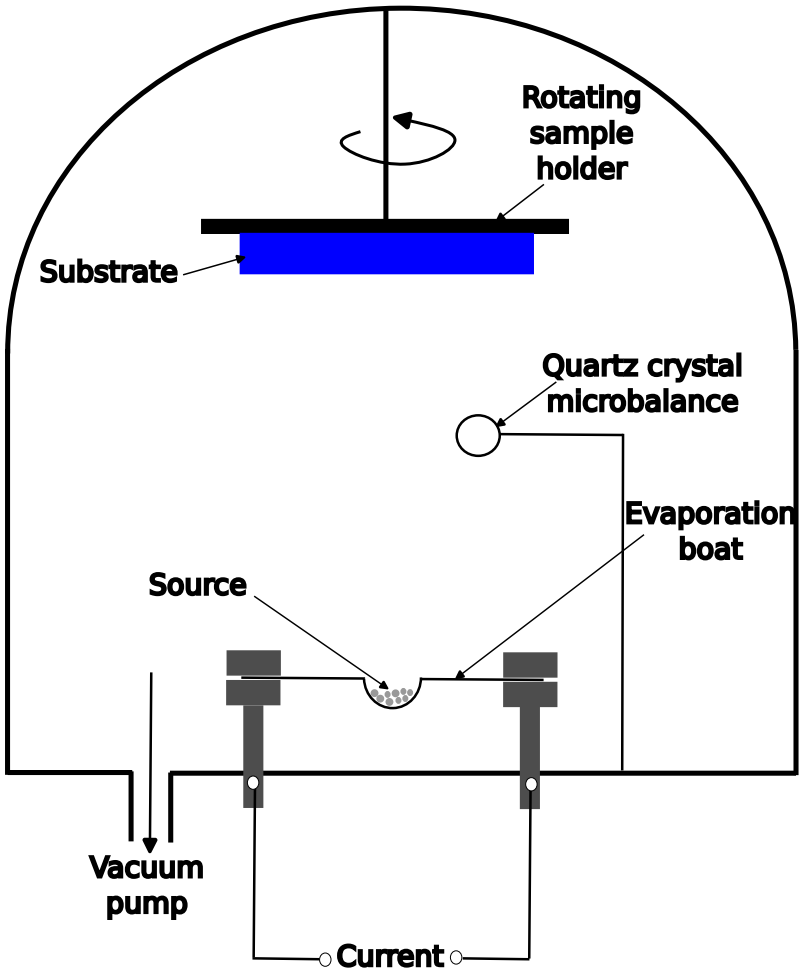

Figure 3.1: *Schematic diagram of a thermal evaporator with a quartz crystal microbalance to monitor the film thickness.*

The masses of the elements calculated are then put into a quartz tube and then sealed under vacuum to a pressure less than 1×10^{-4} Torr.

The quartz tube is then placed into a box furnace and heated to a temperature where all constituents are in a liquid form. The tubes are then held at this temperature for up to 48 hours which allows for the powders to homogenise using convection currents. The temperature is then ramped down slowly to allow for the crystal to become solid without any secondary phases forming. When the temperature is low enough that the material is solid, the quartz tube is then held at temperature for up to 100 hours to allow the crystal to grow. Finally, the temperature of the quartz tube and its contents are allowed to cool naturally to room temperature.

3.1.2 Thermal evaporation

The main technique for depositing the source material as a thin film is by thermal evaporation. This is done by loading the source material (whatever substance you want to deposit) and the substrate you want to deposit on as shown in Figure

3.1. The set up is then sealed under vacuum before a current is passed through the evaporation boat to resistively heat the boat and the source material within it. Once sufficiently heated the material will be converted to a vapour and deposited throughout the chamber including on the substrate. The substrate is rotated to improve the uniformity of the film.

Three different chambers are used within this research:

- Moorfield 307 is used to deposit the Ge chalcogenide alloy series in Chapter 4
- Moorfield MiniLab 080 is used to deposit the Sb_2Se_3 and GeSe layers in the devices in Chapter 5 as well as the Sb alloy series in Chapter 6
- Oerlikon Leybold Vacuum, Univex 300 Thermal Metal Evaporator is used to deposit the Au contacts in Chapter 5.

The film thickness is monitored within the chambers using a quartz crystal microbalance (QCM). The quartz crystal is a piezoelectric material; when a current runs through the material it oscillates. When more material is deposited onto the crystal, the frequency of the oscillations changes. The rate of change allows for us to monitor the mass deposited in real time.

In order to monitor this rate of deposition, the QCM is calibrated using profilometer measurements of film thicknesses. To measure the film thickness using a profilometer, a step in the film must be created in the film, which is created by scribing the film or masking the substrate before the evaporation. The stylus is brought into contact with the surface with a specified force. This stylus is then scanned across the step. A change in height of the stylus is measured as it is scanned across the sample, meaning the height of the film is determined. The profilometer used throughout this research is an Ambios XP-200 surface profilometer.

3.1.3 Sputtering

Radio Frequency magnetron sputtering is another technique used to deposit thin films within this work. The technique requires a target made of the same material as the planned thin film. Ar^+ ions are generated and directed towards a target using an electric field created by a radio-frequency alternating current. When the ions bombard the target, a plasma is created above the target. In magnetron sputtering, a permanent magnet is underneath the target to attract the Ar^+ ions. Once the plasma is generated it will coat the entirety of the inside of the chamber, including the substrate.

RF magnetron sputtering was used to deposit CdS in the research reported in Chapter 5 and 6. The system used within this work is an AJA Orion 8 deposition system using an established methodology from our laboratory. [168]

3.1.4 Spin coat deposition

Spin coating is a simple form of solution processing of thin films. The first stage involves dissolving the target material for the thin film in a volatile solvent. This solution is then deposited onto the substrate, either statically (while the substrate is stationary) or dynamically (while it is spinning). Centrifugal forces then move the solution to the edge of the substrate, leaving a uniform film behind. The films then start to dry and the solvent will begin to evaporate, leaving behind the target material as a thin film.

Spin coating is used to deposit poly (3-hexylthiophene) (P3HT) and TiO_2 in the work reported in Chapter 5 and 6, respectively. To deposit the P3HT a Laurell 650 series spin coater is used. To deposit the TiO_2, an Osilla spin coater is used. Both methodologies follow those established previously within the University of Liverpool laboratory. [169, 170]

3.2 Material characterisation

3.2.1 Inductively Coupled Plasma Optical Emission Spectroscopy

Inductively coupled plasma optical emission spectroscopy (ICP-OES) is used to measure composition ratios for bulk crystals presented in each results chapter. The powders are dissolved in acid before being diluted in deionised water. The atoms within the samples are excited by Ar plasma. When the excited electrons return to the ground state they emit electromagnetic waves characteristic of each element. The method of using the optical intensities to measure the compositions is described in chapter 4.

ICP-OES scans are measured using an Agilent 5110 ICP-OES spectrophotometer.

3.2.2 X-ray diffraction

X-ray diffraction (XRD) can provide information about the phase of a crystalline material and the dimensions of its unit cell. To begin this technique, x-rays are generated and selected to produce monochromatic radiation. This monochromatic radiation is then collimated to increase the intensity before being fired at the sample of interest. Max von Laue showed that a crystalline substance acts as a three-dimensional diffraction grating and can therefore produce an interference pattern.

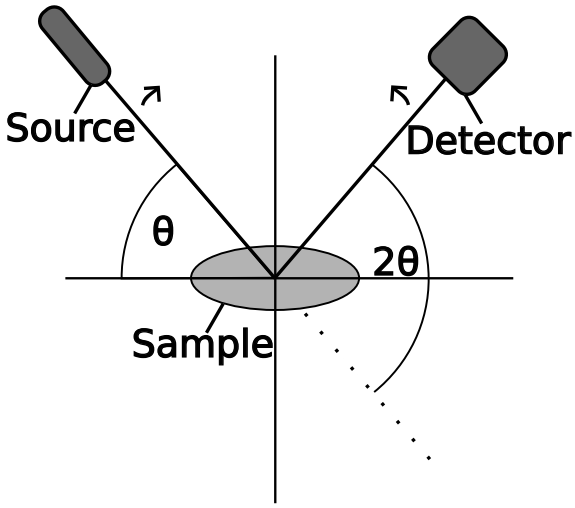

Figure 3.2: *The XRD set up when performing a θ:2θ scan.*

[171] Constructive interference occurs when Bragg's law is satisfied [172]:

$$n\lambda = 2d_{hkl}sin\theta \tag{3.4}$$

where n is a positive number denoting the order of the interference, λ is the wavelength of the x-ray, d_{hkl} is the interplanar spacing for plane with Miller indices hkl and θ is the angle between the incoming x-ray and the plane of the crystal.

In a θ:2θ scan, the collimated x-ray beam strikes the sample at an angle of θ and the x-ray detector is placed at an angle 2θ, as defined in Figure 3.2. When Bragg's law is satisfied there will be a peak in the intensities of the x-rays. During an XRD scan, the x-ray beam and detector are rotated through a range of angles where different constructive interference peaks become apparent and thus deduce information about the crystal structure.

In this research, three types of XRD are used: single crystal XRD, powder XRD and thin film XRD. Single crystal XRD was not performed by the author so is not covered in detail here. Powder XRD and thin film XRD, as the names suggest, involve XRD measurements of pulverised crystals and thin films, respectively. In both cases, θ:2θ scans are performed and the first order constructive interference peaks are measured.

Within a crystal structure, like the *Pnma* crystal structure studied here, there will be a primitive unit cell. In an XRD scan there will be a series of peaks associated with the various parallel planes of atoms, defined by the Miller indices hkl. The position of the peak in the 2θ scan related to the parallel plane hkl will be dependent on the interplanar spacing d_{hkl} and the wavelength of the x-ray used, as defined in Equation 3.4. Furthermore, using Equation 3.4, the lattice parameter for XRD patterns can be calculated as discussed in more detail in Chapter 4.

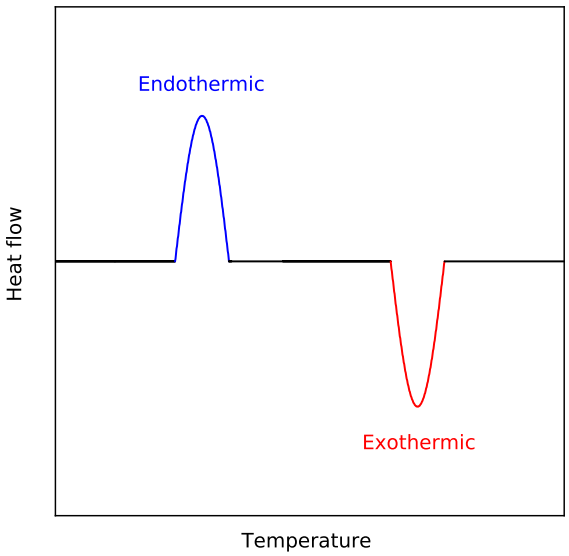

Figure 3.3: *The different peak positions in a schematic differential scanning calorimetry scan depending on if the reaction is endothermic (blue) or exothermic (red).*

If a powder XRD scan is used, and the powder is completely pulverised so there is no preferrential orientation, then an expected powder diffraction spectrum can be generated if the unit cell of the material of interest is well understood. The peak positions, as discussed above, are known from the interplanar spacing. Further information about the intensity of the peaks can be calculated using the structure factor for each plane. The structure factor indicates that the intensity of the peak is determined by the position of the atoms along the atomic planes and which atoms are in those positions (different atoms have different scattering factors). An expected powder diffraction can allow for useful examination for preferred orientation of a film growth as discussed in Chapter 4, more detail of which can be found in References [173] and [174].

All thin film and powder XRD measurements are performed using a Rigaku Smartlab x-ray diffractometer with a rotating copper anode.

3.2.3 Differential scanning calorimetry and thermogravimetric analysis

Differential scanning calorimetry (DSC) and thermogravimeteric analysis (TGA) is a combined technique for studying the thermal properties of a material. The technique requires loading a small amount of material into a sample holder and comparing it with an identical reference sample holder that is empty. For DSC, the amount of heat needed to raise the temperature of both sample holders will only differ depending on the material so the technique can be used to monitor the thermal

properties. Peaks indicate phase transitions, such as a melting point, with negative and positive peaks indicating endothermic and exothermic reactions, respectively, as shown in Figure 3.3. TGA compares the comparative weight difference between the loaded and empty sample holder to test for any mass loss during heating.

In this work, DSC-TGA was taken with a TA Instruments SDT-Q600 system, with around 10 mg of material used in each test.

3.2.4 Scanning electron microscopy

Scanning electron microscopy (SEM) involves accelerating a focused beam of electrons towards the sample. The interactions of these electrons with the sample produce a number of signals including secondary electrons, backscattered electrons and x-rays. In this research, the secondary electrons are the signal of interest. Secondary electrons are generated from the surface which allows for the collection of information about the topography and morphology of the films.

In this work, SEM measurements are carried out using a JEOL 6610 microscope at 10kV acceleration voltage.

3.3 Photoemission spectroscopy

Two types of photoemission spectroscopy are used in this research, lab-based x-ray photoemission spectroscopy (XPS) and hard x-ray photoemission spectroscopy (HAXPES). The two are discussed side-by-side below.

Both techniques, as the name suggests, require the generation of x-rays. To generate the x-rays in XPS, a filament generates electrons and directs them at the anode material which will generate characteristic energies depending on the anode material used. The anode used within this research is an aluminium (Al) anode which has a characteristic energy kα_1 at 1486.6 eV. Anodes, such as Al, produce a spectrum of x-rays due to secondary features like bremsstrahlung radiation which in this case have been removed from the source using an aluminium foil and a quartz crystal. This process is known as monochromating the x-rays.

On the other hand, x-rays for HAXPES are generated using a synchrotron. When a particle accelerator causes electrons to travel at speeds close to the speed of light and then bends the electron path, the relativistic electron emits synchroton radiation. At a facility such as Diamond light source, which is the facility used here, the synchrotron can be manipulated to generate x-rays. Synchrotron radiation is monochromated to provide a souce of x-rays. [175]

Regardless of how the x-rays are generated, the photoemission process mechanism is the same. Incoming x-rays are aimed at the material of interest to the study.

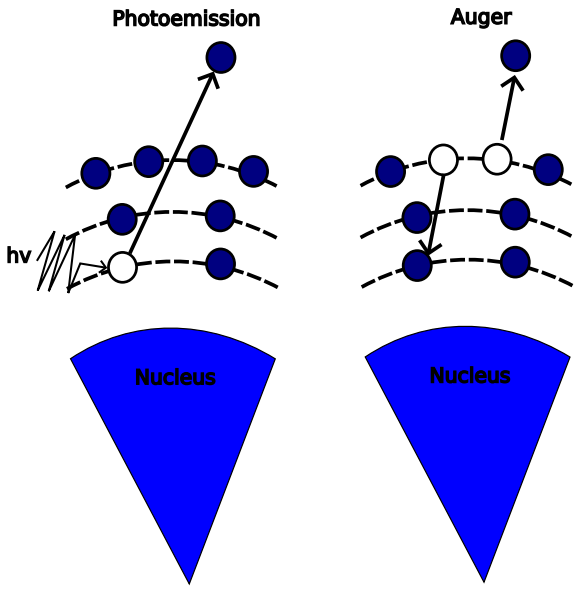

Figure 3.4: *The photoemission (left) and Auger process (right) for an excited photoelectron and for the relaxation process afterwards, respectively.*

The x-rays will then be absorbed by the electrons within the target material causing them to be ejected from their atoms, as shown in Figure 3.4. Ejected photoelectrons are then directed towards an analyser and the kinetic energy of the photoelectrons is measured. If there are no scattering processes, then the only factor that the vacuum kinetic energy (E'_k) will depend on is the following:

$$E'_k = h\nu - E_b - \phi_s \tag{3.5}$$

where $h\nu$, E_b, and ϕ_s are the incoming x-ray energy, binding energy of the electron, and the work function of the sample. To minimise the scattering between sample and analyser, the entire procedure is performed under an ultra-high vacuum. When the photoelectrons reach the analyser, they must overcome the additional work function of the analyser (ϕ_a) so the measured kinetic energy (E_k) is:

$$E_k = E'_k - (\phi_a - \phi_s) = h\nu - E_b - \phi_s - (\phi_a - \phi_s) = h\nu - E_b - \phi_a \tag{3.6}$$

and so the binding energy can be found without knowing the work function of the sample.

Examples of a HAXPES and an XPS survey are shown in Figure 3.5(a) and 3.5(b), respectively, with both being plotted with binding energy as the x-axis as is standard when reporting photoemssion results. Both HAXPES and XPS share some common features in their scans, with the first similar feature being the core levels. The core levels originate from the photoelectrons within an orbital of the atom without undergoing any scattering process. Every element will have characteristic

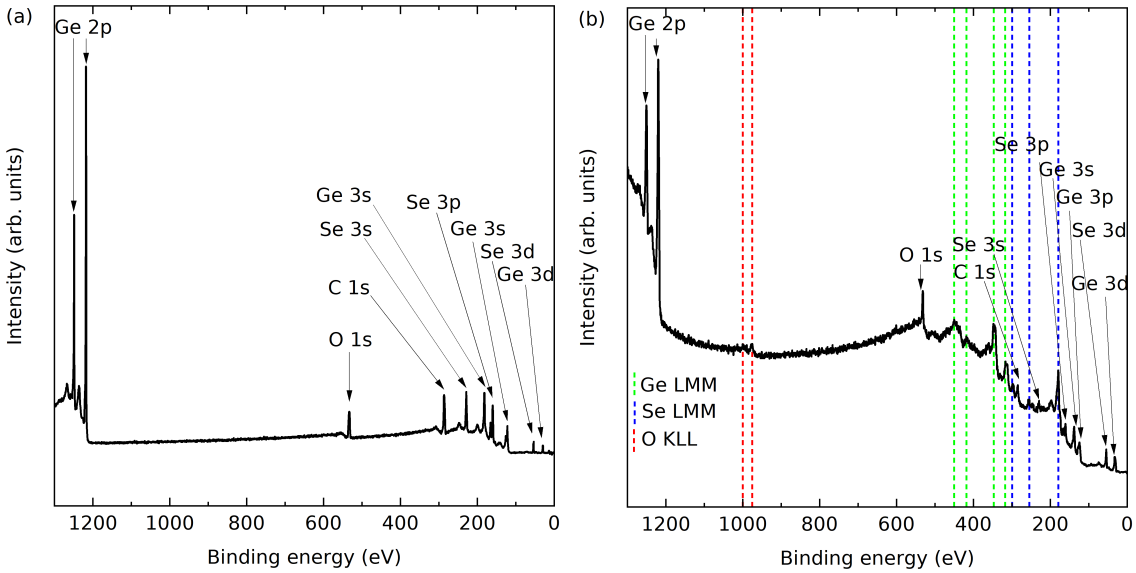

Figure 3.5: *Photoemission surveys for GeSe as measured in hard x-ray photoemission spectroscopy (a) and lab based x-ray photoemission spectroscopy (b).*

Table 3.1: *The principal quantum number (n), orbital angular momentum (l) and total angular momentum (j) for different orbitals alongside the area ratios needed to fit the pair of core levels.*

Orbital	n	l	j	Occupancy	Area Ratio
s	1	0	1/2	2	-
p	2	1	1/2, 3/2	2, 4	1:2
d	3	2	3/2, 5/2	4, 6	2:3
f	4	3	5/2, 7/2	6, 8	3:4

core levels that are at well documented binding energies. [176] The exact value of the binding energy will differ depending on the bonding environment of the electron within the atom, known as the chemical shift. This feature makes photoemission spectroscopy an incredibly powerful tool for identifying phase impurities and any contamination within the material.

In this research the software Casa XPS is used to analyse the core level peaks; full details are discussed below. A Shirley background is fitted to remove any contribution from inelastically scattered electrons from the peak. [177, 178] Then a line is fitted above the background, the line shape is typically represented with a computational combination of a Gaussian and Lorentzian (defined in Equation 3.8 and 3.9 below) which allows for the separate contributions from instrumental and lifetime broadening to be accounted for.

As shown in Table 3.1, each orbital is defined by the principal quantum number (n) which starts at 1 and increases by 1 with each orbital. The orbital angular momentum (l) is equal to n-1. The total angular momentum (j) is equal to the

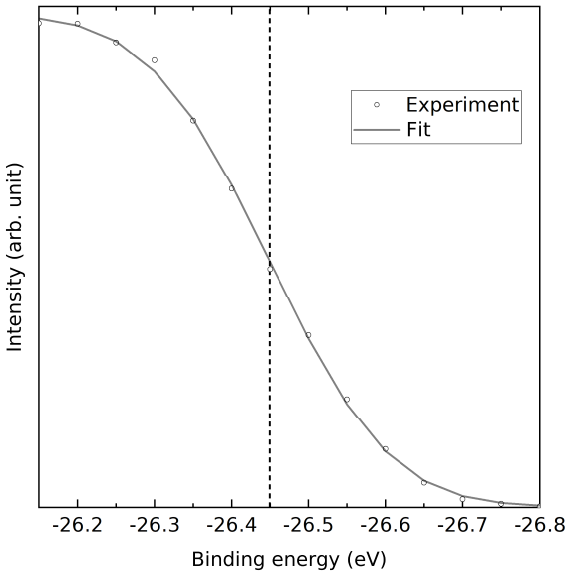

Figure 3.6: *Fermi-Dirac function fitted to a gold sample in hard x-ray photoemission spectroscopy. The dashed line indicates the shift needed for all samples, the Fermi-Dirac should centre at 0 eV when calibrated.*

l$\pm\frac{1}{2}$ (the spin angular momentum). Note here the total angular momentum cannot be smaller than zero so only one s orbital exists. An orbital is normally defined using spectroscopic notation of the form nl_j. The occupancy (number of electrons) in an orbital is equal to 2j+1, as each possible total quantum number can only be occupied once based on the Pauli exclusion principle. For example, if j=$\frac{3}{2}$ then four electrons can occupy the total angular momentums of -$\frac{3}{2}$, -$\frac{1}{2}$, +$\frac{1}{2}$ and +$\frac{3}{2}$. Using this knowledge, the following constraints can then be applied to the core level fitting:

- The area ratio of the doublets to be used when fitting core level features, defined as the ratio of the occupancy for the orbital (see Table 3.1)
- In all but exceptional circumstances the full width half maximum (FWHM) of the doublets is equal
- The doublet separation is independent of the material studied, so it can be beneficial to use doublet separations reported previously.

If the above constraints are inputted into the Casa XPS software then it will compute the peaks so as to minimise the residual differences between the fitted peak and the experimentally measured core levels.

The second common feature of both HAXPES and XPS is valence band analysis. At the lower binding energy edge of the photoemission scan, photoelectrons originating from the highest occupied energy states (i.e. the valence electrons) are detected. The spectrum is always calibrated so that the Fermi level is at zero. Therefore, for a metal sample the valence band edge will be a Fermi-Dirac distribution at zero, an example of the Fermi-Dirac distribution before calibrating the Au sample in HAXPES

is shown in Figure 3.6. However, for a semiconductor, the Fermi level will typically be at an energy with no occupied states. This will cause the valence band edge to be away from the zero position. One quick analysis that can be done for valence band edges is to measure the difference between the valence band edge and zero, using a linear extrapolation of the valence band leading edge. As the Fermi level is calibrated to zero, the value here represents the difference between the Fermi level and the valence band maximum. A more thorough analysis comes from comparing the experimental valence band spectrum with density functional theory calculated density of states discussed below in Section 3.4.

With the XPS set-up used in this research, it is possible to measure the secondary electron cutoff (SEC) which is not possible with the HAXPES set up. The photoelectrons from the SEC comes from the opposite end of the spectrum to the valence band. Here the electrons will only be secondary or inelastically scattered electrons which will only just overcome the work function of the material and so the electrons will essentially have close to zero kinetic energy. Given that the x-ray energy is known and the SEC is measured then the work function of the sample (ϕ_s) can be found with:

$$\phi_s = h\nu - SEC \tag{3.7}$$

Using SEC and the valence band position, it is possible to find the ionisation potential. Then using the valence band maximum, as well as the known band gap, the conduction band minimum can also be found. This allows for a direct comparison of the natural band alignments of materials, as reported for GeS and GeSe in Chapter 5.

Auger features appear in the XPS scans here but do not appear in the HAXPES scans. An example is shown for the Ge LMM, Se LMM and O KLL Auger feature in Figure 3.5(b). When a photoelectron is emitted from a core level, a hole is left behind which can be filled by an electron relaxing down from a higher core level. This process releases energy equal to the energy separation between the two. Sometimes this energy can be absorbed by another electron within the atom which then leads to that electron being ejected, this ejected electron is the Auger electron as shown in Figure 3.4. The kinetic energy of the Auger electron is therefore only dependent on the energy emitted by the relaxed electron, independent of incoming photon energy. However, because of the photoemission convention to plot binding energy on the x-axis, the Auger feature will shift towards higher binding energy as the incoming x-ray photon energy increases. Therefore, no Auger features are present in the HAXPES survey in Figure 3.5(a) because it is outside of the binding energy range presented. No analysis of the Auger features are performed in this research.

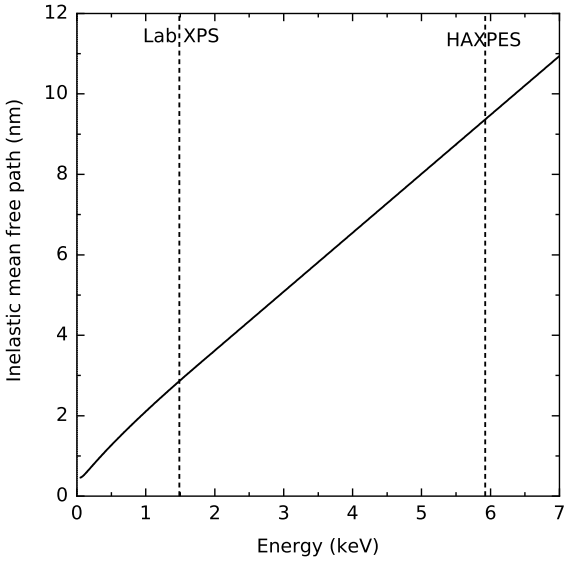

Figure 3.7: *The inelastic mean free path (IMFP) of GeSe as calculated using TPP-2M methodology. [179]*

There are further differences between XPS and HAXPES which show why it is important both are used in this research. Firstly, the resolution of HAXPES spectrometer used in this work is greater than that of the XPS spectrometer. Secondly, the inelastic mean free path (IMFP) of the photoelectrons generated from the Ge 3d in HAXPES (with a kinetic energy of 5.891 keV) are less surface sensitive than those generated from the Ge 3d in XPS (with a kinetic energy of 1.457 keV). The IMFP are illustrated for GeSe in Figure 3.7, with the kinetic energies of the electrons from the Ge 3d orbitals generated from XPS and HAXPES labelled with a dashed line, typically 95% of photoelectrons will originate in the first three IMFP of the sample. Finally, there is a difference in the one electron photoionisation cross-section of the orbitals, the probabilities of an electron being emitted from its electronic state, which can be exploited. The cross sections of the valence and semi-core orbitals in GeS and GeSe as a function of energy are presented in Figure 3.8, with vertical dotted lines indicating the energies used for measurements in this study. [180]

As can be seen in Figure 3.8, the *s*-orbital cross-sections decrease more gradually relative to other orbitals as the photon energy increases, which is due to them being more contracted. [181] This in turn implies that *s* orbitals will be relatively more prominent in HAXPES than in XPS spectra, as they will contribute a higher proportion of the total intensity at a higher incident photon energy, as found in previous studies on materials with ns^2 lone pairs. [152, 159, 182, 183]

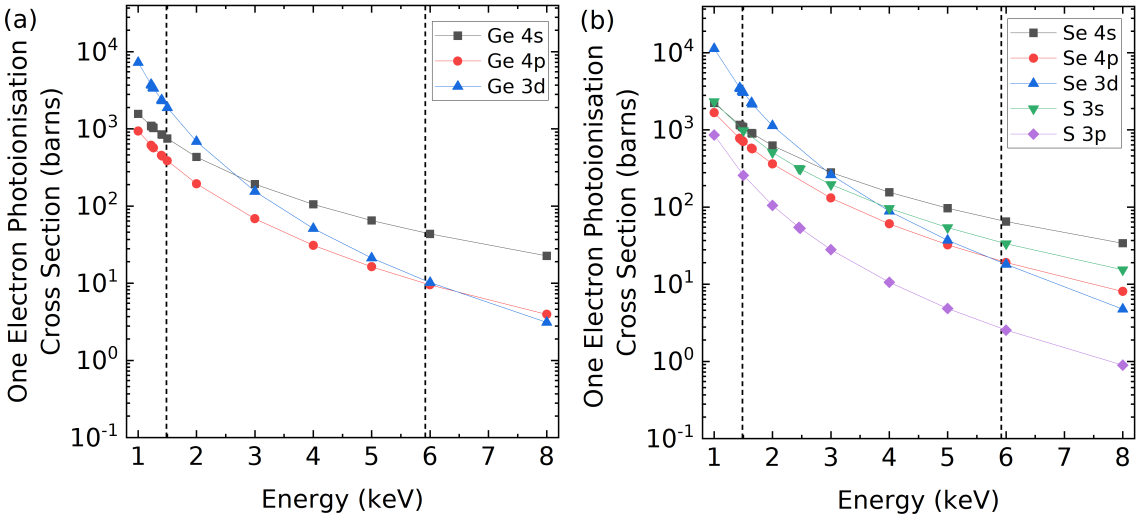

Figure 3.8: *One-electron photoionisation cross sections of (a) Ge and (b) S and Se [180]. The vertical lines at 5.921 keV and 1.487 keV show the energies used for HAXPES and XPS measurements, respectively.*

3.4 Density functional theory calculations

Density functional theory (DFT) calculations are used throughout this research to compare experiment and theory. No calculations are performed by the author of this research so a brief description of the calculations is given here, but full details are beyond the scope of this thesis.

All of the information about a quantum mechanical system is within the wavefunction of the system, which can be found by solving Schrödinger's equation. However, an exact solution to this equation can only be found for a 2D square potential or a hydrogen atom. For an N-body system, which has 3N degrees of freedom, an exact solution is impossible. Therefore, approximations must be made to find out information about the system. DFT is one way that this can be done.

The Born-Oppenheimer approximation is the most basic approximation within DFT. [184] It states that the forces on both the electrons and ions within a system are of the same order of magnitude, implying that the momenta are also of the same order of magnitude. However, because the ions' mass is much larger than the electrons' mass, the kinetic energy of the electrons is much higher than the kinetic energy of the ions. This assumption forms the basis of the approximations. It suggests that electrons will react instantaneously to the motion of ions. For an ionic configuration, we assume electrons are in the instantaneous ground state and we can therefore calculate the total energy of the system. Varying the ionic configuration means a multi-dimensional ground state potential energy surface can be defined. This implies that the motion of the ions can be treated as classical particles that are moving within this potential.

Because of this assumption in DFT, the electron density is used as the fundamental property for making calculations. This has been shown to be a useful calculation using the Hohenburg-Kohn theorem. [185] This theorem states that the density of any system determines all ground-state properties of the system. That would suggest that the ground state energy of a many electron system is a function of the electron density. Therefore, if the electron density is known then we can know the total energy of the system. It is possible to derive an effective one-electron-type Schrödinger equation solution by focussing on the electron density.

Within DFT, the electron density is described by different functionals (a functional is a function of a function). Rather than 3N degrees of freedom, they rely only on 3 degrees of freedom (x, y, z). Different functionals have been created throughout the development of DFT. Currently, the popular functionals include Perdew–Burke-Ernzerhof (PBE) and Heyd–Scuseria–Ernzerhof (HSE). [186, 187] The former is computationally easier, but the latter appear to generally provide results closer to experimental values. Additionally, corrections have been developed to account for asymmetric electron density due to van der Waals interactions, with the Grimme correction (D3). [188]

Directly comparing the experimentally determined and theoretically predicted properties such as lattice parameters and band gaps is straightforward. One comparison that requires a more detailed description is comparing the valence band spectrum from photoemission with the density of states predicted by DFT.

The reason the DFT is not directly comparable is because broadening from the instrument or lifetime as well as the cross section of each orbital is not considered. The photoionisation cross sections of the orbitals used in Chapter 5 are discussed above and shown in Figure 3.8. The first stage in comparing the DFT and photoemission valence band data involves multiplying the intensity of each DFT orbital by the one electron photoionisation cross section.

Then a convolution of a Gaussian and Lorentian distribution is applied to consider the broadening. The Gaussian distribution ($f_G(x)$) follows the form:

$$f_G(x) = \frac{1}{\sigma\sqrt{2\pi}} \exp -\frac{1}{2}\left(\frac{x-\mu}{\sigma}\right)^2 \tag{3.8}$$

where σ and μ are the Gaussian broadening factor and the average energy factor, respectively. To find σ, a Fermi-Dirac function is fitted to the Fermi edge part of the photoemission from a metal sample, usually gold. The Lorentzian distribution ($f_L(x)$) follows the form:

$$f_L(x) = \frac{1}{\pi}\frac{\frac{1}{2}\Gamma}{(x-\mu)^2 + (\frac{1}{2}\Gamma)^2} \tag{3.9}$$

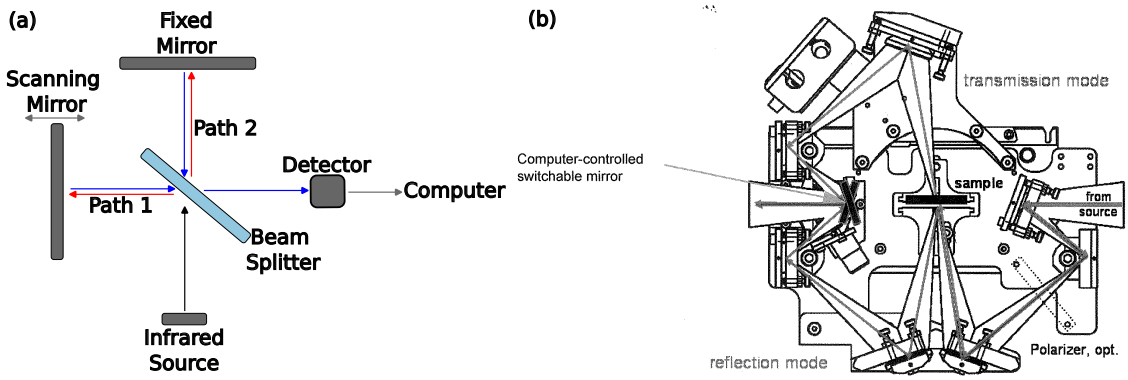

Figure 3.9: *(a) The Fourier transform infrared spectroscopy with a moving mirror to vary the wavelengths of light used in each scan. (b) The reflection-transmission accessory used to measure the sample between the beam splitter and the detector, image taken from the A 510/Q-T User Instruction from Bruker. [189]*

where Γ is the Lorentz broadening factor which is chosen to optimise the extent to which the broadened theory resembles the experimental spectrum.

3.5 Optical spectroscopy

Measurements of the photovoltaic absorbers' optical properties are a key part of this research, as discussed in Chapter 2. The techniques that are used in this research are Fourier transform infrared spectroscopy (FTIR) in Chapter 4 and UV-VIS spectrophotometer in Chapter 6, which are explained below.

3.5.1 Fourier-transform infrared spectrscopy

In FTIR a broadband beam of light with many different wavelengths is shone at the sample and the amount of light that is reflected and transmitted by the sample is measured. The sample is placed between the beam splitter and the detector in Figure 3.9, with the mirrors positioned in so that the detector can be used to measure either the reflection or transmission from the sample. The beam is modified by the moving mirror to have a different set of wavelengths throughout the experiment. The intensity detected versus the mirror position is produced and is called an interferogram. By applying a Fourier transform to the interferogram, the intensity of light at each wavelength can be found. FTIR measurements are performed using a Bruker Vertex 70V Fourier-transform infrared spectrometer with a combined reflection-transmission accessory.

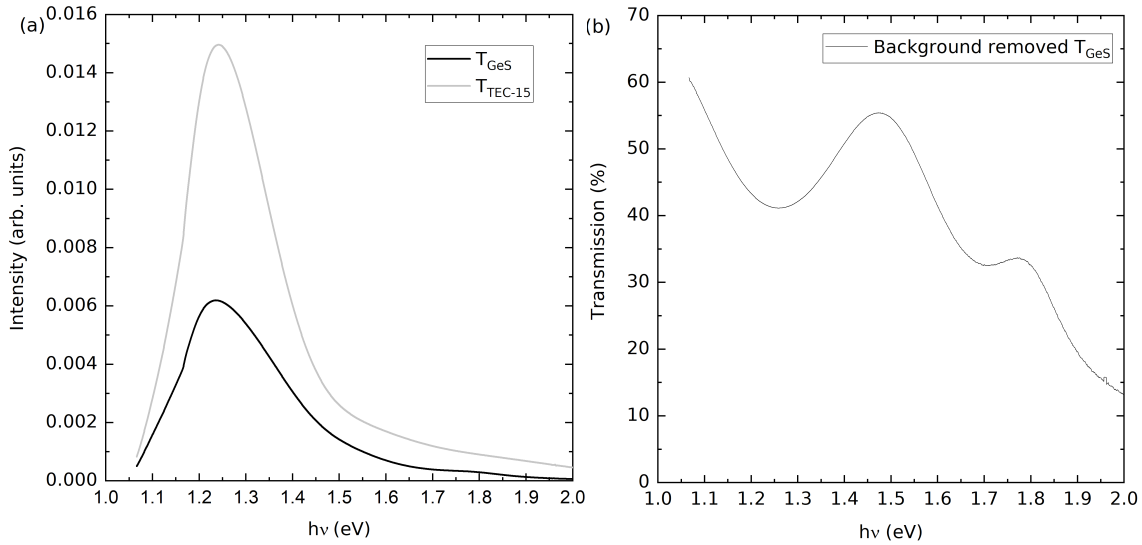

Figure 3.10: *(a) Raw data of GeS and TEC-15 transmission measured and (b) is the background removed transmission of GeS.*

3.5.2 Ultraviolet-Visible Spectrophotometer

UV-VIS spectrophotometer replaces the broadband light source with a monochromated one, meaning the intensity of transmission or reflection from the sample is repeatedly measured at regular wavelength intervals of 1 nm. Measurements in this research are taken using a Shimadzu SolidSpec-3700 UV-vis spectrophotometer.

3.5.3 Analysis

To go from the raw data to the final transmission and reflection data a number of steps have to be conducted. As well as taking the transmission and reflection data (T_{sample} and R_{sample} respectively), transmission and reflection data are also taken for the TEC-15 glass (T_{TEC} and R_{TEC} respectively). T_{TEC} and R_{TEC} are used to take into account any transmission and reflection of the TEC-15 glass, as well as the source spectrometer, beamsplitter and detector response. Alongside this the reflection of a gold mirror is also measured (R_{Au}).

This data is then used to find the transmission by doing the following equation:

$$\text{Background removed } T_{sample} = \frac{T_{sample}}{T_{TEC}}$$

An example of the raw data and the background removed transmission is included in Figure 3.10.

Similar steps were followed to find the reflection data:

$$\text{Background removed } R_{sample} = \frac{R_{sample} - R_{TEC}}{R_{Au} - R_{TEC}}$$

Using the transmission and reflection the absorption coefficient (α) from the sample can be found using equation:

$$\alpha = \frac{1}{d} \ln \frac{(1-R)^2}{T} \tag{3.10}$$

where d is the thickness of the film. This equation can be further simplified by assuming zero reflection. How the absorption coefficient is used to find the bandgap is discussed in more detail in Chapter 4.

3.6 Solar cell characterisation

3.6.1 Current density - voltage

Current density - voltage (JV) measurements are an important technique for measuring the solar cell performance. JV measurements are taken under the specific light condition AM(1.5) with a varied voltage applied across the device and the current through the device is measured. The area of the contacts is used to convert the current to the current density. In this research, the measurements are taken at room temperature using a Keithley 2400 source measure unit with the light source coming from a TS Space Systems solar simulator (class AAA). The light source is calibrated using a GaAs reference device.

A solar cell, as discussed in section 2.2, is made up of a p-n junction which is the exact same structure as a diode. Therefore, in the dark, when a voltage is applied across either a solar cell or a power diode, the current should have the same characteristic as a diode. When light shines on the solar cell, the JV curve shifts down and to the right as the cell begins to generate power.

There are a few key features to point out within the JV curves. The maximum current and voltage is the short-circuit current (J_{sc}) and open-circuit voltage (V_{OC}) is found by finding were the curve crosses the x and y axis, respectively, as shown in Figure 3.11. The bottom right quadrant relates to the power generating area of the JV measurement, with the amount of power generated being equal to the product of the current and voltage at any point. The maximum power point (P_{MPP}) is the point in that quadrant of the JV curve were the power is maximised, as shown in Figure 3.11.

A further factor that can be determined is the fill factor, a measure of the squareness of the JV curve. Using the data from the JV curve, the fill factor (FF) is:

$$FF = \frac{P_{MPP}}{V_{OC} \times J_{sc}} \tag{3.11}$$

The power conversion efficiency (PCE) of the solar cell is the ratio of the max-

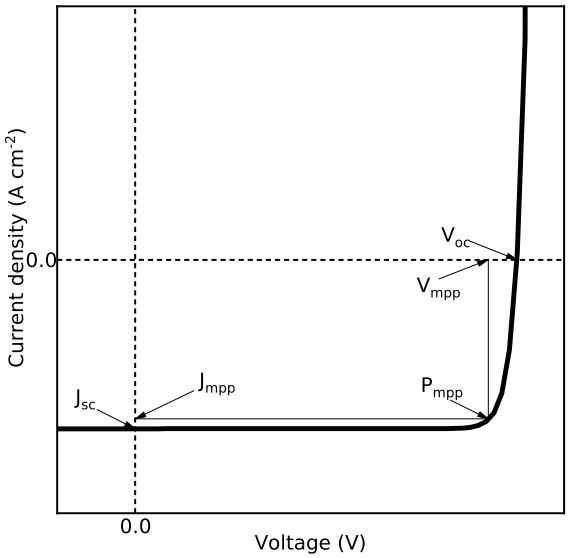

Figure 3.11: *An example of a JV curve with the J_{sc}, V_{OC} and P_{MPP} labelled.*

imum possible power (P_{max}) to the power incident (P_{inc}) on the solar cell. The maximum possible efficiency is the product of the J_{sc}, V_{OC} and FF. The incident power on the solar cell is 1000 Wm^{-2}, which is the power from AM(1.5) as discussed in Chapter 2.2. Therefore, the PCE (η) can be found using equation:

$$\eta = \frac{P_{max}}{P_{inc}} = \frac{V_{OC} J_{sc} FF}{P_{inc}} \tag{3.12}$$

Two relevant resistances, the shunt (R_{sh}) and series (R_s) resistance can also be measured from the gradient of the JV curves. R_{sh} can be found as the inverse of the gradient of the curve under reverse bias, ideally R_{sh} would be as high as possible. R_s can be found as the gradient of the curve under forward bias, ideally R_s would be as low as possible.

3.6.2 External quantum efficiencies

External quantum efficiency (EQE) is defined as the ratio of photogenerated electrons collected by the solar cell to the number of photons as a function of wavelength. In EQE measurements, the light source is monochromated and readings are taken incrementally at different wavelengths.

Neither the number of electrons out or photons in are directly measurable. To measure the number of photons in, the power of the lamp (P) can be measured and then divided by the energy of the wavelength ($h\nu$) being measured at that time. To measure the number of electrons out, the current generated (I) by the solar cell under the light source is divided by the charge of an electron (q). Dividing per unit

wavelength thus gives the equation:

$$EQE(\%) = \frac{I \times h\nu}{q \times P \times \lambda} \tag{3.13}$$

In this research, the EQE measurements are carried out with a Bentham PVE300 EQE system with a TMC300 Monochromator and Bentham 605 power supply.

3.6.3 Capacitance voltage

Capacitance voltage (CV) measurements are taken to find the doping density within different devices, using the method reported by Hllibrand and Gold. [190] The basic principle of the measurement is to apply a voltage (V) across the device and measure the capacitance (C) at different voltages. A full mathematical derivation is considered beyond the scope of this thesis but is covered in Reference [191]. The relevant equation is doping density (n) is given by:

$$n = \frac{2/q\epsilon}{\frac{d(1/C^2)}{dV}} \tag{3.14}$$

where q and ϵ are the charge of an electron and the permittivity of the material being investigated. If $1/C^2$ is plotted against V, then the gradient can be measured and used to find the doping density of the material.

In this research, the CV measurements are carried out using a Boonton 7200 Capacitance Meter in ±500mV range at frequency 1MHz, the frequency fixed for the set up.

Chapter 4

Properties of Ge(S,Se) alloys

4.1 Introduction

At the end of chapter two, it was recommended that the GeS_xSe_{1-x} series is an important material to research as a photovoltaic material. In this chapter, results are presented using bulk crystals and thin films of nine compositions of GeS_xSe_{1-x} to study the thermal, structural and optical properties of the series. This includes a specific study of the GeSe band gap. All these results are compared to the results of density functional theory (DFT) calculations.

4.2 Literature review

4.2.1 Structural studies

Studies of the variation in the lattice parameters with composition for the GeS_xSe_{1-x} series are limited. Marcheva demonstrated a linear variation in the lattice parameters between the endpoints, but without providing details of how the compositions were determined. [192] On the other hand, a series of studies on compositions with $x = 0$, 0.25, 0.5, 0.75 and 1 by Solanki *et al.* found a non-linear variation in the lattice parameters inconsistent with Vegard's law. [193–196] Im *et al.* also suggested a linear fit for the lattice parameters across a series of GeS_xSe_{1-x} nanocrystals, but again did not provide sufficient detail to compare results. [197] Notably, these studies generally determine the composition using energy-dispersive x-ray spectroscopy (EDX), which is a powerful tool for qualitatively assessing the elemental composition of films and crystals, but cannot provide accurate absolute concentrations of each element.

4.2.2 Optical studies

Germanium selenide

Unfortunately, the literature available about the optical properties of GeSe is highly conflicted, with neither the nature nor magnitude of the fundamental band gap being reconciled. This issue is further compounded when considered in unison with results from computational studies, especially those which pre-date the use of hybrid functionals, leading to misconceptions about the fundamental properties of the material.

A commonly cited value of the GeSe band gap comes from a study on cleaved single crystals, with thicknesses ranging between 25 μm to 2.25 mm. [198] This study claims indirect energy gaps of 1.075 eV and 1.080 eV for polarization parallel to the *a*- and *c*- crystallographic axis respectively (space group *Pbnm*), with reported absorption coefficients on the order of 5 cm^{-1}. Further studies on single crystals supported this polarization dependence of the band gap. [199, 200] However, other studies have found no polarization dependence and an indirect band gap of 1.10 eV. [201, 202] It has also been reported that the 1.10 eV band gap is indirect forbidden. [203] Studies on both thin films and nanobelts have found similar indirect band gaps of 1.14 eV. [204, 205] Studies on amorphous thin films have found indirect band gaps of 1.01 eV and 1.16 eV (with a direct forbidden band gap of 1.53 eV).[206, 207] In addition to these optical studies, Mishra *et al.* concluded that GeSe has an indirect band gap using angle-resolved ultraviolet photoemission spectroscopy (ARUPS). [208] The validity of conclusions from ARUPS come with considerable doubts. ARUPS is a surface-sensitive technique and the data had to be double differentiated before being interpreted. This collection of contradictory experimental data demonstrates the necessity for the nature and size of the band gap to be resolved to inform the development of photovoltaic devices.

Uncertainty also arises due to the wide range of computational results available for GeSe. Despite the extensive literature available for monolayer GeSe, our work focuses on the bulk properties. The calculated values of the band gap for the bulk vary widely. One study found a direct band gap of 1.59 eV or 1.50 eV depending on the light polarisation, whilst another found an indirect band gap of 1.45 eV independent of polarisation. [209, 210] Both of these studies, however, used semi-empirical methods, with the former constructing an effective-orbital linear combination of atomic orbitals (EO-LCAO) Hamiltonian, and the latter using empirically-derived pseudopotentials fitted to optical data of GeS and SnSe. [211] These methods are highly sensitive to the data used to fit them and have difficulty accurately reproducing conduction band states, leading to significant uncertainty in the magnitude of the gap. An *ab initio* study for GeSe revealed a band gap of 1.08 eV or 1.05 eV

dependent on whether spin-orbit coupling was included. [212] This study uses the generalized gradient approximation (GGA), which is known to inherently underestimate band gaps by around 30%, and so must be considered a lower-bound on the magnitude of the gap, but does demonstrate the minimal effect of spin-orbit coupling on both the size of the gap and the shape of the band edges.

Chen *et al.* performed a combined experimental-theoretical study on GeSe films. [213] Optical absorption measurements were analysed under the assumption of an indirect band gap, giving a room temperature value of 1.25 eV. First principle calculations using a hybrid functional found an indirect band gap of 1.24 eV. These two values should not be compared directly; the band gap varies with temperature, while DFT gives a prediction of the value at 0 K. This brief summary of the literature illustrates obvious uncertainty regarding the fundamental properties of GeSe, both experimentally and theoretically.

GeS and alloy studies

Studies of GeS generally conclude that the band gap lies in the region of 1.6-1.65 eV. [214–216] The only characterisation of the optical properties of the GeS_xSe_{1-x} series was performed using the Kubelka-Monk method to analyse diffuse reflectance data obtained from nanocrystals. [197] However, the band gap of the GeSe endpoint in that study is underestimated due to the assumption of an indirect band gap, which is discussed below.

4.3 Experimental methods

4.3.1 Crystal growth

Nine compositions of polycrystalline samples of GeS_xSe_{1-x} over the composition range $0 \leq x \leq 1$ were prepared as follows. Stoichiometric amounts of Ge, S and Se (all 5N purity, Alfa Aesar) were weighed and placed into quartz tubes sealed at $\leq 10^{-4}$ Torr of Argon. The tubes were then heated to 800 °C from room temperature at 5 °C min^{-1}, held for a dwell time of 24 h, then cooled to 500 °C at 0.3 °C min^{-1} and held for a dwell time of 100 h before cooling to room temperature at 5 °C min^{-1}.

4.3.2 Thin film deposition

Polycrystalline films of the GeS_xSe_{1-x} series were deposited on SnO_2:F-coated soda lime glass substrates (TEC-15, NSG) by thermal evaporation at a rate of $\sim$2 Å s^{-1}. Film thickness measurements were measured using an Ambios XP-200 surface profilometer and the growth conditions were monitored using a calibrated quartz

microbalance. After deposition, the films were annealed at 350 °C for 30 minutes in an N_2 atmosphere. The film thicknesses of the thinner films used for thin-film XRD, and the thicker films used for optical characterisation, are recorded in Table 4.1.

x	Thin film (nm)	Thick film (nm)
0	400±30	1630±60
0.142±0.003	410±20	1500±50
0.257±0.002	600±30	1490±30
0.330±0.004	460±20	1480±70
0.484±0.006	440±20	1600±110
0.620±0.002	350±20	1760±100
0.766±0.005	460±40	1380±50
0.825±0.004	410±20	2250±80
1	450±14	2160±80

Table 4.1: *Thicknesses of the two thermally evaporated films prepared for each of the GeS_xSe_{1-x} compositions measured using a profilometer. The thinner films were used for the thin-film XRD measurements and the thicker films were used for the optical measurements.*

4.3.3 Experimental characterisation

Samples were prepared for inductively coupled plasma optical emission spectroscopy (ICP-OES) by dissolving ∼10 mg of ground powder in a mixture of 1 ml 37 wt.% concentration HCl and 2 ml 70 wt.% concentration HNO_3 diluted to 4 vol.% acid concentration in deionised water. ICP-OES measurements on these solutions were performed using an Agilent 5110 ICP-OES spectrometer to determine the sulfur to selenium ratio. The emission intensity was linearly calibrated at each emission wavelength using five known concentrations. For sulfur, the emission wavelengths measured were 180.669, 181.972 and 182.562 nm, and for selenium the emission wavelength measured were 185.457, 185.821, 203.985 and 207.479 nm. Samples of deionised water and diluted acid were also analysed to identify any background levels of these elements.

Thermogravimetric analysis and differential scanning calorimentry (TGA-DSC) was performed using a TA Instruments SDT-Q600 system. These measurements were performed on powders in alumina crucibles with lids, which were heated at 10 °C min^{-1} to 700 °C and then cooled to 50 °C at the same rate.

Powder and thin-film x-ray diffraction (XRD) measurements were performed under ambient conditions using a Rigaku Smartlab x-ray diffractometer with a rotating copper anode. For both measurements, monochromated Cu Kα_1 x-rays were used to

perform θ:2θ scans in the range 20° to 80° at 0.5° min^{-1} in a parallel beam geometry. Measurements were taken in step-scan mode with resolution 0.01°. The error on the peak positions was taken to be half the full width half maximum of the peak, which was then propagated through to the determined lattice parameters.

For the GeSe samples, infrared transmission and specular reflection spectra were acquired at an 11° angle of incidence at ambient temperature in the range 0.9–1.8 eV using a Bruker Vertex 70V Fourier-transform infrared spectrometer with a combined reflection-transmission accessory. A tungsten near-infrared source and CaF_2 beam splitter were used for all measurements. For single crystal measurements, a liquid nitrogen cooled mercury-cadmium-telluride (MCT) detector was used. For thin film measurements, both a room temperature silicon (Si) and MCT detectors were used. For temperature-dependent optical measurements, the samples were cooled in an Oxford Instruments CFV2 continuous-flow cryostat using liquid nitrogen.

For the full alloy series, optical characterisation was performed at ambient temperature using a Bruker Vertex 70V Fourier-transform infrared spectrometer in transmission mode at an 11° angle of incidence. The measurements were carried out with a tungsten near-infrared source, a quartz beam splitter and a room temperature silicon detector.

The DFT calculations in the alloy model study here began by using Heyd, Scuseria and Ernzerhof (HSE06) to generate the structures of the end points. [217] Then, the structures and properties of the GeS_xSe_{1-x} series were calculated using the Transformer code, described elsewhere. [218] The Transformer code was used to enumerate all the symmetry-inequivalent chalcogen arrangements. The arrangements for each alloy composition were then weighted according to their occurrence probability in order to calculate thermodynamic and physical properties. For the DFT used in the GeSe band gap study, both Perdew, Burke and Ernzerhof (PBE) and HSE06 (both with Grimme correction D3 used to account for van der Waals) were used to generate structures and predict properties of GeSe. [186–188, 217] Additionally, in this case study the quasiparticle self-consistent (qsGW) approach was applied to the HSE06 structure. [219] Finally, the Bethe-Salpeter equation (BSE) was applied to the qsGW, which takes into account the exciton binding energy. [220, 221]

4.4 Results and discussion

4.4.1 Composition confirmation

For the GeS_xSe_{1-x} series, ICP-OES was used to confirm the S:Se ratio. The determined compositions are listed in Table 4.2. This was calculated using the following

method:

1. Sulfur (S) and selenium (Se) concentrations were provided in mg/L
2. These concentrations were then converted to g/L and divided by the relative atomic mass (to convert to mol/L)
3. The measured Se to S ratios were found by dividing the molar concentrations of Se by the molar concentrations of S.
4. The measured x value was then calculated from:

$$x = 1 - \frac{\text{Se : S ratio}}{1 + \text{Se : S ratio}} \tag{4.1}$$

x	Melting Point ±2 (°C)	a (Å)	b (Å)	c (Å)	band gap ±0.02 (eV)
0	665	10.839(10)	3.8352(3)	4.40(2)	1.31
0.142±0.003	658	10.801(13)	3.8104(3)	4.395(18)	1.37
0.257±0.002	649	10.769(13)	3.790(12)	4.39(2)	1.41
0.330±0.004	640	10.74(2)	3.772(5)	4.376(13)	1.45
0.484±0.006	633	10.676(19)	3.739(7)	4.366(14)	1.49
0.620±0.002	630	10.63(12)	3.709(12)	4.352(13)	1.52
0.766±0.005	626	10.593(9)	3.693(6)	4.340(16)	1.55
0.825±0.004	630	10.55(2)	3.679(10)	4.319(7)	1.57
1	647	10.479(12)	3.642(4)	4.305(15)	1.64

Table 4.2: *Summary of the compositions of the GeS_xSe_{1-x} alloys prepared in this work (x-value measured by ICP-OES) with the corresponding melting points (TGA-DSC), lattice parameters (a, b and c; XRD) and band gaps (optical characterisation).*

4.4.2 Thermodynamic comparison

The TGA-DSC measurements confirm that all of the powders are solid solutions rather than physical mixtures of GeS/GeSe and/or unreacted starting materials. The TGA-DSC of GeSe is shown in Figure 4.1(a), and measurements on all nine compositions examined in this work are provided in the Figure 4.2. All show one distinct melting point that shifts with composition, rather than the two distinct melting points for GeS and GeSe that would be expected for a physical mixture of the pure phases. We also find no evidence of unreacted sulfur or selenium, which, if present, would produce a notable spike in the DSC at the melting points of 112.8°C for S and 220°C for Se.

Our TGA-DSC is consistent with previous studies of GeSe. [222, 223] The heat flow indicates endothermic transitions occurring at 576°C, 641°C and 665°C. The

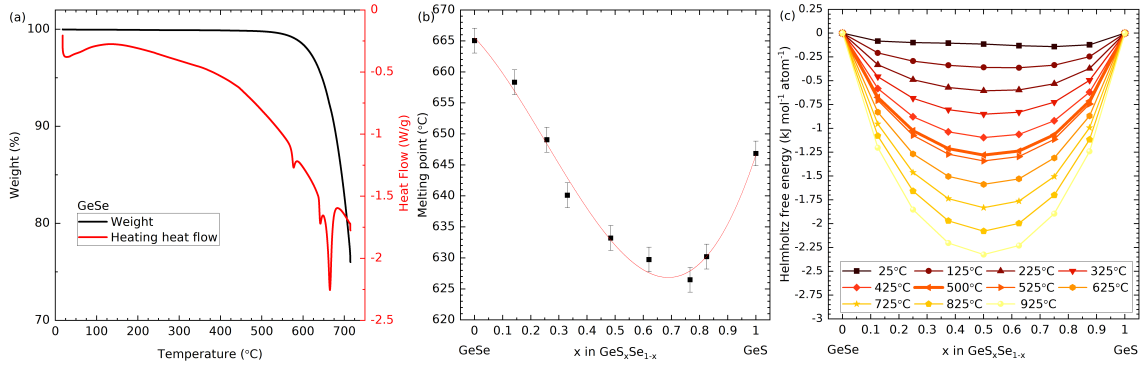

Figure 4.1: *(a) Thermogravimetric analysis and differential scanning calorimetry (TGA-DSC) of GeSe. The red line shows the heat flow as the powder is heated while the black line shows the weight loss as the powder during heating. (b) Derived melting points for all nine compositions. A fourth order polynomial fit has been added to provide a guide to the eye for the variation in melting point with composition. (c) Calculated Helmholtz free energies as a function of composition obtained calculated based on the lattice energies of structures in a supercell model of the alloy system. Thick black line marks the mixing energy calculated for an alloy formation temperature of ∼500° C (775 K), which is used to calculate the thermodynamic property averages discussed in the text.*

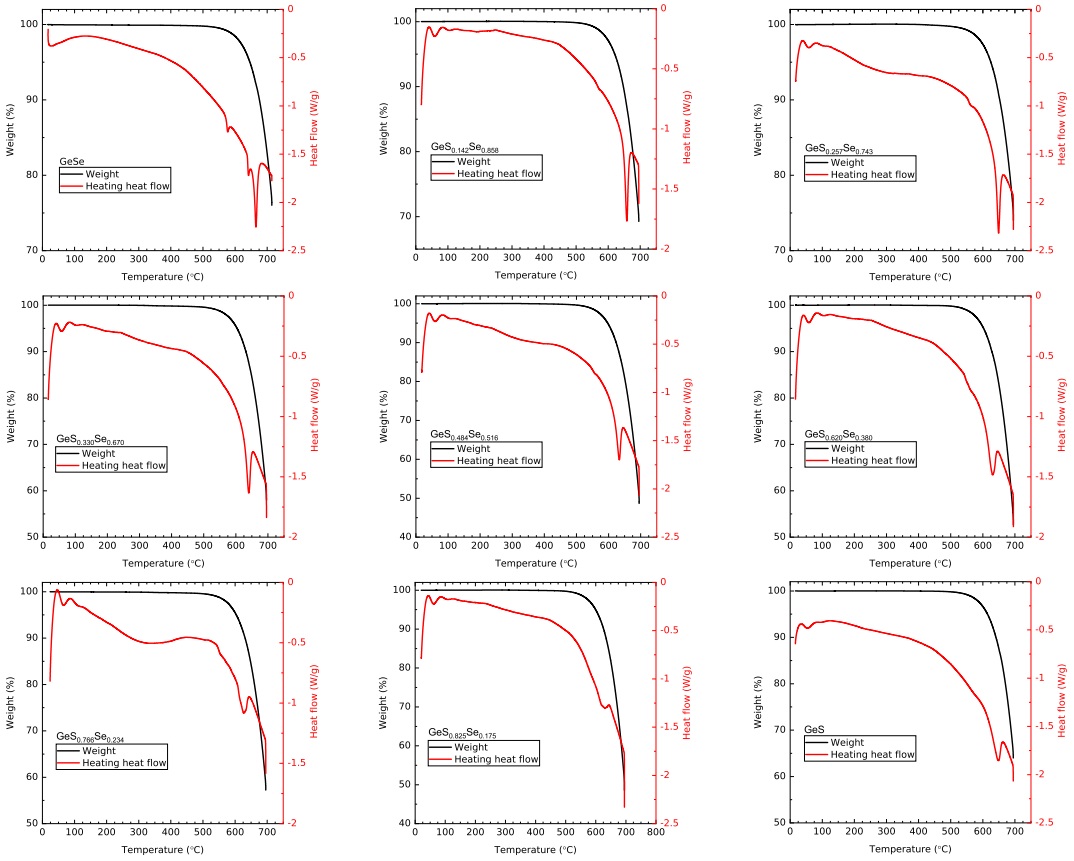

Figure 4.2: *Thermogravimetric analysis and differential scanning calorimetry (TGA/DSC) measurements for GeS_xSe_{1-x} compositions with (a) $x = 0.000$, (b) $x = 0.142$, (c) $x = 0.257$, (d) $x = 0.330$, (e) $x = 0.484$, (f) $x = 0.620$, (g) $x = 0.766$, (h) $x = 0.825$, and (i) $x = 1.000$.*

first endothermic transition at 576°C can be explained as the conversion of α-GeSe to β-GeSe. These two phases are both in the *Pnma* space group but have different lattice parameters. The lattice parameters of the room-temperature α-GeSe structure measured in this work are a = 10.839(10) Å, b = 3.8352(3) Å and c = 4.40(2) Å, while those of β-GeSe have been reported as a = 8.0892(6) Å, b = 3.8261(3) Å and c = 5.8089(5) Å. [224] This phase transition is present from GeSe to $GeS_{0.766}Se_{0.234}$, with the temperature of the transition decreasing to 552°C in the latter. The second endothermic transition at 641°C can be explained as the conversion from the orthorhombic β-GeSe to cubic GeSe. This transition is not apparent for the GeS_xSe_{1-x} solid solutions or for GeS. The third endothermic transition corresponds to the melting point of GeSe at 665°C. GeS shows a single endothermic transition at 647°C, which can be assigned to the melting point, and is slightly lower than previous reports. [222, 223] We were unable to find any literature reports of the thermal properties of the GeS_xSe_{1-x} system.

The melting points for each composition are shown in Table 4.2. Comparison of the melting points in Figure 4.1(b) shows that GeS_xSe_{1-x} is bowing between the two end points, which has not previously been reported. The composition with the minimum melting temperature was found to occur at $GeS_{0.766}Se_{0.234}$, for which the melting point is (626±2)°C.

The calculated Helmholtz free energies of mixing as a function of temperature and composition, computed from the lattice energies of the configurations in the supercell model, are presented in Figure 4.1(c). For an ideal solid solution, the mixing would be purely entropic and the Helmholtz free energy would be symmetric around $GeS_{0.5}Se_{0.5}$. The mixing profiles show noticeable skew at low temperature but become more symmetric with increasing temperature, indicating a small enthalpic contribution to the mixing and thus a small deviation from ideality. Calculating the melting point of a material is challenging as it in principle involves comparing the Gibbs free energies of both the solid and liquid phases, and constructing an accurate model of the latter would be computationally very demanding. We are therefore unable to compare the calculations directly to the thermal analysis. However, we note that the near-ideal solid-solution behaviour predicted from theory is consistent with the formation of a homogeneous solid solution as evident from the experimental measurements.

4.4.3 Structure comparison

Figure 4.3(a) shows XRD measurements performed on powders of each of the alloy compositions. The continuous shift in the 111 and 400 peak positions between the two endpoint compositions, highlighted in the expansion of the 30°-35° range shown

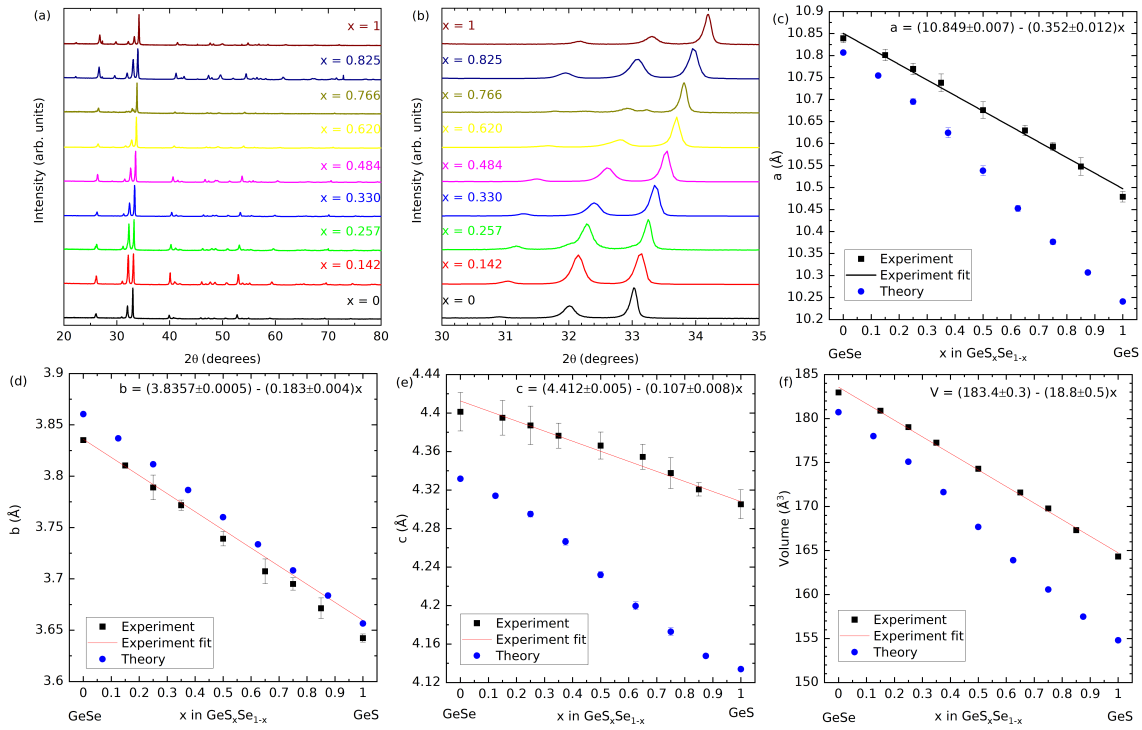

Figure 4.3: *Powder XRD of the nine GeS_xSe_{1-x} powders (a) and an expansion of the 30°-35° range to show the peak shifts with composition (b). The lattice parameters a, b and c of the Pnma structure derived from the powder XRD measurements are shown in (c), (d) and (e) respectively and the corresponding cell volumes are shown in (f). All measurements were performed at ambient temperature.*

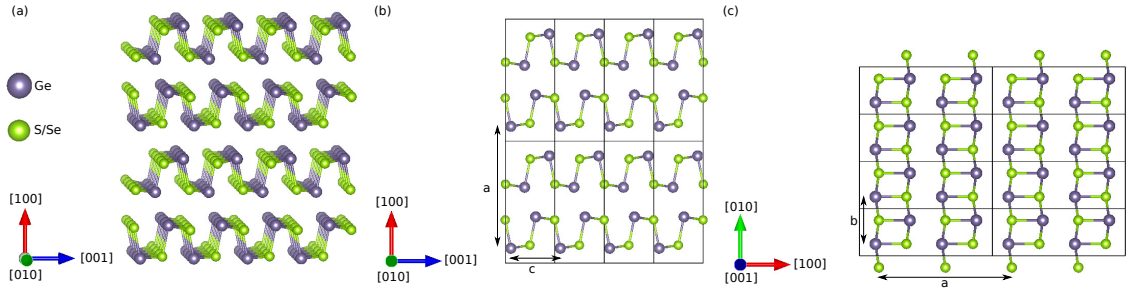

Figure 4.4: *(a) The nanosheet structure of the GeS_xSe_{1-x} series with covalent bonds in two direction ([010] and [001]) and van der Waals interactions in the other ([100]). (b) and (c) show the a, b and c lattice parameters on the crystal structure with the boxes representing one unit cell. These images were prepared using the VESTA software[157] with the crystallographic information file from Ref. 225.*

in Figure 4.3(b), provides further evidence that our growth method yields solid solutions with no significant phase separation. If instead the powders corresponded to physical mixtures, we would expect to observe distinctive peaks corresponding to GeS and GeSe.

The 201, 111 and 400 were used to calculate the lattice parameters using Bragg's law, which are presented in Table 4.2 and compared in Figure 4.3(c)-(f). A list of the peak positions and a summary of the analysis can be found in the Supplementary Information. We performed linear fits to the three lattice parameters (shown in Figure 4.4(b) and 4.4(c)) and the cell volume to obtain the following results:

$$a(x) = 10.849 \pm 0.007 - (0.352 \pm 0.012)x \tag{4.2}$$

$$b(x) = 3.8357 \pm 0.0005 - (0.183 \pm 0.004)x \tag{4.3}$$

$$c(x) = 4.412 \pm 0.005 - (0.107 \pm 0.008)x \tag{4.4}$$

$$V(x) = 183.4 \pm 0.3 - (18.8 \pm 0.5)x \tag{4.5}$$

where the lattice parameters are in Å and the cell volume is in $Å^3$. The R-squared values for a, b, c and volume are 0.993, 0.993, 0.972 and 0.997, respectively.

The experimental lattice parameters presented for GeS and GeSe were consistent with previous literature. [165, 166, 222] Our previous single crystal XRD measurements on GeSe [225] yielded lattice parameters $a = 10.833(2)$Å, $b = 3.8355(7)$Å and $c = 4.3954(5)$Å, which also align with the values determined from the XRD measurements in the present study.

Figure 4.3(c)-(f) also show the lattice parameters and cell volumes predicted from the alloy model. All show a linear variation in the lattice parameter with increasing Se content, which is consistent with the measurements. However, while the predicted variation in the b-axis length shows a similar rate of change to the measurements,

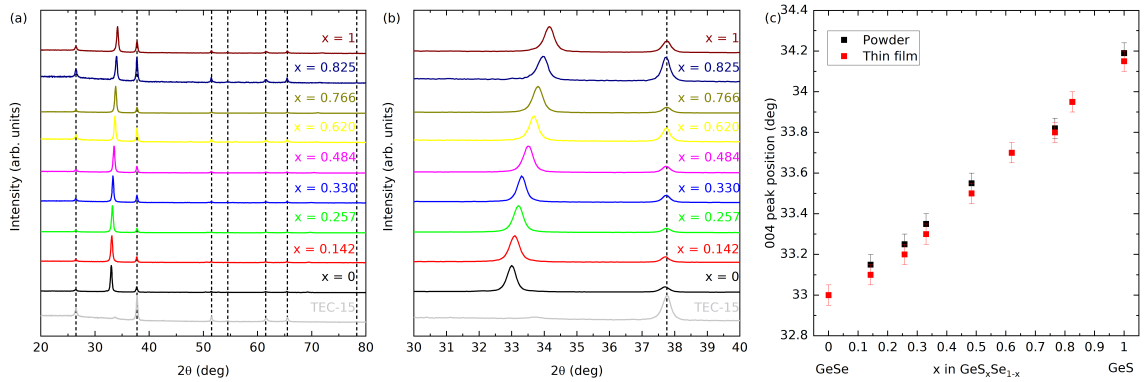

Figure 4.5: *(a) Thin film XRD measurements on the nine GeS_xSe_{1-x} thin films collected at ambient temperature. The vertical dashed lines indicate the positions of SnO_2 XRD peaks from the TEC-15 SnO_2/glass substrates. (b) Expanded view of the XRD over the range 30° to 35° to show the peak shift with composition. (c) Comparison of the (400) XRD peak position in the powders and thin films as a function of composition.*

the predicted a and c parameters show a steeper decrease. This means that the predictions are further away from the experiment at the GeS endpoint than the GeSe endpoint. It is worth noting that the theory predicts the athermal lattice parameters at 0 K and therefore does not account for thermal expansion at finite temperature, which may explain some of the difference. [226]

4.4.4 Thin film XRD

Figure 4.5(a) shows thin-film XRD measurements for each composition. Figure 4.5(b) shows the the continuous shift of the (400) peak as a function of composition between the two endpoints, similar to Figure 4.3(b), which again confirms that the GeS_xSe_{1-x} alloys are deposited as solid solutions with no phase separation. All of the film samples show SnO_2 diffraction peaks, indicated by dashed vertical lines on Figure 4.5(a), due to the TEC-15 SnO_2/glass substrates. The GeS_xSe_{1-x} XRD peaks indicate strongly preferred (100) orientation. The main peak is due to the (400) reflection between 33° and 34.1°. All of the samples also show a systematic shift of the (800) peak between 69.3° and 71.9°, although this peak has a much weaker intensity. The (600) peak is present for the early compositions in the series from x=0 to x=0.330 at 50.3° to 50.9°, but later in the series this overlaps with a peak from the TEC-15 SnO_2/glass (FTO) substrate. Some of the films have one or two low-intensity peaks related to other reflections, but none that appear consistently across the series.

The preferred (100) growth orientation has consistently been observed for GeSe for a variety of preparation techniques, including thermal evaporation, magnetron sputtering and the more novel rapid thermal sublimation. [227–232] Previous theo-

retical studies have shown that for GeSe the total energy of the (100) plane is lower than the other prominent (110), (111), (311), and (511) planes. [227] However, thin-film XRD measurements of ternary GeS/GeSe alloys and of GeS are lacking in the literature. The implications of this for the materials in PV are discussed more in Section 5.4.5.

Finally, Figure 4.5(c) compares the positions of the 400 XRD peak of the thin-film samples with those measured for powders. As the peak positions of the two types of sample coincide within their respective uncertainties, we conclude that the films have the same composition as the powders from which they were deposited, i.e. no preferential loss of S or Se occurs during the thermal evaporation process.

4.4.5 Optics

GeSe band gap updated

The absorption spectra, $(\alpha h\nu)^2$ versus $h\nu$, are shown in Figure 4.6(a) for the temperature range 70 K to 280 K. Details of how these measurements were taken can be found in Section 3.3. By extrapolation to the $(\alpha h\nu)^2 = 0$, an optical transition of 1.301±0.004 eV is found at 300 K. This suggests a maximum solar cell power conversion efficiency of 32.6% based on the detailed balanced limit. [128, 129] Identification of the initial relatively weak absorption onset with absorption coefficent rising to $\sim 1.5\times10^4$ cm^{-1} by ∼1.5 eV (as shown in the inset of Figure 4.6(a)) was informed by comparison with the calculated joint density of states (JDOS), which is discussed below, as shown with the 70 K experimental data in Figure 4.6(b). There is a stronger absorption onset at ∼1.6 eV, for which the absorption coefficent rises to $\sim 6\times10^4$ cm^{-1} by ∼1.8 eV. This strong onset is apparent in both the experimental absorption data and the calculated JDOS using the HSE06+D3 level of theory. This is an interesting finding for photovoltaic applications – while the direct nature and size of the band gap appears to be optimal based on the detailed balanced limit, the weakness of the initial absorption onset suggests that GeSe has non-ideal optical properties for solar cells. The steepness of the absorption onset is often not considered when screening for potential photovoltaic absorbers, but is a key property. The experimentally determined absorption is compared to the theoretically calculated JDOS in Figure 4.6(b) and discussed further below.

In Figure 4.6(c), the temperature dependence of the band gap, $E_g(T)$, is analysed with the Varshni relation[233]:

$$E_g(T) = E_g(0) + \frac{\alpha T^2}{\beta + T} \tag{4.6}$$

where $E_g(0)$, α and β are fitting parameters. The typical Varshni-like temperature

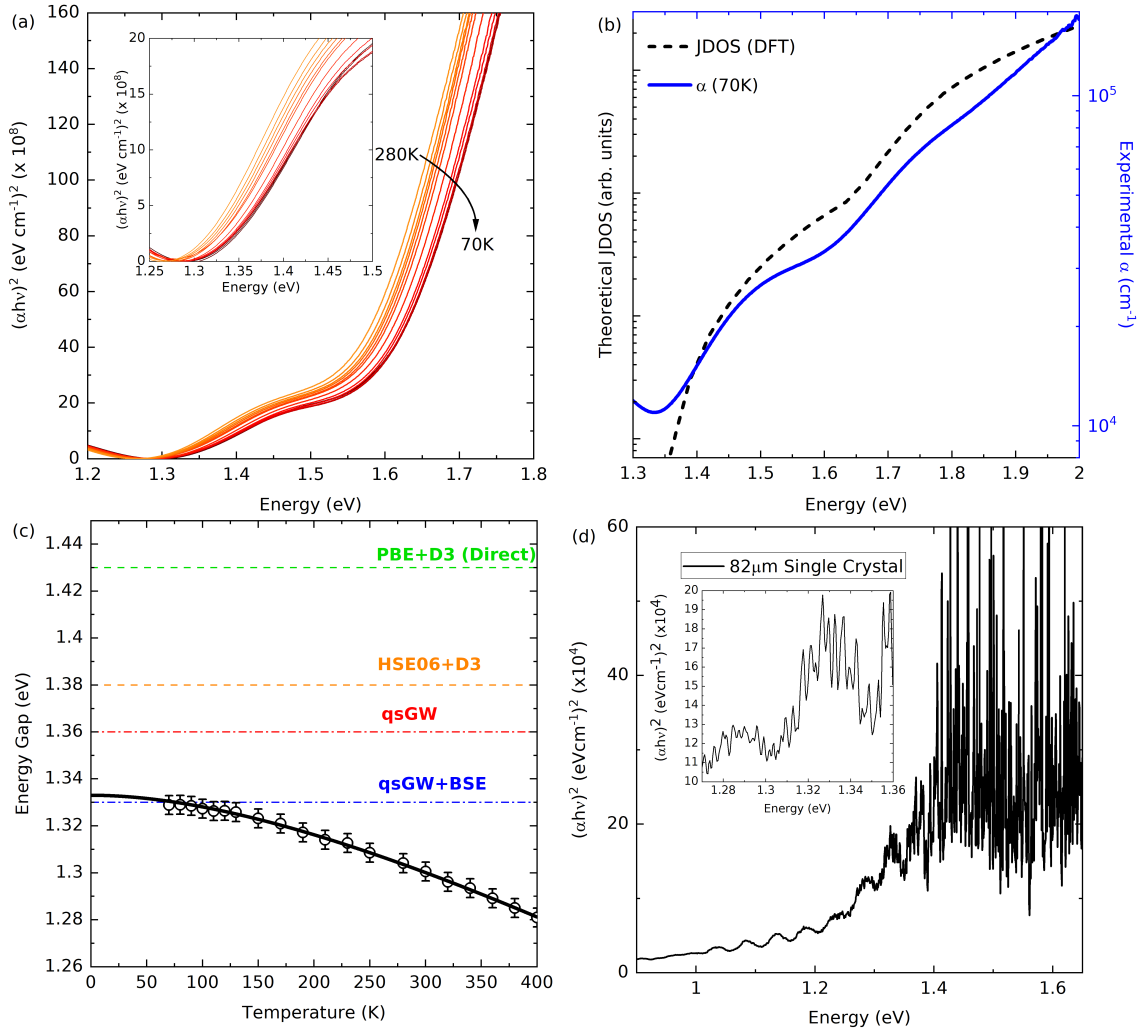

Figure 4.6: *(a) Optical absorption spectra of the 400 nm GeSe thin film for the temperature range 70–280 K, plotted as $(\alpha h\nu)^2$ versus $h\nu$. The inset shows the weak initial absorption onset; (b) The 70 K experimental absorption data, showing the weak absorption onset at ∼1.33 eV followed by the strong absorption onset at ∼1.6 eV, along with the calculated joint density of states (JDOS) derived from the HSE06+D3 band structure - both are plotted with a logarithmic y-axis. To account for the difference between HSE06+D3 and qsGW +BSE fundamental band gaps, the JDOS is shifted to 0.05eV lower energy; and (c) The variation of the direct band gap as a function of the temperature between 70 and 400 K fitted by the Varshni relation. The fundamental direct band gaps calculated with successively higher levels of theory are shown as horizontal lines. Note that PBE+D3 predicts an indirect band gap, but the smallest direct transition from that level of theory has been included here for comparison. (d) $(\alpha h\nu)^2$ versus $h\nu$ for the 82 μm-thick GeSe single crystal, assuming a direct allowed absorption onset. The inset shows the same data zoomed into the range of 1.27 eV to 1.36 eV. In this range there are clear oscillations consistent with the thickness of the cleaved single crystal.*

dependence of the band gap is observed due to thermal expansion and electron-phonon interactions.[233] The Varshni fit yields $E_g(0)$, α and β parameters of 1.333±0.003 eV, 2.3 $\times 10^{-4}$ eV K^{-1}, and 478 K respectively. The different values of the direct band gaps found from different theoretical calculations are also presented on the Figure. These results are discussed further below, but it can be seen that the value of $E_g(0)$ is in excellent agreement with the fundamental direct band gap found by qsGW+BSE.

In spite of previous reports suggesting an indirect band gap, the Tauc-like analysis in Figure 4.6(a) is performed under the assumption that the direct allowed transition dominates the absorption. For many conventional III-V, II-VI compound semiconductors (eg. GaAs and CdTe) and elemental group IV semiconductors (eg. Si), the nature of the band gap can be determined by plotting $(\alpha h\nu)^m$ versus $h\nu$ where $m = 2$ and $m = 1/2$ give a linear onset for the cases of direct and indirect fundamental band gaps, respectively. [234, 235] In these cases, the manifestation of the fundamental transition in optical spectra is unencumbered by other transitions that occur at significantly higher energies. For many other semiconductor materials, such as GeSe, there are many direct and indirect transitions within a few hundred meV of the fundamental band gap. Therefore, determining whether the fundamental band gap is direct or indirect is extremely challenging from optical absorption measurements. In such a scenario, the direct transitions will dominate absorption spectra due to their much greater probability. Therefore, no claims to have experimentally determined the nature of the fundamental band gap of GeSe are made here. Additionally, this approach is supported by the theoretical results reported below, which all indicate direct and indirect transitions within close energy proximity.

The absorption spectra of the single crystal (see Figure 4.6(d)) reveals a much weaker absorption feature, with an onset that begins around 1.0 eV and an absorption coefficient of 150 cm^{-1} by 1.4 eV. This is consistent with other aforementioned reports of single crystals within the literature,[199, 200] which are often cited as the band gap for GeSe. However, we suggest the absorption onset manifests itself at a lower photon energy for the single crystals (here and in the literature) due to sub-gap phenomena such as Urbach tailing and defect-related absorption. In this lower energy region, due to the low absorption coefficient, a portion of photons are permitted to transmit through a thick sample. However, the higher energy photons will be very efficiently absorbed, making it impossible, for thick samples, to probe the direct onset at 1.3 eV. This is an obvious benefit of this work focusing primarily on thin films. This, therefore, supports this interpretation that the fundamental band gap is higher than previously reported and the lower energy onsets found for bulk crystals are due to the fact that no light can be transmitted through thick crystals in the high-absorption-coefficient region of the spectrum.

Table 4.3: *Calculated lattice parameters of GeSe, with percentage differences from the experimental lattice parameters obtained in this work from refinement of the experimental XRD data collected at 250.7 K.*

	a (Å)	b (Å)	c (Å)
PBE+D3	3.884 +1.265%	4.486 +2.061%	11.014 +1.671%
HSE06+D3	3.811 −0.64%	4.451 +3.31%	10.950 +1.08%

The GeSe lattice parameters obtained from DFT relaxations with the PBE+D3 and HSE06+D3 methods differ from those determined experimentally; these are summarised for the two methods in Table 4.3. Both calculation methods show some difference from the 250.7 K experimental values – both give b parameter values over 2% higher than experiment, with HSE06+D3 differing more than PBE+D3. The other two calculated lattice parameters are closer to the experimental values – HSE06+D3 reproduces a within 1%, while PBE+D3 overestimates by just over 1%, while in c, HSE06+D3 more closely reproduces the experimental parameter. Neither geometry optimisation appears to more closely replicate the experimental structure overall, and hence electronic band structures were calculated using both relaxed structures.

The HSE06 band structures on each of the two relaxed structures are depicted in Figure 4.7. The majority of the band structure of GeSe is very similar regardless of the geometry optimization, with the conduction band minimum occurring at Γ in both, except for a key difference in the crucial Γ to Y path (corresponding to the **c** direction in the *Pnma* cell). In the PBE+D3-optimized structure, the valence band maximum (VBM) occurs away from the high symmetry points and GeSe is predicted to be an indirect semiconductor, in line with previous GGA calculations, while with HSE06+D3 structure, the VBM occurs at Γ, meaning the fundamental band gap is direct. Nevertheless, in both cases the magnitude of the fundamental band gap of bulk GeSe is similar to each other, and higher than previously assessed by GGA-DFT, with $E_g^i = 1.34$ eV for the PBE+D3 structure, and with the lowest direct transition at Γ only slightly higher at 1.43 eV, while $E_g^d = 1.38$ eV for the HSE06+D3 structure.

To confirm that HSE06 is accurate in its determination of the band gap, we further compare to high-level qsGW calculations performed within the `Questaal` package at a similar k-point density. In both cases, the qsGW band structure (Figure 4.8) is found to compare very closely (with the indirect/direct band gaps within 20 meV) to the HSE06 electronic structure calculated at that same geometry. The direct band gap feature in the HSE06+D3 band structure is retained in the qsGW

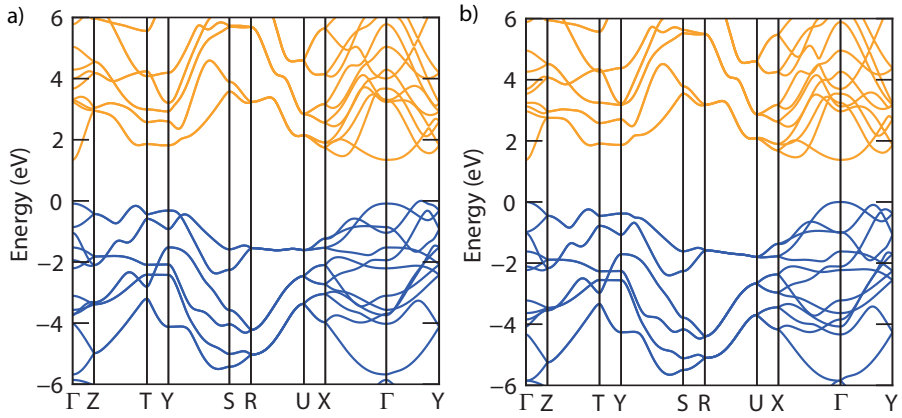

Figure 4.7: *HSE06 electronic band structures of GeSe on the structures relaxed using a) PBE+D3 and b) HSE06+D3. Valence band is in blue, conduction band in orange and $E = 0$ eV is set to the valence band maximum.*

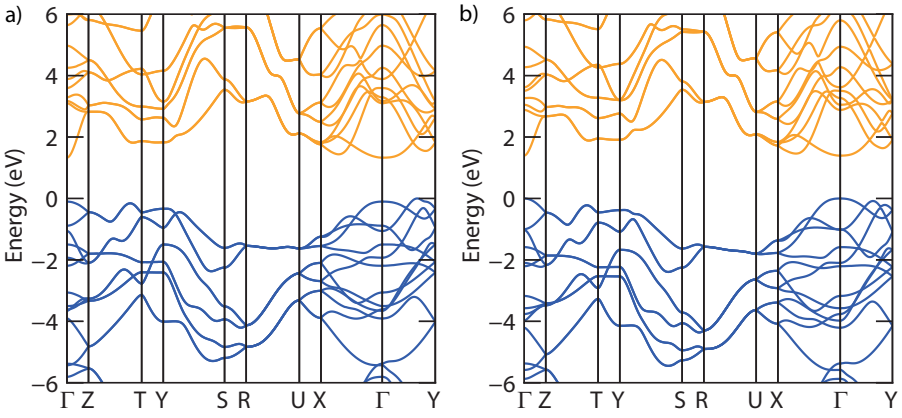

Figure 4.8: *qsGW electronic band structures of GeSe on the structures relaxed using a) PBE+D3 and b) HSE06+D3. Valence band is in blue, conduction band in orange and $E = 0$ eV is set to the valence band maximum.*

calculation, further confirming that this feature is structurally driven. The resultant band gap here is found to be direct with a value of 1.36 eV. Further, the error within qsGW quasiparticle band gaps is systematic. For simple semiconductors, like GeSe, without large spin fluctuations, its primary error arises from the omission of higher-order 'ladder' diagrams when determining the contributions of the screened Coulomb interaction, W. To quantify this effect, GeSe was calculated (at the HSE06+D3 structure alone, due to the significant computational cost) with qsGW+BSE. The resultant band gap was found to be 1.33 eV, only 30 meV lower than the original qsGW gap. Encouragingly, the calculated ground state direct band gaps converge to the 0 K experimental value as the computational cost increases, as demonstrated in Figure 4.6(c).

While the fundamental band gap of GeSe is optimal for a solar absorber, as mentioned above, the weak initial absorption onset is not ideal for photovoltaics. The weak absorption onset observed in Figure 4.6(b) is due to the low joint density of states associated with the dispersive band extrema of both the conduction and valence bands, as is apparent in the calculated band structures shown in Figures 4.7 and 4.8. The validity of the theoretical findings is supported by the agreement between the experimental and theoretical results shown in Figure 4.6 and a comparison is also shown in Table 4.4.

	E_g (eV)	Strong absorption onset energy (eV)
Experiment, thin film (70K)	1.329±0.004[a]	1.56±0.03
HSE06+D3	1.38	1.60
qsGW +BSE	1.33	1.55

[a]A very weak onset was measured at ∼1.0 eV for the bulk GeSe crystals, with the absorption coefficient not exceeding 150 cm^{-1} below the fundamental band gap at 1.3 eV (supplementary Figure S4) - it is not fundamental and, as discussed, comes from Urbach tailing/defects.

Table 4.4: *Experimental and calculated fundamental band gap, E_g, and strong absorption onset energy.*

The success of the theoretical approach employed here for GeSe suggests that using a combination of the HSE06+D3 method to calculate the structure and the qsGW+BSE level of theory for optical properties is an appropriate procedure for obtaining accurate first principles descriptions of vdW materials. Additional equivalent studies on a range of semiconducting vdW materials would be desirable to evaluate this procedure further.

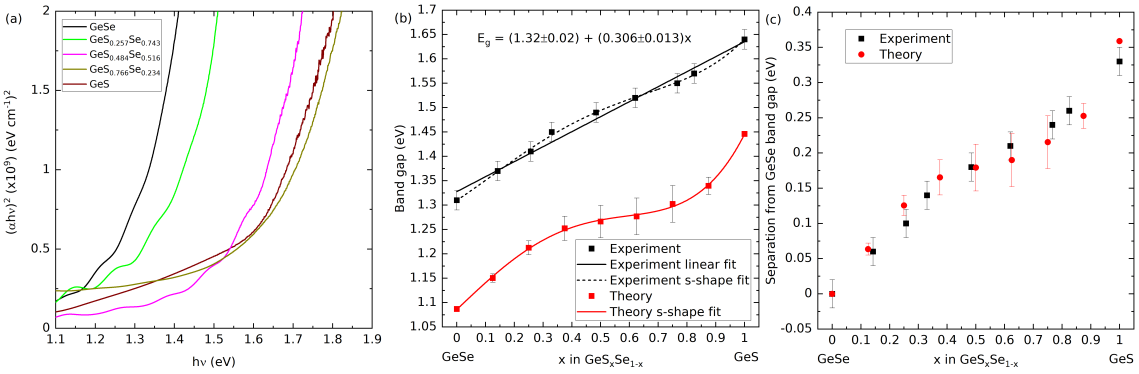

Figure 4.9: *(a) Optical absorption $(\alpha h\nu)^2$ as a function of photon energy $h\nu$ for the x = 0, 0.257, 0.484, 0.766 and 1 compositions in the GeS_xSe_{1-x} series. Data for the remaining compositions is provided in the Supplementary Information. (b) Comparison of the measured and calculated band gaps as a function of composition. The experimental data is fitted to a linear trendline, for which the fitting parameters are shown on the plot, and both sets of data are fitted to s-shaped curves as a guide to the eye. (c) Measured and predicted change in band gap as a function of composition relative to the GeSe endpoint.*

Optical properties of GeS_xSe_{1-x}

The measured optical absorption spectra $(\alpha h\nu)^2$ as a function of the photon energy $h\nu$ are shown in Figure 4.9(a) for x = 0, 0.257, 0.484, 0.766 and 1. The remaining compositions are not included on the Figure for ease of viewing the data. As discussed previously for GeSe, the optical analysis is performed under the assumption of direct transitions dominating the absorption. [225] This is supported by band structure calculations, which show several direct and indirect transitions within a few hundred meV of the fundamental band gap. Therefore, one can derive the smallest direct transition for each of the compositions, but as above it cannot be used to establish the nature on the fundamental band gap.

The stronger onset dominates the optical absorption data and makes identifying the initial onset more challenging. Optical absorption data is typically analysed under the assumption that the lowest direct gap transitions dominate, as analysed in the previous section. If there is a single transition between parabolic conduction and valence bands, then $(\alpha h\nu)^2$ versus $h\nu$ is linear. However, that approach does not work when there are multiple transitions close to the band gap, as they combine to give a non-linear onset. In order to estimate the fundamental band gap, the $(\alpha h\nu)^2$ versus $h\nu$ data were inspected and the third derivative taken. Using the third derivative to identify the critical points of a band structure is rigorously justified for modulation reflectance optical spectroscopies, and also has some benefit for identifying features in optical absorption data. [236, 237]

The derived band gaps are listed in Table 4.2 and plotted as a function of composition in Figure 4.9(b). The band gap can be seen to vary approximately linearly with

composition across the GeS_xSe_{1-x} series, and a linear fit can be performed within experimental error giving $E_g(GeS_xSe_{1-x})=(1.320\pm0.020)+(0.306\pm0.013)x$. The R-squared value of this fit is 0.985. Typically, the band gaps for alloy series either vary linearly or exhibit "bowing" depending on the electronegativity and size difference between the atoms being mixed, with a higher electronegativity difference as in ZnO_xS_{1-x} and $GaN_{1-x}Sb_x$ giving a larger bowing parameter. [238, 239] Given the chemical similarity between sulfur and selenium, an approximately linear variation in the band gap seems reasonable.

The smallest predicted direct transitions for the endpoint compositions are in good agreement with the experimentally measured direct band gaps. For GeS and GeSe, the predicted smallest direct transition are 1.714 eV and 1.355 eV, respectively. The predicted band gaps obtained from the theoretical alloy model (Figure 4.9(b)), which are calculated as a weighted average of the predicted band gaps for each of the supercell structures with a given composition, appear to be offset to lower energies. However, the band-folding in the supercells means that the distinction between direct and indirect transitions is effectively lost, and the predicted band gaps are therefore simply calculated as the lowest-energy transitions in the joint density of states. Based on the band structures calculated at this level of theory for the endpoints, these are likely to be indirect transitions.

Furthermore, the experimental band gaps measured with absorption spectroscopy also account for the momentum matrix elements, which are not considered in the DFT-determined values. Either or both of these could account for the discrepancy between the DFT and experimental band gaps.

The DFT-calculated band gap versus composition shows an unusual s-shaped trend. From the atom-projected electronic density of states (see Figure 4.10), this appears to be caused by interactions between the Se $4p$ and S $3p$ states at the valence band edge. This trend is also reflected in the experimental results, but is less pronounced. Taking the GeSe band gap as a reference point and comparing the change in the measured and predicted band gaps with composition shows a very similar trend (Figure 4.9(c)), suggesting that the difference between the measured and predicted band gaps can largely be accounted for with a constant shift. Therefore, while a straight line provides a good fit to the experimental band gap variation with alloy composition, the weak s-shaped dependence could be a real phenomenon and so requires further investigation.

Based on the detailed balance limit, the Se-rich end of the series has a band gap ideal for a single-junction solar cell, [128] and the S-rich end of the series is close to the ideal for a two-junction tandem solar cell when paired with a Si absorber layer. [142]

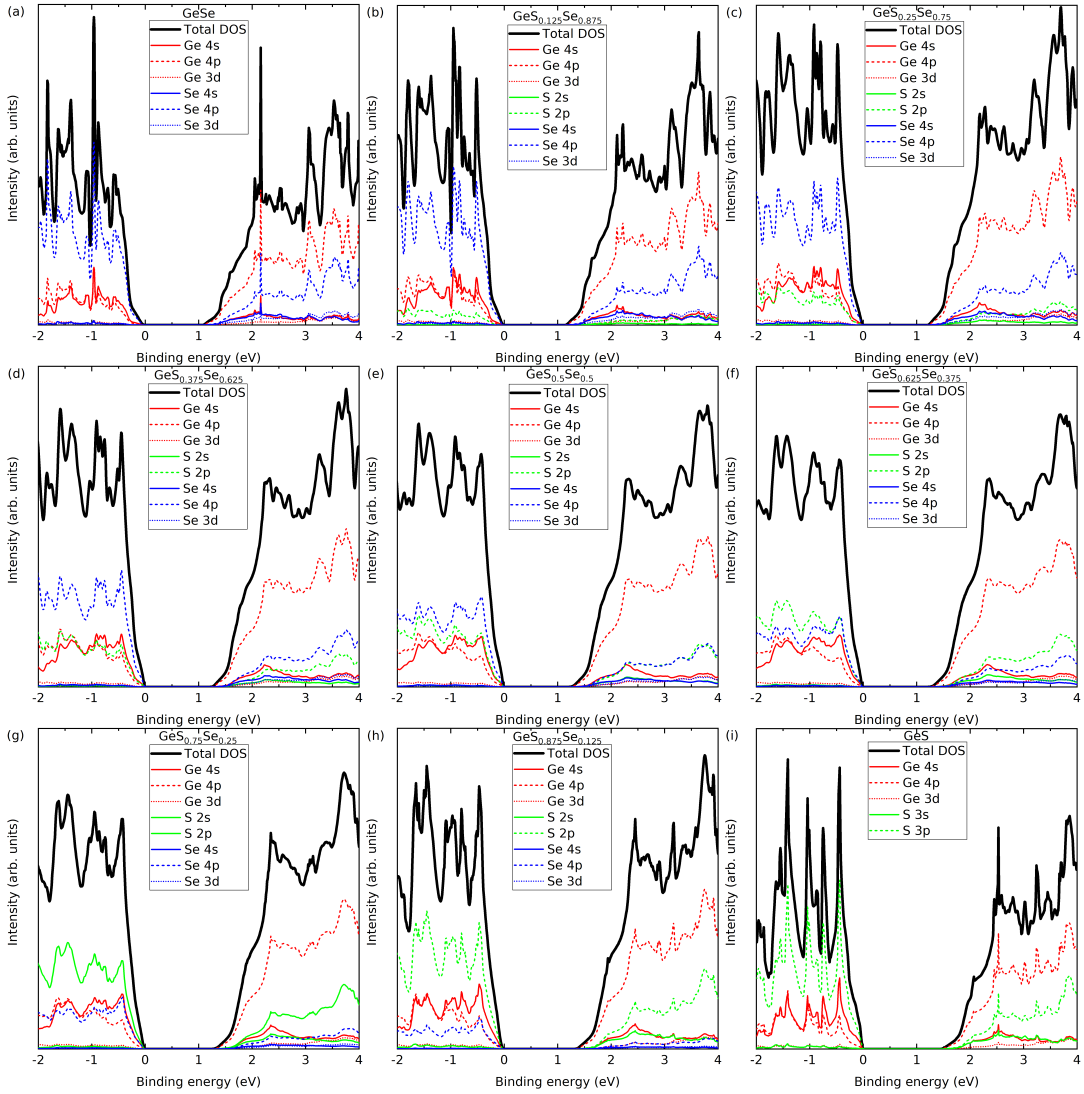

Figure 4.10: *Calculated total and atom-projected electronic density of states $g(E)$ for GeS_xSe_{1-x} compositions with (a) $x = 0$, (b) $x = 0.125$, (c) $x = 0.25$, (d) $x = 0.375$, (e) $x = 0.5$, (f) $x = 0.625$, (g) $x = 0.75$, (h) $x = 0.875$, and (i) $x = 1$.*

4.5 Conclusion

Nine different compositions of GeS_xSe_{1-x} bulk crystals have been grown by a melt growth technique and the compositions determined using ICP-OES. The bulk powders made from pulverised bulk crystals were used to grow thin films by thermal evaporation at room temperature but annealed after deposition. These samples were characterised experimentally and compared to theoretical calculations on a supercell model of the alloy performed using density-functional theory.

The melting point bows between the two endpoints of the powders; the GeS_xSe_{1-x} has a minimum of 626°C at $GeS_{0.766}Se_{0.234}$. Lattice parameters measured using XRD show a linear trend between the two endpoints, which is consistent with the predictions from the alloy model. The measurements and theory agree reasonably well for the GeSe endpoint, but the model underestimates the a and c parameters at the sulfur-rich end of the series. The thermal and structural sets of experiments indicate the formation of a homogeneous solid solution, which is supported by theoretical mixing free energy profiles, demonstrating that the formation of the solid solution is predominantly driven by entropy.

A case study of the optical properties of the GeSe endpoint was also performed theoretically and experimentally. The theoretical study suggests the fundamental band gap is direct. Under the assumption of a direct band gap, experimental absorption spectra from thin films indicate a value of 1.301±0.004 eV at 300 K, somewhat larger than the widely quoted value of 1.1–1.2 eV for the fundamental band gap. Previous optical absorption results suggesting lower band gaps with low absorption coefficients have been understood to be artefacts of measurements of very thick crystals for which light is not transmitted in the direct absorption onset region of the spectrum. Hybrid density functional theory calculations (HSE06), with the Grimme correction (D3) used to account for the vdW interactions, suggest a band gap that is direct with a value of 1.38 eV at 0 K. Additionally, quasiparticle self-consistent GW approximations (using the structure from the HSE06+D3 calculations) also give a fundamental direct band gap, but with a value of 1.36 eV. Further to this, when the BSE correction is applied to the qsGW, a smaller direct band gap of 1.33 eV is calculated. With increasing computational cost, the different theoretical approaches converge towards the experimentally obtained value of 1.333±0.003 eV for the 0 K fundamental band gap. As well as this, the shape of the theoretical JDOS is consistent with the low temperature experimental optical absorption spectra, with both exhibiting an onset ∼0.3 eV above the initial absorption edge.

The smallest direct optical transitions were measured for the entire alloy series and a linear fit found to give band gaps $E_g(GeS_xSe_{1-x})=(1.320\pm0.020)+(0.306\pm0.013)x$ for the series. While the measurements could not be directly compared to theoret-

ical predictions, the alloy model was found to give a good prediction of the change in band gap with composition relative to the GeSe endpoint.

The formation of a solid solution across the composition range, combined with the range of band gaps observed, indicate that GeS_xSe_{1-x} alloys have potential for solar cell applications where tunable band gaps are beneficial. The extensive comparison between measurements and theory also demonstrates that the alloy model adopted in this Chapter (as well as the comparison in the next Chapter) gives good results, and can therefore potentially be applied to other systems of interest in the future.

Chapter 5

Lone pairs and devices

5.1 Introduction

The previous chapter showed that the GeS_xSe_{1-x} alloys are of interest for PV based on its optical properties. In this Chapter, the presence of active lone pairs for the two endpoints of the alloy series is studied. As discussed in Chapter 2, the stereochemically active lone pair effect has been linked to the success of methylammonium lead iodide solar cells. [240] Furthermore, this effect has also been present for the promising and related PV material, Sb_2Se_3. [133] Showing the presence of stereochemically active lone pairs for GeSe and GeS would further increase the motivation for using the materials in PV.

Additionally in this Chapter, to complete the work investigating the GeS_xSe_{1-x} alloy series for PV applications, some device work for GeSe is presented. GeSe was chosen as a single junction cell as optically it is the closest to the maximum possible efficiency based on the detailed balance limit. [225, 241]

5.2 Literature review

5.2.1 Valence band studies of GeS and GeSe

Early studies on GeS and GeSe identified three key features in the valence band spectrum named Peaks I, II and III (Figure 5.1). It was suggested that Peak I was composed of S $3p$/Se $4p$ and Ge $4p$ orbitals, Peak II of Ge $4s$ orbitals, and Peak III of S $3s$/Se $4s$ states. [242–254] This appears to be based on early speculation linked to the lead chalcogenides that was subsequently propagated in much of the literature. [255, 256] Waghmare *et al.* performed calculations on IV-VI chalcogenides in the cubic (rocksalt) structure and demonstrated that Ge $4s$ states are also present in Peak I at the VBM. [257] Since then, theoretical calculations of orthorhombic GeS have also indicated the presence of Ge $4s$ states at the VBM, but other studies of

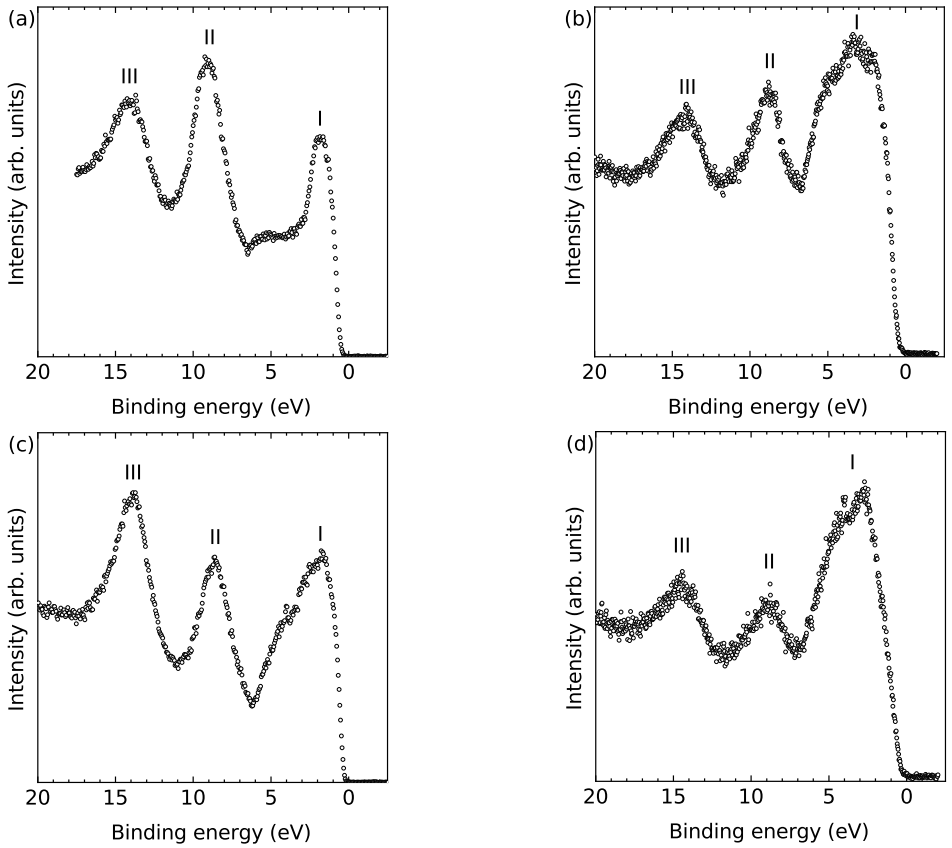

Figure 5.1: *(a) and (b) show HAXPES and XPS measurements of GeS, respectively, while (c) and (d) show HAXPES and XPS measurements of GeSe. Peaks I, II and III are labelled to correspond to how they are referred to in early reports on the valence bands of GeS and GeSe. Peak I was initially thought to be composed of S 3p/Se 4p and Ge 4p orbitals, Peak II of Ge 4s orbitals, and Peak III of S 3s/Se 4s states.*

GeS are limited to monolayers and amorphous materials, the electronic structures of which differ significantly from the electronic structures of bulk crystals. [258–261] Theoretical calculations on orthorhombic GeSe have also suggested that the Ge 4s orbitals contribute to the VBM, with one study loosely comparing the calculated density of states to XPS measurements of the valence band spectra. [167, 262, 263] GeS and GeSe are known to adopt distorted crystal structures, [264] and theoretical studies on both have demonstrated the asymmetric electron densities expected in materials with stereochemically active lone pairs. [258, 261, 265] However, neither material has been studied using HAXPES, and this would be the most effective method for confirming the presence of Ge 4s states at the VBM.

Beyond the germanium chalcogenides, studies of Ge 4s lone pairs remain limited. While Ge(II) would appear to be an alternative to Pb(II), in perovskite materials it has largely been overlooked due to the lower binding energy of the Ge 4s electrons compared to the Sn 5s and Pb 6s electrons. [266] Mitzi has previously shown that in crystals of $(C_4H_9NH_3)_2MI_4$ perovskites (M = Ge, Sn, Pb) the stereochemical activity of the lone pair was strongest in the Ge materials. [267] Despite this, it is generally accepted that the lone s orbital becomes more stable on descending the group (i.e. $6s^2$ lone pairs are more stable than $4s^2$ lone pairs), [268] and this decreased stability means that Ge perovskites are more prone to oxidation, which further explains the limited studies on these materials. [149] However, with careful preparation, Ge perovskites with stereochemically active lone pairs could prove useful in the development of tandem solar cells given their wide band gaps. A proof of concept study of single-junction Ge perovskite cells has been performed, albeit with a limited efficiency of 0.2%.[269] It has been further demonstrated that other Ge perovskite materials can be made, with multiple studies reporting the successful preparation of crystals of the $CsGeX_3$ (X = Cl, Br, I) perovskite series. [270–273] Theoretical studies of $CsGeI_3$, $(CH_3NH_3)GeCl_3$ and $(CH_3NH_3)GeI_3$ have all shown a contribution from the Ge 4s orbitals to the VBM, again suggesting stereochemically active lone pairs. [269, 273–275]

5.2.2 Doping GeSe

At present, no PV study of GeSe has investigated the impact that doping could have on device performance. GeSe has been reported to be natively p-type. [276, 277] Experimental reports on doping the material are limited to a study of n-type doping using nitrogen and carbon. [278] A theoretical study by Shu and Cai, which explored thirteen elements as possible donors for GeSe, identified Ag as a promising candidate for p-type doping. [279]

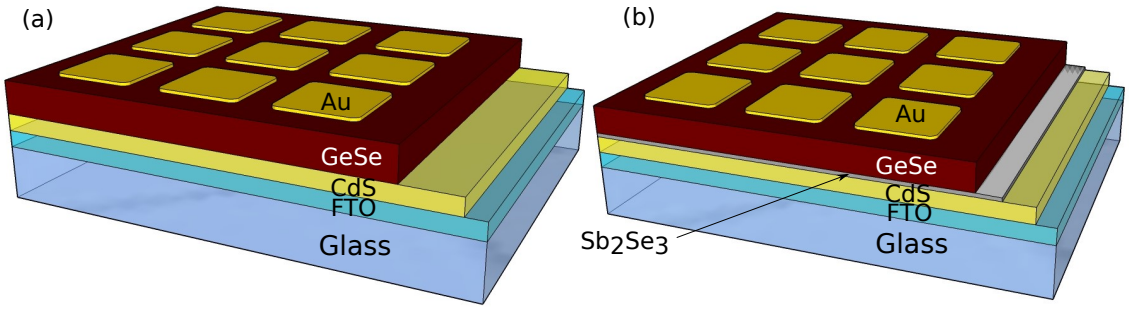

Figure 5.2: *The two different device structures investigated FTO/CdS/GeSe/Au and FTO/CdS/Sb_2Se_3/GeSe/Au. Each device structure was made with both Ag-doped and undoped GeSe versions, making four device configurations in total.*

5.2.3 Device results

GeSe has previously been investigated in PV devices. [280] This has included some theoretical studies that have looked at SnS, SnSe and MAPI as potential partner layers in a heterojunction. [281–285] Furthermore, initial experimental studies by Xue *et al.* showed promising results. A device structure of ITO/CdS/GeSe/Au gave an efficiency of 1.48 %, V_{OC} of 240 mV, J_{SC} of 14.48 mA cm^{-2}, and fill factor of 42.60 %. [230, 232] Further work by Chen *et al.* studying both FTO/CdS/GeSe/C/Ag and FTO/TiO_2/GeSe/C/Ag gave efficiencies of 0.05 % and 0.27 %, respectively. [227, 229] Recently, the efficiencies have seen a significant improvement by incorporating a 10 nm Sb_2Se_3 interfacial layer into the device. [167] The new device structure of ITO/CdS/Sb_2Se_3/GeSe/Au has an efficiency of 5.2%, V_{OC} of 380 mV, J_{SC} of 24.6 mA cm^{-2}, and fill factor of 56 %.

5.3 Experimental methods

The samples used in the lone pair study, the GeS and GeSe samples, and the undoped GeSe in the cell study, were prepared in the same way as described in the previous Chapter. Ag-doped GeSe was grown by the same melt growth technique, with quantities of 1.4371 g of Ge, 1.5627 g of Se, and 0.0002 g of Ag, measured on scales with precision 0.0001 g. The Ag-doped GeSe was loaded with a target composition of 0.01 atomic% doping level, with an Ag/(Ag+Ge) molar ratio of 0.0001. Both mixtures were melted at 800 °C for 48 hours, then cooled to 500 °C at a rate of 0.3 °C min^{-1} where the mixture was held for 100 hours, before finally being cooled to room temperature.

To make the devices, CdS films were deposited on SnO_2:F-coated soda lime glass substrate (TEC15, NSG Group) by RF-magnetron sputtering at 1.32 W cm^{-2}, 5 mTorr of Ar gas and a substrate temperature of 200 °C for 30 minutes to give a film with thickness 100 nm for all devices. For half of the devices, a 10 nm interfacial

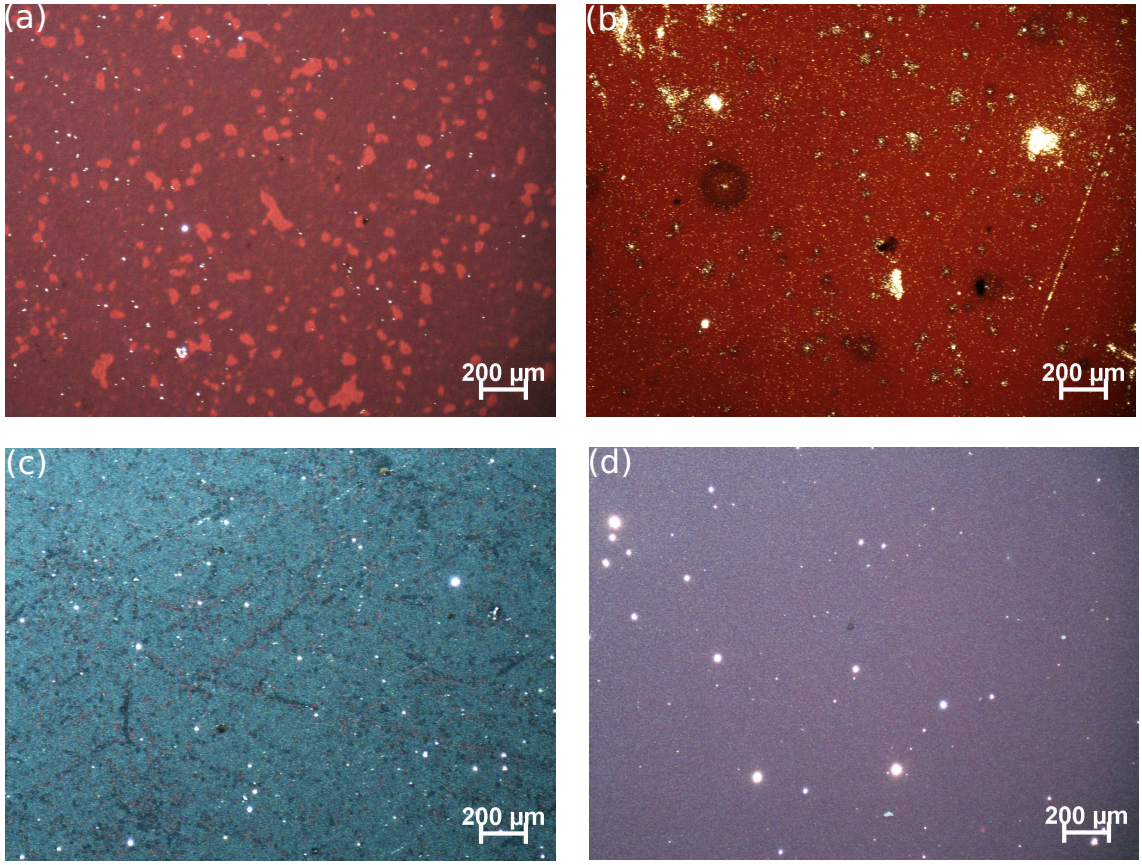

Figure 5.3: *Backlit optical microscope images of devices (a) FTO/CdS/Ag:GeSe (b) FTO/CdS/u:GeSe (c) FTO/CdS/Sb_2Se_3/Ag:GeSe (d) FTO/CdS/Sb_2Se_3/u:GeSe. White spots show pinholes which are blocked from shorting the devices using spin-coated P3HT.*

layer of Sb_2Se_3 was deposited by thermal evaporation at this stage. A Te interfacial layer was also tried but the devices were unsuccessful. Then, 600-800 nm of doped or undoped GeSe was deposited by thermal evaporation. All thermal evaporation deposition thicknesses were monitored using a quartz crystal microbalance (QCM) calibrated with an Ambios XP-200 surface profilometer. At this stage all devices were annealed on a hot plate in a N_2 environment with the annealing temperatures varied as stated below. P3HT was dissolved in chlorobenzene at a concentration of 5 mg ml^{-1} by heating the solution at 70 °C in a N_2 atmosphere for 1 hour. P3HT was then deposited onto the cells by dynamic spin coating in a two step process, with an initial 1000 rpm step (10 seconds) to spread the solution across the device, followed by a 4000 rpm drying step (30 seconds). This was added as a standard pinhole blocker due to the pinholes shown in Figure 5.3. Finally, 50 nm of gold was deposited by thermal evaporation with a mask to make a cell with an active area of 0.1 cm^2. Both device structures are shown in Figure 5.2.

Note, the systematic cell device study here was informed by previous device results. This included different transparent conducting oxides (TCOs), window layers,

and P3HT conditions. These previous device results are not shown here.

HAXPES measurements were collected at beamline I09 at the Diamond Light Source facility, UK in a standard ultrahigh vacuum (UHV) chamber with a pressure of $< 1\times10^{-10}$ mbar. All these measurements were taken across two separate beamtimes, one for the lone pair study and the second looking at the Ag-doped GeSe. For the lone pair study, a Si(004) channel-cut crystal, following a double-crystal Si(111) monochromator, was used to select x-rays from the source ($h\upsilon = 5.921$ keV). For the solar cell study, the hard x-rays used were defocussed with an energy of 6.60 keV selected by a double-crystal Si (111) and Si (004) channel cut monochromator. The soft x-rays were also defocussed with a photon energy of 1.09 keV. The soft x-ray energy was selected using a plane grating monochromator. Measurements were made using a Scienta Omicron EW4000 high-energy analyzer with an acceptance angle of $\pm28°$. For the lone pair study, calibration was performed using a gold sample, enabling the energy resolution of 0.25 eV to be determined by fitting the Fermi edge with a Fermi-Dirac function convolved with a Gaussian peak. The uncertainty in energies was ±0.03 eV for core level peaks. For the solar cell study, the resolution was determined to be 0.27 eV and 0.23 eV for the 6.60 keV and 1.09 keV measurements, respectively.

XPS measurements were performed in a standard UHV chamber with a pressure of $\sim1\times10^{-10}$ mbar. Surface contaminants were removed by sputtering with Ar^+ ions at a 0.3 kV accelerating voltage. The XPS measurements were taken using a SPECS monochromatic Al Kα x-ray source ($h\upsilon = 1.487$ keV) operating at 250 W and a hemispherical PSP Vacuum Technology electron-energy analyzer operating with a typical pass energy of 10 eV. The SEC measurements were taken with reduced power (9 W), reduced slit size in the analyser, and a -10 V bias applied. Calibration was performed using a silver sample, enabling the energy resolution of 0.4 eV to be determined by fitting the Fermi edge data. The uncertainty in energies from XPS was ±0.05 eV for core level peaks and ±0.10 eV for VBM positions.

Scanning electron microscopy (SEM) was performed with a JEOL 6610 microscope at 10kV acceleration voltage.

Undoped and Ag-doped GeSe powder and thin film XRD measurements were performed using a Panalytical X'pert Pro instrument with a rotating cobalt anode, under ambient conditions. Monochromated incident radiation (Co Kα_1) was used to perform θ:2θ scans carried out between 25 ° and 95 ° in parallel beam geometry for both powder and film measurements.

Current-voltage (JV) measurements were performed to measure the power conversion efficiency (PCE) of all devices. The measurements were completed under AM1.5 illumination provided by a TS space systems solar simulator calibrated by a photodiode. External quantum efficiency (EQE) measurements were completed

using a Bentham PVE300 characterization system. Capacitance voltage (CV) measurements were carried out using a Boonton 7200 Capacitance Meter in ±500mV range.

Electronic structure calculations performed here used PBEsol exchange-correlation functional. [286] Then, HSE-06 was applied to the optimised structure to generate electronic-structure calculations. [217] Full details are available in this paper if required [287].

5.4 Results and discussion

5.4.1 Core level

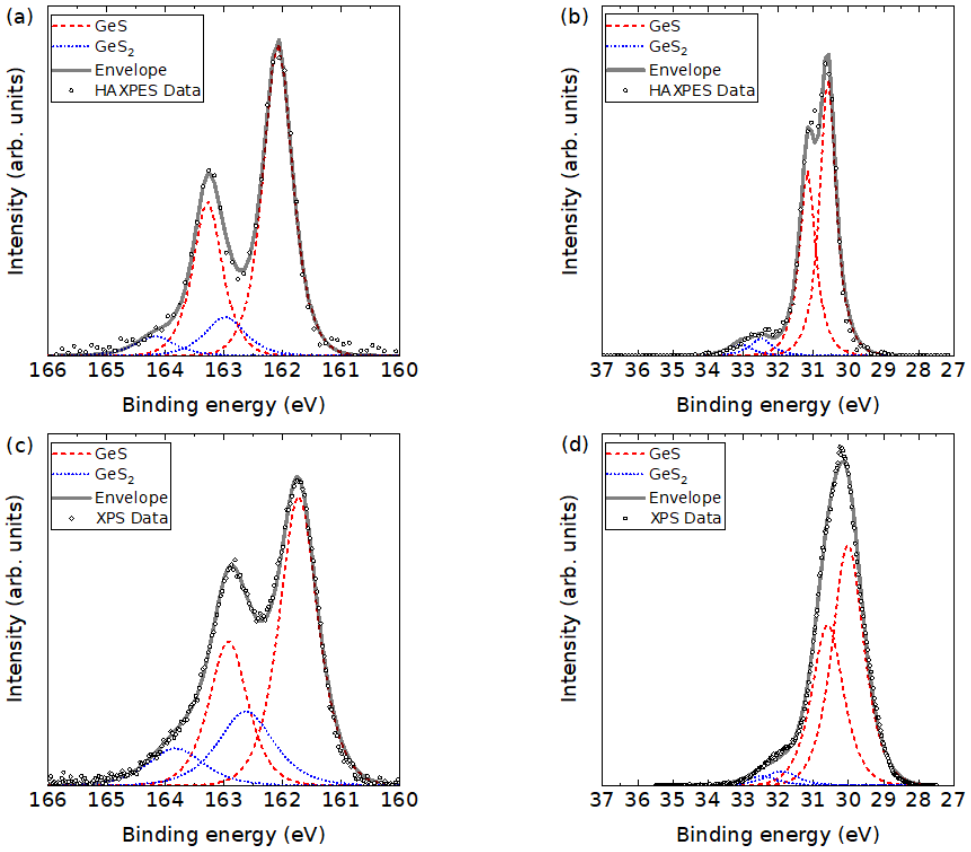

Figure 5.4: *Photoemission measurements on GeS crystals. (a)/(b) HAXPES measurements of the S 2p (a) and Ge 3d (b) core levels. (c)/(d) XPS measurements of the S 2p (c) and Ge 3d (d) core levels. A Shirley background has been subtracted from all four spectra. The peak positions and FWHM are summarised in Table 5.1.*

Figure 5.4(a) and 5.4(b) show HAXPES measurements on GeS in the S $2p$ and Ge $3d$ regions, respectively, while Figure 5.4(c) and 5.4(d) show equivalent XPS measurements. The positions and full widths at half maxima (FWHM) of the fitted peaks are presented in Table 5.1. Evidence confirming the absence of oxygen

Table 5.1: *Peak positions (FWHM) from the GeS measurements shown in Figure 5.4. The doublet separations for the S 2p and Ge 3d features are 1.2 eV and 0.58 eV respectively. The separation between components associated with the different chemical environments are supported by the fits of more heavily contaminated samples in the supplementary information of the published work. [287]*

Regions	HAXPES (eV)	XPS (eV)
S $2p_{3/2}$ - GeS	162.1 (0.6)	161.7 (0.8)
S $2p_{3/2}$ - GeS_2	163.0 (0.8)	162.6 (1.1)
Ge $3d_{5/2}$ - GeS	30.6 (0.5)	30.0 (1.0)
Ge $3d_{5/2}$ - GeS_2	32.5 (0.7)	31.9 (1.1)

Table 5.2: *Peak positions (FWHM) from the GeSe measurements shown in Figure 5.5. The doublet separations for the Se 3d and Ge 3d regions are 0.85 eV and 0.58 eV respectively. The separations between components associated with different chemical environments are supported by the fits of more heavily contaminated samples in the supplementary information of the published work. [287]*

Regions	HAXPES (eV)	XPS (eV)
Se $3d_{5/2}$ - GeSe	53.9 (0.5)	54.0 (0.6)
Se $3d_{5/2}$ - El. Se	54.5 (0.9)	54.6 (1.2)
Ge $3d_{5/2}$ - GeSe	29.9 (0.5)	29.9 (0.9)
Ge $3d_{5/2}$ - GeO	31.1 (0.9)	31.1 (1.0)
Ge $3d_{5/2}$ - GeO_2	32.7 (0.8)	32.7 (1.9)

contamination and measurements in the Ge $2p$ region are given in the supplementary information of the published work. [287] One previous study of GeS crystals reported the GeS S $2p_{3/2}$ peaks to be in the region of 161.8 eV, which is in reasonable agreement with our findings [288]. However, previous measurements of the core levels in GeS were unable to clearly resolve the $3d_{5/2}$ and $3d_{3/2}$ components of the Ge 3d doublet due to insufficient resolution. [288, 289]. This is also the case for our XPS measurements, but we were able to resolve the components using our higher-resolution HAXPES measurements.

HAXPES and XPS measurements of the Se $3d$ and Ge $3d$ core levels in GeSe are presented in Figure 5.5, and the positions and FWHM of the fitted peaks are presented in Table 5.2. Measurements of the Ge $2p$ region are presented in the supplementary information of the published work. [287] Previous studies of GeSe did not report the Se $3d$ doublet separation. [230, 288, 290] Previous reports that resolved the Ge $3d$ doublets place the Ge $3d_{5/2}$ feature at 29.85 eV, in agreement with our findings [167, 230]. However, these studies were performed using XPS and therefore lack the energy resolution of our HAXPES measurements.

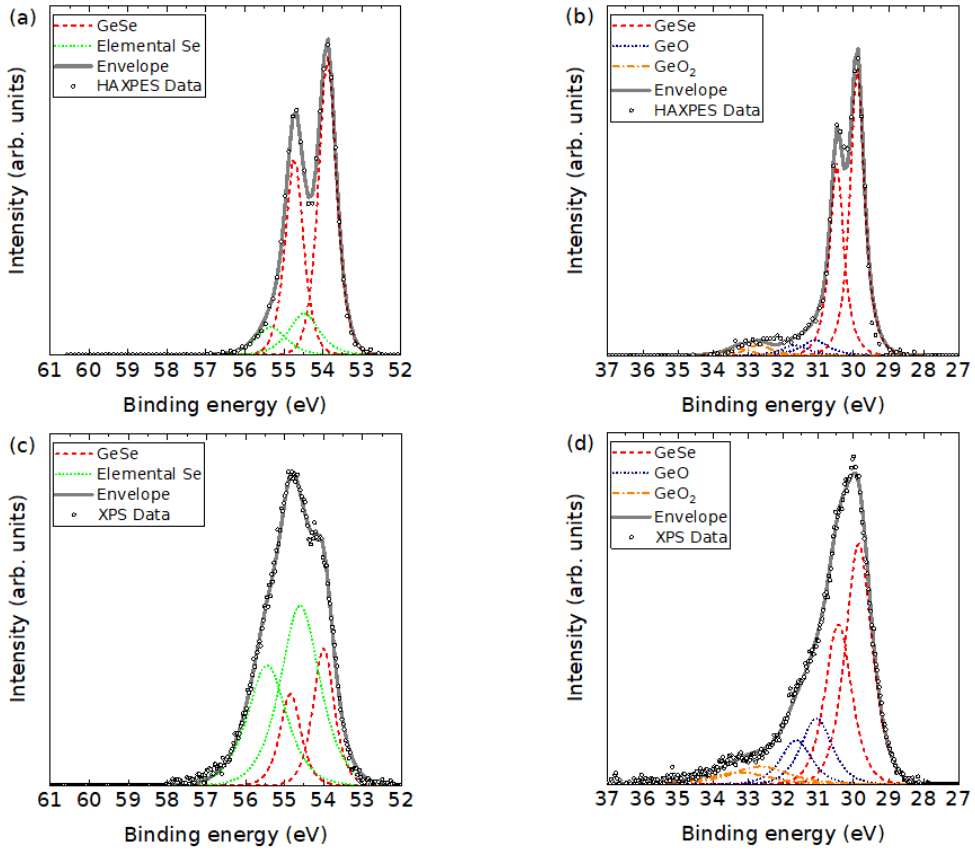

Figure 5.5: *Photoemission measurements of GeSe crystals. (a)/(b) HAXPES measurements of the Se 3d (a) and Ge 3d (b) core levels. (c)/(d) XPS measurements of the Se 3d (c) and Ge 3d (d) core levels. A Shirley background has been subtracted from all four spectra. The peak positions and FWHM are summarised in Table 5.2.*

For GeS, the results indicate a small amount of contamination with GeS_2. As the contamination is present in the photoemission results but not the XRD, this indicates the contamination is limited to the surface. This is not expected to influence the ionization potential (IP) results reported below, due to its low intensity and the significantly higher IP of GeS_2 compared with that of GeS. For GeSe, measurements of the Ge $3d$ region show GeO and GeO_2. The measurements of the Se $3d$ region also show some contamination with elemental Se. Only small amounts are detected in the HAXPES spectra, whereas in the XPS measurements the elemental Se component is larger than the GeSe component. The elemental Se component therefore likely corresponds to selenium ejected to the surface when the germanium was oxidised. That the contamination is limited to the surface is again confirmed by the fact that the species are only observed in the photoemission spectra and not in the XRD measurements.

5.4.2 Band alignments

Figures 5.6(a) and 5.6(b) show XPS measurements of the VBM and SEC for GeS and GeSe respectively. These results can be used to calculate the ionization potential (IP) using the equation:

$$\mathrm{IP} = h\nu - (\mathrm{SEC} - \mathrm{VBM}) \tag{5.1}$$

where $h\nu = 1.487$ keV is the energy of the incident x-rays. The IP values were found to be 5.74 eV for GeS and 5.48 eV for GeSe. Using these IP values and band gap measurements from the previous chapter, the positions of the valence and conduction bands of GeS and GeSe were determined and are shown in Figure 5.7. The GeSe IP value measured here is similar to, albeit slightly higher than, the 5.12 eV reported previously.[291]

A useful comparison to make is the natural band alignments with potential window layers when using GeS and GeSe in a solar cell (Figure 5.7). There are no studies, experimental or theoretical, of GeS solar cells. However, a number of window layers for GeSe have been proposed theoretically and tested experimentally. TiO_2 is widely used as a window layer in Sb_2Se_3 solar cells. [169] The natural band alignments of TiO_2 with both GeS and GeSe suggest a small spike-like barrier. However, the GeSe/TiO_2 devices reported to date have shown poor performance. [227, 297] On the other hand, CdS would exhibit a small cliff-like barrier, and GeSe/CdS devices have shown superior performance to date. [167, 230]. Given how small the CBOs are for both CdS and TiO_2, the natural band alignments suggest both could be suitable window layers for GeS and GeSe. Theoretical studies have suggested SnS and SnSe as potential partner layers for GeSe-based PV devices [283, 284]. For SnS, the natural band alignments with both GeS and GeSe indicate a

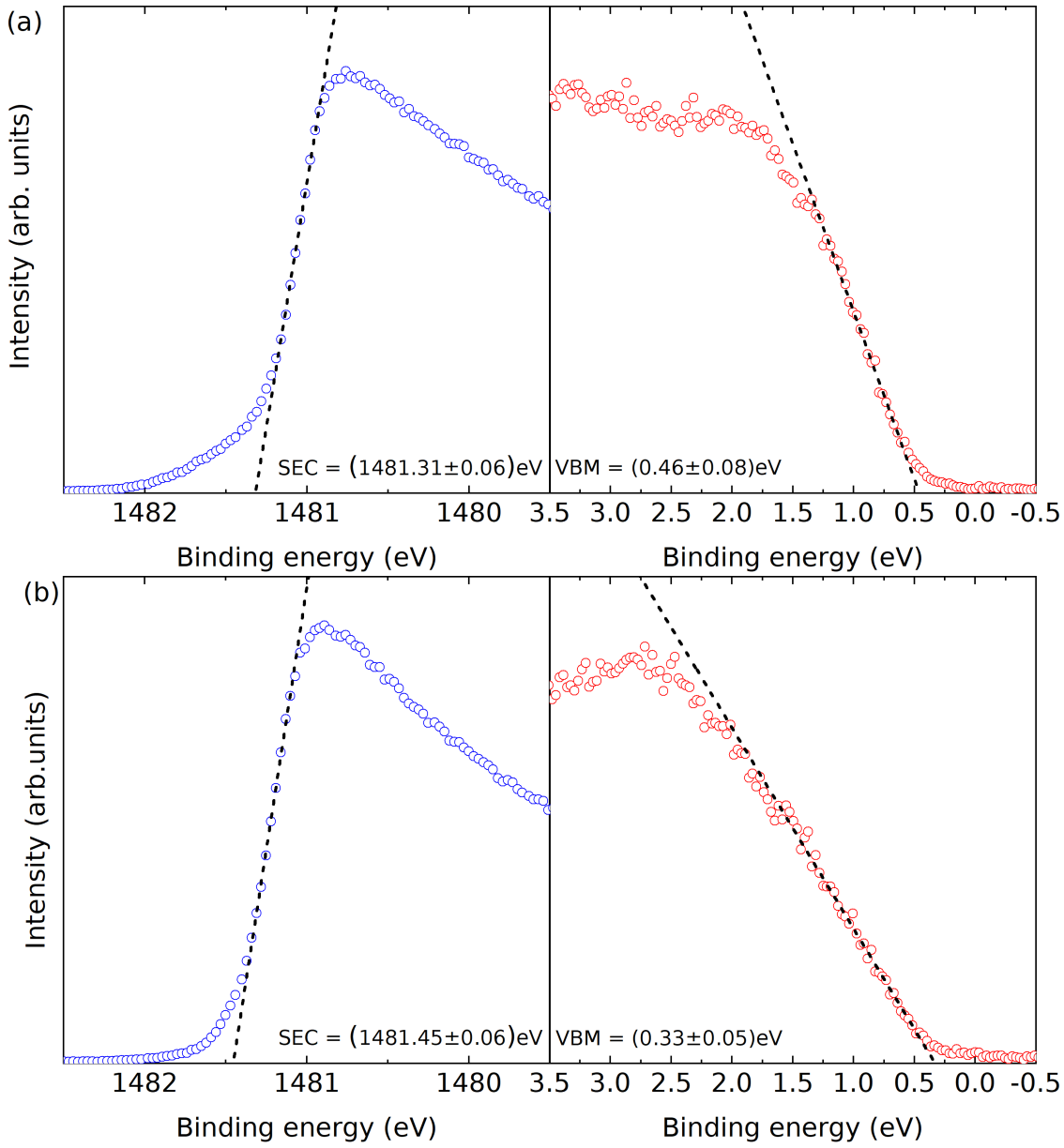

Figure 5.6: *Secondary electron cutoff (SEC) and valence band onset of GeS (a) and GeSe (b) measured using XPS ($h\nu$ = 1.487 keV). The linear extrapolations used to determine the secondary electron cutoff and valence band maxima are shown by dotted lines.*

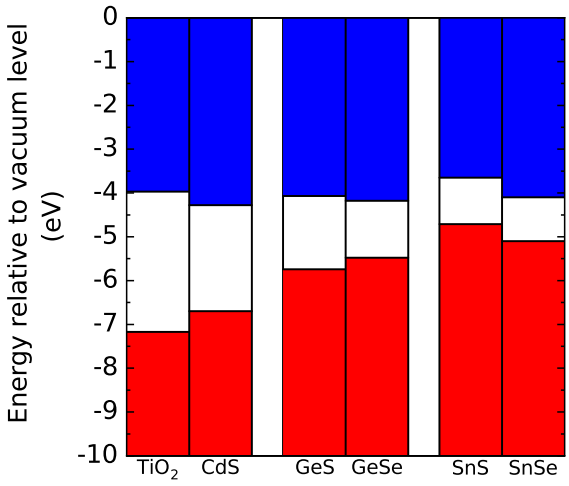

Figure 5.7: *Comparison of the natural band alignments of GeS and GeSe with some potential window layers for photovoltaic devices. The positions of the valence band maxima of GeS and GeSe were experimentally determined using the measurements in Figure 5.6, and the conduction band minima were then inferred from the band gaps reported in the previous chapter. The band alignments for the window layer materials are taken from the literature. [133, 292–294]*

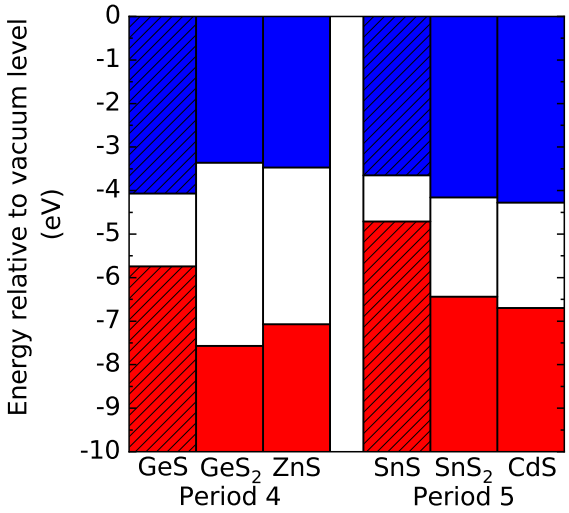

Figure 5.8: *Comparison of the positions of the valence band maximum (VBM) and conduction band minimum (CBM) of GeS to other Period 4/5 sulphides. The position of the VBM of GeS was determined from the measurements in Figure 5.6, and the position of the CBM was determined using the band gap reported in the previous chapter. The band positions of the other materials are taken from the literature. [292, 293, 295, 296] The shaded bars used for GeS and SnS indicate that these materials have stereochemically active lone pairs.*

large cliff-like barrier, which would limit the device efficiency. This could explain why Mao *et al.* observed superior performance in GeSe-based solar cells when partnering with SnSe rather than SnS, as SnSe has an almost flat conduction band alignment with GeSe. [284]

In Figure 5.8, the GeS band positions are compared to those of related sulfides to demonstrate the impact the Ge lone pair on the ionisation potentials. This is limited to sulfides because reliable literature data for other selenides appears to be lacking. By comparing to the other Period 4 cation materials, it is clear that the GeS lone pair significantly reduces the ionisation potential. GeS_2 has the same composition and hence valence orbitals, but with Ge in the 4+ rather than 2+ oxidation state. ZnS has an almost identical electronic configuration and 2+ oxidation state, but no stereochemically active lone pair. Figure 5.8 also compares the band positions of the corresponding Period 5 sulphides (i.e. GeS and SnS, GeS_2 and SnS_2, ZnS and CdS). This wider comparison again confirms that the presence of the stereochemically active lone pair leads to a marked reduction in the ionisation potential, for both Period 4 and 5 sulphides.

The effect of the lone pair on raising the VBM and reducing the ionisation potential can be understood using the revised lone pair model. [152] The Ge $4s$/Sn $5s$ states hybridise with the S $3p$ states to form bonding and antibonding states, with the latter being raised above the S $3p$ states that would otherwise have dominated the VBM and determined the ionisation potential. We have previously demonstrated this for the Sn chalcogenides, [292] and our results show the same effect for GeS. In GeS_2/ZnS and SnS_2/CdS, the antibonding states do not form, and so the ionisation potential is dominated by the S $3p$ states, which are at higher binding energy, and thus these materials have lower valence band maxima and higher ionisation potentials.

5.4.3 Valence bands

Figure 5.9 compares the valence band photoemission spectra measured using XPS and HAXPES to pDoS curves obtained from hybrid DFT. Figures 5.9(a) and 5.9(b) show the HAXPES and XPS results for GeS, respectively, while Figures 5.9(c) and 5.9(d) show the same data for GeSe. The calculated pDoS are weighted using the relevant one electron photoionisation cross sections (Figure 3.8) [180] and convolved with a Gaussian function to account for instrumental and thermal broadening, and a Lorentzian function to account for lifetime broadening. The FWHM of the Gaussian functions were 0.24 eV and 0.38 eV for the HAXPES and XPS simulations, respectively, while the FWHM of the Lorentzian functions were 0.24 eV and 0.30 eV.

For GeS, the HAXPES measurements in Figure 5.9(a) begin with a narrow peak

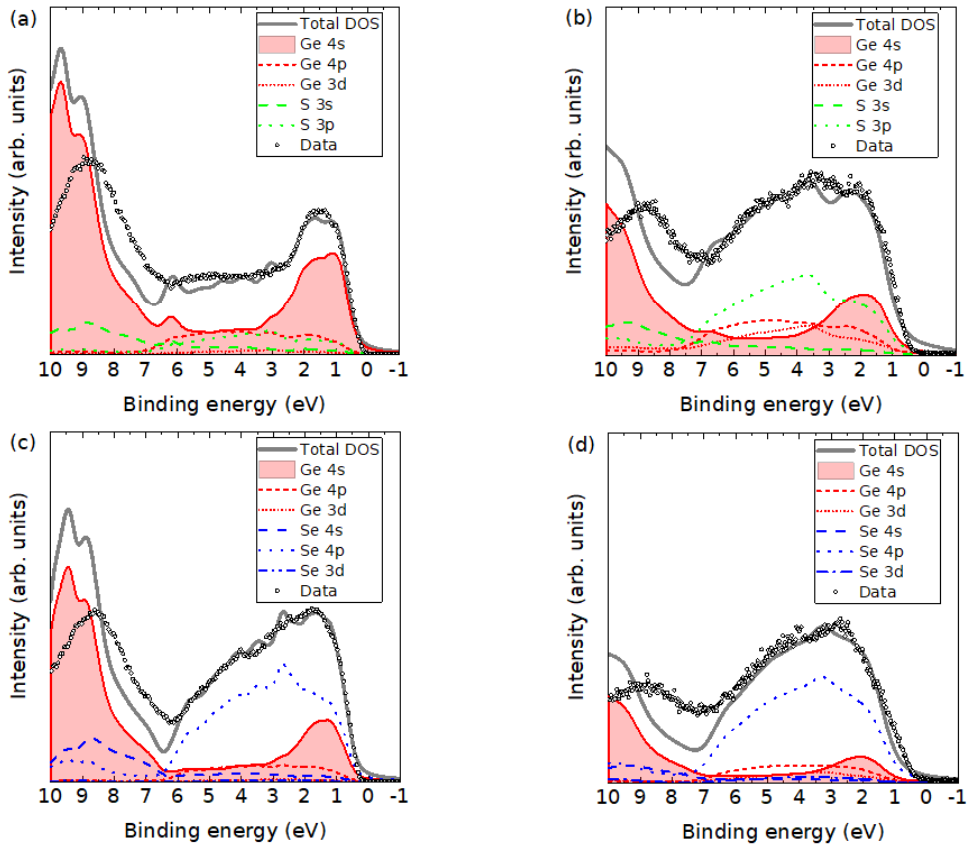

Figure 5.9: *Comparison of the experimental valence band spectra of GeS and GeSe to the atom- and orbital-projected electronic density of states (pDoS) curves obtained from hybrid DFT calculations. (a) and (b) compare the HAXPES and XPS measurements on GeS, respectively. (c) and (d) compare the same data for GeSe. All four plots compare the measurements to the DFT pDoS after weighting with the cross sections in Figure 3.8.*

at the VBM (0-2.5 eV), followed by a plateau to 6-7 eV and a broad peak centred around 9 eV. In the XPS measurements in Figure 5.9(b), there is instead one broad peak from the VBM (0-6 eV) followed by a second peak centred around 8.5 eV. The differences between the two spectra are explained well by the calculated cross-section corrected pDoS curves, with experiment and theory agreeing well up to around 7 eV. The broad peak in the XPS data is shown to be composed of contributions from S $3p$ and Ge $4s$, $4p$ and $3d$ orbitals, together with a small contribution from S $3s$ states. However, as expected from the one-electron photoionisation cross sections, the Ge $4s$ orbitals make a more significant contribution to the HAXPES spectra than the other orbitals, and the more pronounced peak therefore arises from the presence of the Ge $4s$ states at the VBM. This provides experimental evidence, for the first time, for the presence of Ge $4s$ states at the VBM in GeS, which is an important indicator of the cation having a stereochemically active lone pair. This also provides direct evidence to support our explanation of the comparatively low ionisation potential of GeS demonstrated in Figure 5.8.

Both the HAXPES and XPS measurements on GeSe in Figure 5.9(c) and 5.9(d), respectively, begin with one broad peak from the VBM (0-7 eV) followed by a second smaller peak centred around 9 eV. However, there are subtle differences in the shapes of the two broad peaks. The valence band has a sharper onset in the HAXPES than in the XPS spectra, and the top of the first broad peak is closer to the onset in the former. This subtle difference in shape is again explained by the calculated pDoS curves, and the experiments and theory again agree well up to 7 eV. The subtle differences are related to the hybridised lone pair states present at the VBM. The XPS peak shows a large contribution from Se $4p$ orbitals, with the height of the experimental valence band spectrum close to the maximum of the Se $4p$ pDoS. The broad peak also contains smaller contributions from the Ge $4s$, $4p$ and $3d$ and the Se $4s$ and $4p$ states. As expected from the differences in the cross sections, the Ge $4s^2$ orbitals make a larger contribution to the HAXPES than to the XPS spectra. This causes the sharper onset at the valence band, where the Ge $4s$ orbitals contribute to the density of states, and shifts the maximum of the broad peak closer to the onset. Once again, this provides the first experimental evidence for the presence of Ge $4s$ orbitals at the VBM in GeSe, and hence evidence for stereochemically active lone pairs.

A noteworthy feature of all four comparisons in Figure 5.9 is the divergence between experiment and theory at higher binding energies, which is a relatively common occurrence. [298, 299] A possible cause of this is that the cross-section corrected DFT valence band DOS are based on the ground-state electronic structure, whereas the experimental spectra probe the materials in an excited state. Ley *et al.* state that this will shift experimental features toward the top of the valence

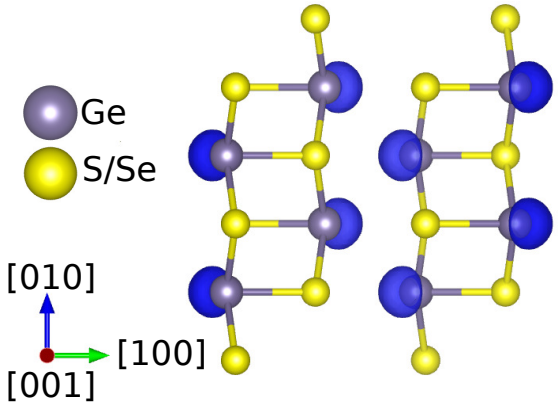

Figure 5.10: *Electron localisation function for GeS obtained using hybrid DFT (isosurface level: 0.918), showing the Ge 4s lone pair in blue. Similar results are obtained for GeSe - see supplementary information of the publication. [287] This image was prepared using the VESTA software. [157]*

band relative to spectra predicted from theory, which is consistent with how our measurements and calculations compare. [300]

The key finding from the present analysis is the presence of Ge $4s$ orbitals at the valence band edge in both GeS and GeSe. The revised lone pair model indicates that in order for these stereochemically active lone pairs to form the Ge $4s$ orbitals must interact with the anion S $3p$/Se $4p$ orbitals to form bonding and antibonding states. The presence of the Ge $4s$ states at the valence band edges is, therefore, evidence that the antibonding states predicted by the revised lone pair model are present, and hence that these materials have the stereochemically active lone pairs found in several other high-performance PV materials. The formation of these bonding and antibonding states is only possible in a distorted crystal structure, because the orbital interactions would otherwise be forbidden by symmetry. The asymmetric electron densities associated with the distorted orthorhombic crystal structures thus arise from the stabilisation of the Ge $4s^2$ lone pairs.

The Ge lone pairs in GeS and GeSe can be visualised using the electron localisation function (ELF) [301] isosurfaces (Figure 5.10). The lone pairs are seen to project between the nanosheets in the [100] direction, which is typical of stereochemically active lone pairs and the associated crystal structure distortions. The ELF shown in Figure 5.10 was generated from the calculations where the Ge $3d$ electrons were treated as core states. Despite the very similar electronic structures, we found that including these states in the valence region led to a notably more spherical charge density around the Ge atoms and substantial delocalization of the Ge lone pair. Despite this, as noted above we found no significant differences in the pDoS, including in the contributions of the Ge $4s$ states to the VBM, and we also found no significant differences in the atomic charges and volumes obtained from topological analyses of the charge densities. [302] We are therefore unsure of

whether this discrepancy is simply an artefact in the calculations.

When comparing the pDoS of GeS and GeSe, it is clear that the Ge $4s$ orbitals make a larger contribution to the valence band edge in GeS than in GeSe. As shown in Figure 5.11(a), the S $3p$ has a lower configuration energy than the Se 4p, which means the separation between the Ge $4s$ states and the anion p states is smaller in GeS than in GeSe. [303] This means that when the Ge $4s$ and the anion p states interact to form bonding and antibonding states, the Ge $4s$ make a larger contribution to the antibonding states that form the valence band edge in GeS than in GeSe. This analysis was first performed by Watson *et al.* for Pb $6s$ lone pairs. [304] Waghmare *et al.* subsequently used DFT calculations to evidence this phenomenon for other cubic IV-VI chalcogenides, including GeS and GeSe, but the cubic compounds do not allow for lattice distortion. [257] The phenomenon was later generalised by Walsh *et al.* with the revised lone pair model. [152] The pattern of the Ge lone pair making a larger contribution to the antibonding states as the size of the anion decreases is consistent with previous studies on Sn and Sb lone pairs. [305, 306]

A further finding from this work is therefore that the Ge^{2+} cation can form stereochemically active lone pairs. This finding should offer new avenues in fields beyond the Ge chalcogenides. For example, research into Ge perovskites may also benefit from confirmation that the lone pair formation is possible, despite the additional challenges posed by oxidation. [149, 266, 267, 269, 275, 307] The traditional lone pair model has generally disregarded $4s^2$ lone pairs as it was assumed that d-block (or scandide) contractions would dominate in this row of the periodic table. [308] Similarly, the revised lone pair model predicts that the formation of stereochemically active lone pairs in GeS and GeSe is unlikely due to the difference in energy between the Ge $4s$ and S $3p$/Se $4p$ atomic levels.

As can be seen in Figure 5.11(b), the difference between the Ge $4s$ and S $3p$ states is greater than the difference between the Pb $6s$ and S $3p$ states. PbS is known to have an inactive lone pair, and the revised lone pair model explains this by the separation between anion p and cation s states being too large to form the asymmetric electron density required to drive the structural distortion. Using the same logic, the formation of the distorted GeS structure then seems highly unlikely as the difference between the states is larger still. As it is clear from the present studies that a stereochemically active lone pair does form, we propose a potential addendum to the model: since Ge is smaller than Pb, one might explain the different behaviour by taking into account the bond length between the cation and anion, as Orgel has suggested previously. [150, 151]

We attempted to investigate the influence of the Ge-chalcogen bond length on the lone pair activity in GeS and GeSe by performing further electronic-structure

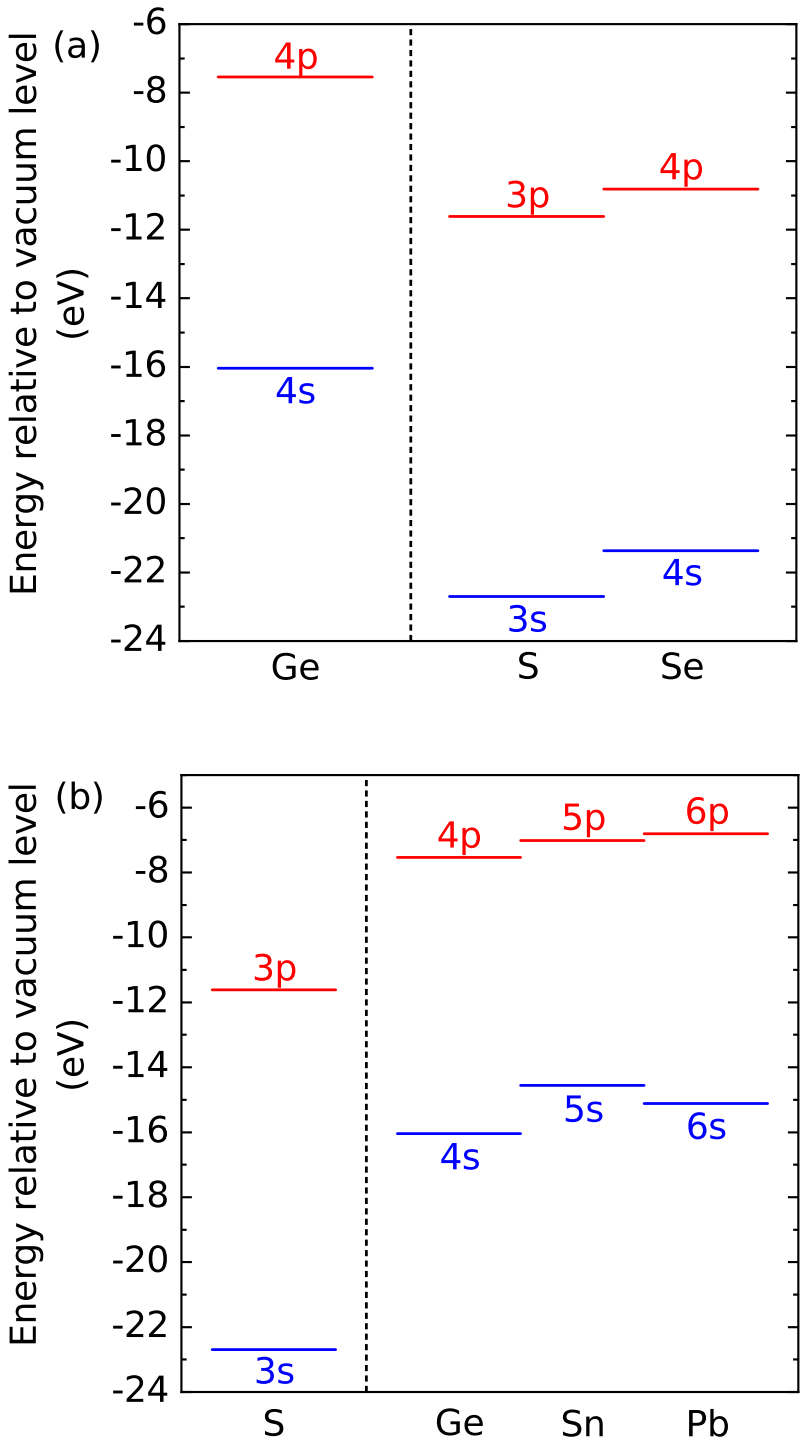

Figure 5.11: *Experimentally determined electronic configuration energies of the valence s and p orbitals in Ge, Sn, Pb, S and Se atoms using data from Refs 303 and 309. (a) Comparison of the energies of Ge with those of S and Se. (b) Comparison the energies of S with those of Ge, Sn and Pb. In the revised lone pair model, the energy separation between the cation s and anion p levels is a key descriptor of the strength of the interactions that drive the formation of active lone pairs and the resulting structural distortions.*

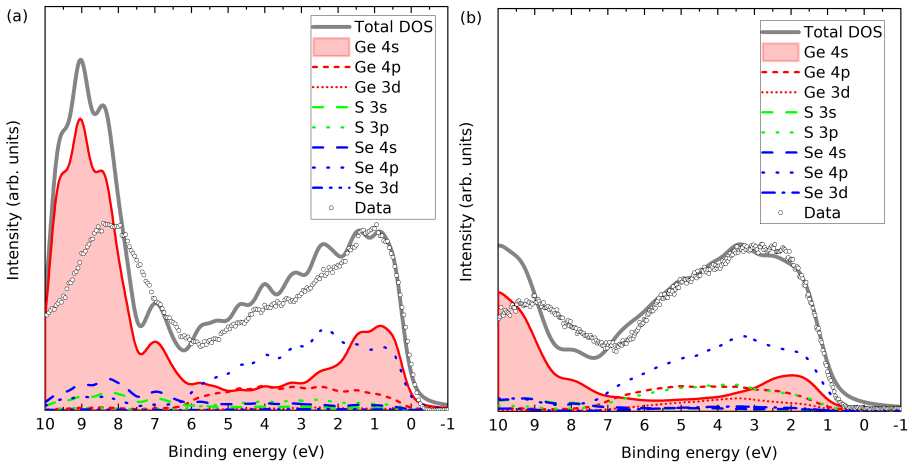

Figure 5.12: *Comparison of the calculated and broadened density of states of $GeS_{0.5}Se_{0.5}$ with the valence band spectra of the $GeS_{0.484}Se_{0.516}$ measured by (a) hard x-ray photoemission spectroscopy at 5.921 keV and (b) lab-based x-ray photoemission spectroscopy at 1.487 keV.*

calculations with the unit-cell volume of both systems adjusted to ± 10 % of the equilibrium volume V_{eq} in the supplementary information of the published work. [287] We found that the cell axis corresponding to the strongest bonding is resistant to change under compression and expansion, such that there is little variation in the nearest-neighbour Ge-chalcogen distance. Despite this, there is a large variation in the direct and indirect bandgaps. We observe some variation in the Ge *s* PDoS in the vicinity of the VBM in both systems, although the integral is largely preserved within a window of ∼2.5 eV below the Fermi energy. Most importantly, analysis of the ELFs at compressed and expanded volumes show that the Ge lone pair is retained at all the volumes tested. We therefore conclude that fully testing our hypothesis on the importance of the cation-anion distance would require a systematic analysis of different chemical systems (i.e. different structural phases and/or chemical species), which is considered to be beyond the scope of the present study.

GeS_xSe_{1-x} comparison

As a small aside, $GeS_{0.5}Se_{0.5}$ valence band density of states is compared to $GeS_{0.484}Se_{0.516}$ using HAXPES and XPS. Both show broadly good agreement between experiment and theory in the range of 0-6 eV. There is a noticeable difference in the shape of the two spectra, with the HAXPES showing a sharp peak at 0-2.5 eV followed by a steady decrease to 6 eV, and the XPS showing one large broad peak between 0-6 eV. The change in shape of the valence band spectrum for the two different photoemission energies is caused by the increased intensity of the Ge 4*s* orbital contribution at the valence band edge. This is evidence that the ternary GeS_xSe_{1-x} alloys have the lone pair effect based on the revised lone pair model. [152] This good agree-

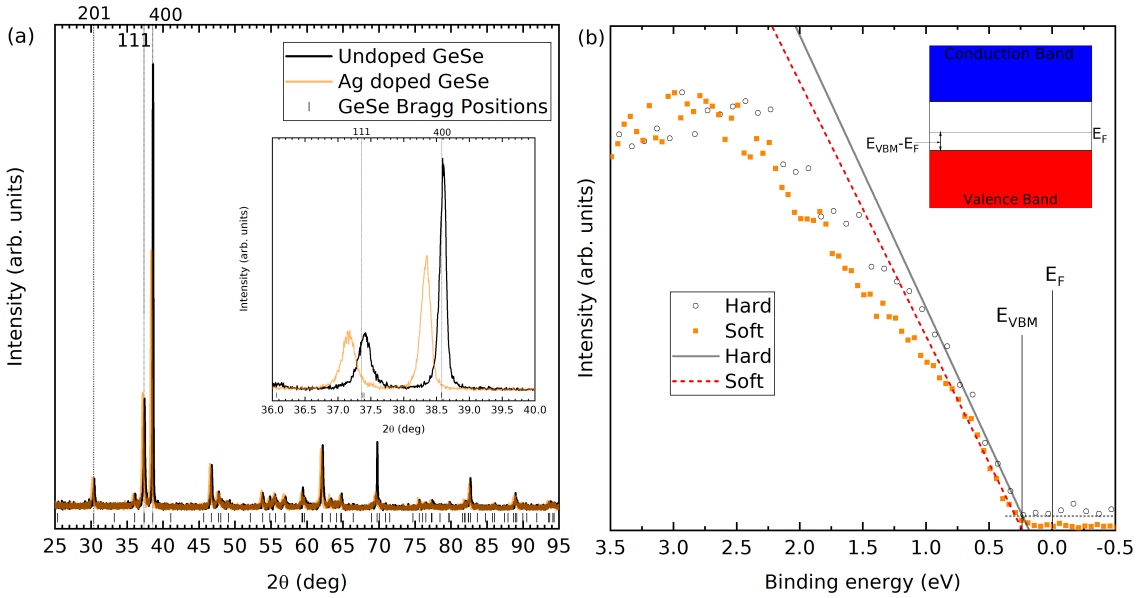

Figure 5.13: *(a) Powder XRD for undoped and Ag-doped materials. Bragg peaks for 201, 111, and 400 reflections are shown with dotted lines. Inset shows the same data zoomed into the 111 and 400 peaks to highlight the shift in pattern. (b) The valence band measurements for the Ag-doped GeSe for hard and soft x-ray photoemission. Inset is a diagram explaining how the Fermi level position can be calculated using the signal onset.*

ment between theory and experiment is consistent with the above work that showed similar levels of agreement for the endpoints, but in this case additionally shows that the supercell alloy model captures the electronic structure of the solid solution reasonably well.

5.4.4 Doping GeSe

Given the results of the previous Chapter, which shows GeSe to be the end of the series closest to the ideal optical properties for the detailed balance limit, as well as the above result that the endpoints of the series have stereochemically active lone pairs, GeSe is investigated below as a PV material. As well as testing as-grown GeSe, GeSe was also doped with Ag to change the doping density of the material with the aim of improving performance.

Powder XRD was performed on the undoped and Ag-doped materials, shown in Figure 5.13(a). The Bragg peak positions are taken from the single crystal X-ray diffraction data of GeSe from the previous Chapter. The Ag-doped GeSe powder shows no additional peaks to the undoped GeSe, suggesting no secondary phases have occurred. Table 5.3 shows the lattice parameters measured for both samples, calculated using the data in Figure 5.13(a) as described for the previous Chapter. The lattice parameters for the undoped material agree with the single crystal X-ray

diffraction data. For the Ag-doped material, all three lattice parameters increase, consistent with the larger size of silver atoms compared with germanium atoms and implying substitutional incorporation as Ag_{Ge}.

Table 5.3: *Lattice parameters (in the Pnma space group setting) for the undoped and Ag-doped GeSe obtained from XRD.*

Lattice parameter	Undoped (Å)	Ag-doped (Å)
a	10.828(9)	10.866(9)
b	3.834(5)	3.844(5)
c	4.382(6)	4.433(6)

ICP-OES was used to estimate the concentration of Ag atoms within the GeSe. Within the undoped GeSe there are approximately 2.2×10^{22} atoms cm^{-3}. The density of silver atoms present for the Ag-doped GeSe is approximately 1.6×10^{18} atoms cm^{-3}, which matches the target of 0.01 molar% Ag levels. No traces of Ag were found in the undoped GeSe.

Hard and soft x-ray photoemission spectroscopy was used to determine the Fermi level position of the undoped and Ag-doped GeSe. In calibrated photoemission spectroscopy, 0 eV binding energy corresponds to the Fermi level of the material. Therefore, measuring the valence band onset determines the separation between the valence band maximum and the Fermi level. In this scenario, a smaller difference would indicate a more p-type material. Soft x-ray photoemission spectroscopy is more surface sensitive than hard x-ray photoemission. The results from the undoped GeSe are taken from Figure 5.9(c) and 5.9(d), and the Ag-doped valence band onsets are shown in Figure 5.13(b). All values are shown in Table 5.4.

Table 5.4: *The measured valence band maximum for the doped and undoped materials. The undoped GeSe valence band maximum were obtained from Figure 5.9(c) and 5.9(d) and Ag-doped GeSe valence band maximum were obtained from Figure 5.13(b).*

Photoemission type	Undoped VBM - E_F (eV)	Ag-doped VBM - E_F (eV)
Hard	0.30±0.05	0.23±0.05
Soft	0.33±0.05	0.26±0.05

Given GeSe has a band gap of 1.30 eV, any valence band maximum less than 0.65 eV from the Fermi level suggests a *p*-type material. The undoped GeSe is *p*-type according to both the soft and hard x-ray photoemission spectroscopy, which is consistent with the previous work that suggests the material is natively *p*-type. [276, 277] Furthermore, the results in both the soft and hard x-ray photoemission spectroscopy indicate that the Ag-doped GeSe has a higher hole density than the

undoped GeSe. The VBM to Fermi level separations have been plotted on Figure 5.14(a) for the two photon energies for the Ag-doped and undoped GeSe - the depths at which they are plotted corresponds to three times the inelastic mean free path (IMFP) for the valence band photoelectrons for each photon energy. IMFP values were calculated using the TPP-2M method.[179] Three times the IMFP corresponds to the depth from which 95% of the measured photoelectrons escape the material, according to the Beer-Lambert law. This data has been used to estimate the surface band bending and charge profiles by solving Poisson's equation.[310] The hole effective masses (electron and hole electron masses of 0.5 and 0.6, respectively) and the dielectric constants (ϵ_∞ and ϵ_0 of 18.1 and 25.8, respectively) used to solve the Poisson equation were taken from the literature and isotropically averaged by taking the cubed root of their product.[311, 312] The results are shown in Figure 5.14. The bulk acceptor densities used as the bulk boundary condition for the Poisson solution are those determined from capacitance-voltage measurements on solar cell devices - see below. The GeSe layers in the devices are made from the same GeSe source material as the crystals used for the photoemission measurements, so the doping level is expected to be similar. The resulting hole densities are 1.9×10^{16} cm^{-3} for the Ag-doped GeSe and 5.2×10^{15} cm^{-3} for the undoped GeSe. Downward band bending occurs at the surface, corresponding to a hole depletion layer. This is consistent with positively charged donor-type surface states with their charge being balanced by the negatively-charged background acceptors in the depletion region. The higher hole density for the Ag-doped material more effectively screens the surface states and hence leads to a narrower depletion region - the bulk carrier density is reached by ∼200 nm compared with ∼400 nm for the undoped GeSe (see Figure 5.14).

5.4.5 Thin films

Thin films of both Ag-doped and undoped GeSe were deposited on both CdS and a 10 nm Sb_2Se_3 interfacial layer on CdS. The films were then annealed at temperatures determined by the optimised solar cell device results presented below. For both the Ag-doped and undoped films with no interfacial layer, the annealing condition was 400 °C for 10 minutes, whereas for the Ag-doped and undoped films with the Sb_2Se_3 interfacial layer the annealing condition was 375 °C for 20 minutes.

SEM images of all four structures after annealing are shown in Figure 5.15. The undoped films (Figures 5.15(b) and 5.15(d)) have lenticular grains at the GeSe surface 0.5-1 μm wide and 2-4 μm long. However, the silver doped films show different morphologies, with the film being grown with no interfacial layer (Figure 5.15(a)) showing striking nodular features 0.5 μm in size and having bright contrast, and that on the Sb_2Se_3 interfacial layer (Figure 5.15(c)) having a less-distinct grain structure.

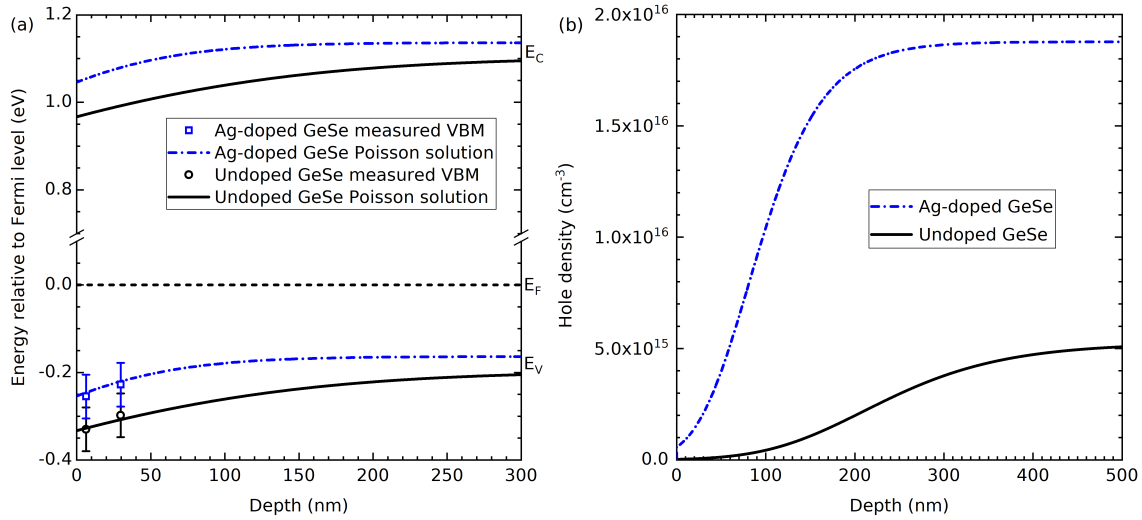

Figure 5.14: *(a) The VBM positions relative to the Fermi level, E_F, determined by photoemission spectroscopy for Ag-doped and undoped GeSe (points) and the band bending profiles obtained by solving the Poisson equation (lines); (b) the hole density versus depth corresponding to the band bending profiles shown in (a).*

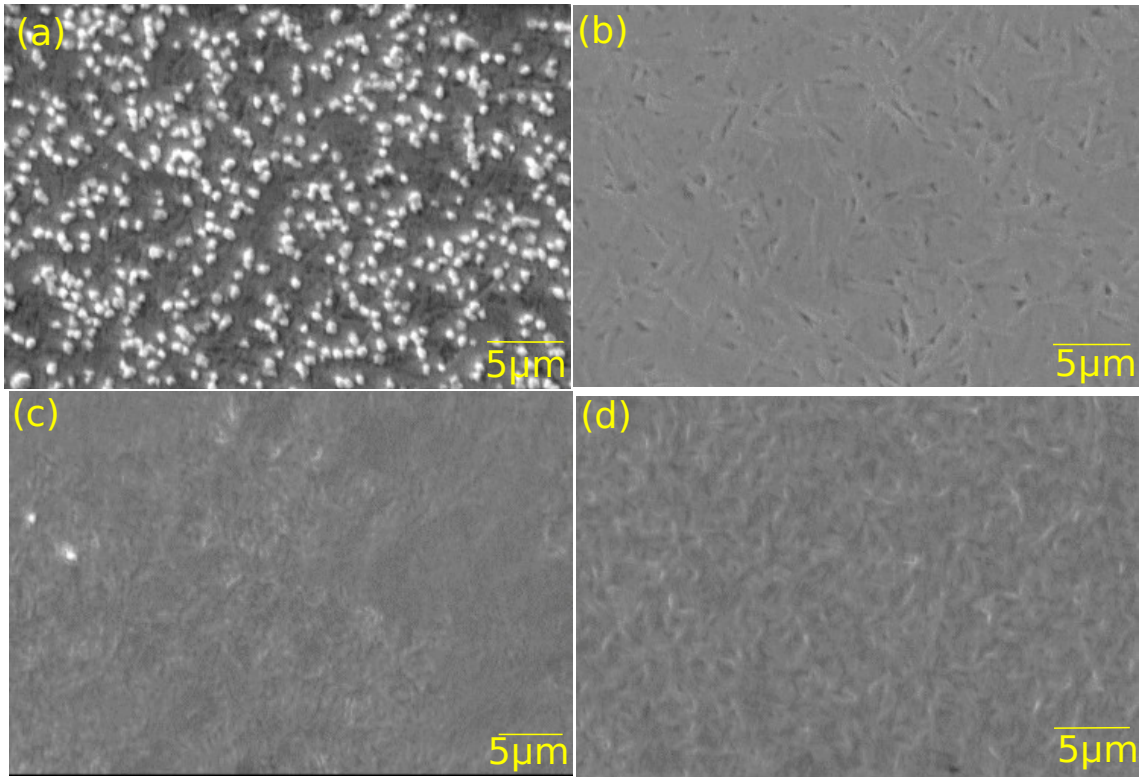

Figure 5.15: *Scanning electron microscopy images for devices (a) FTO/CdS/Ag:GeSe, (b) FTO/CdS/u:GeSe, (c) FTO/CdS/Sb_2Se_3/Ag:GeSe, and (d) FTO/CdS/Sb_2Se_3/u:GeSe where Ag is for silver doped samples and u is undoped samples.*

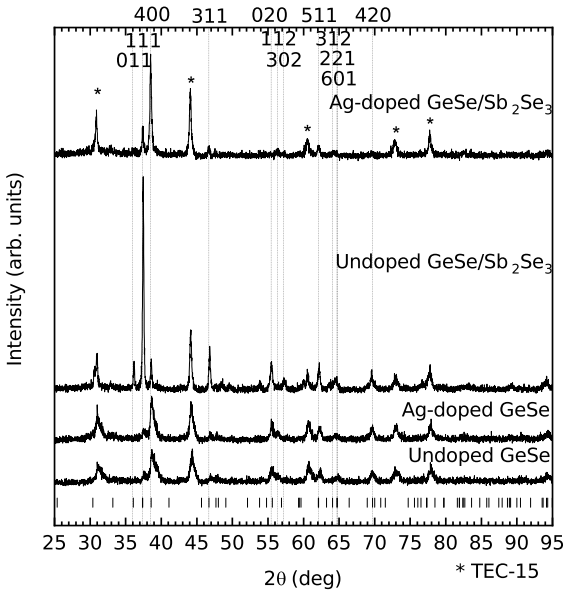

Figure 5.16: *Thin film XRD of the four film stacks along with the GeSe Bragg peak positions taken from the GeSe single crystal XRD data reported in the previous chapter. Relevant Bragg peak positions are labelled and positions related to the SnO_2:F coated substrate are starred.*

We considered the origin of the bright contrast in Figure 5.15(a): the 'secondary electron' detector used to record the images collects a majority of secondary electrons but also a minor fraction of primary electrons, which give compositionally sensitive contrast. Since the average atomic number of GeSe (31) is considerably lower than that of AgSe (40.5), it would be expected that AgSe would give bright contrast. However, this seems unlikely since the nominal composition of the films is just 0.01 atomic% Ag. The alternative explanation is that there is enhanced secondary electron emission from the nodules for morphological reasons. The nature of the nodules should therefore be examined in more detail with energy dispersive x-ray analysis and higher resolution imaging in the SEM.

Thin film XRD has been performed on all four films and is shown in Figure 5.16. The peak for every film is consistent with either GeSe or the SnO_2:F coated substrate (see * on Figure 5.16). The major difference that the incorporation of the Sb_2Se_3 interfacial layer appears to have on the structure of the undoped GeSe is the introduction of the Bragg peaks related to the 011, 111, and 311 reflections. The ratio of intensities of the 111 reflection to the 400 reflection suggests that the (111) plane is becoming more prominent relative to the (100) plane that the 400 reflection involves. Previous literature studying the structure of thin film GeSe has shown a strong orientation preference for the (100) plane experimentally and a theoretical study shows that the total energy of the plane is lower than alternative common planes. [227–232] The incorporation of Sb_2Se_3 interfacial layer has been shown previously to make the (111) plane more prominent, consistent with the findings in

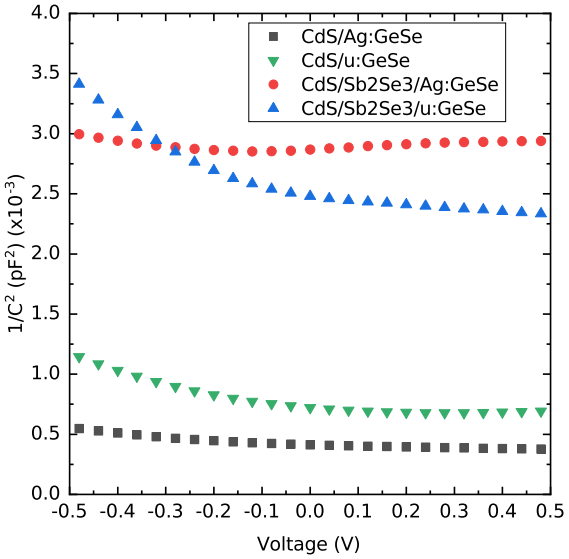

Figure 5.17: *Capacitance voltage measurements for all four champion contacts.*

this study. [167]

5.4.6 GeSe device results

All four device structures were processed into solar cells and the annealing temperatures optimised. To optimise, anneals were done at 25°C intervals between 325°C and 400°C for 20, 40 and 60 minutes. This range was chosen based on preliminary studies that shows 300°C or lower gives an amorphous film, whereas above 400°C the GeSe film appears to get damaged. CV measurements were performed on all four devices to determine doping densities and are presented in Figure 5.17. For the Ag-doped GeSe with an Sb_2Se_3 interfacial layer, a doping density value could not be accurately determined due to a nonlinear line shape near to 0 V - an indication that the device has an interfacial barrier at the junction, which would explain its poor device performance. Therefore, to get a reliable comparison of the hole density with and without the Ag dopant, only the devices with no Sb_2Se_3 interfacial layer were used. The Ag-doped GeSe sample has an acceptor density of 1.9×10^{16} cm^{-3} compared to the undoped GeSe sample with an acceptor density of 5.2×10^{15} cm^{-3}. The undoped GeSe with an Sb_2Se_3 interfacial layer showed a similar acceptor density of 4.6×10^{15} cm^{-3}, comparable to the undoped GeSe cell with no interfacial layer. This suggests that the incorporation of the Ag into the films is increasing the acceptor density by a factor of ~3.5. Therefore, assuming no other effects, Ag-doping should ultimately be beneficial for PV performance. The CV-determined acceptor density is approximately two orders of magnitude lower than the silver atomic density estimated from ICP-OES for the Ag-doped GeSe source material.

Figure 5.18 shows the JV curves for the best contact for each of the optimised

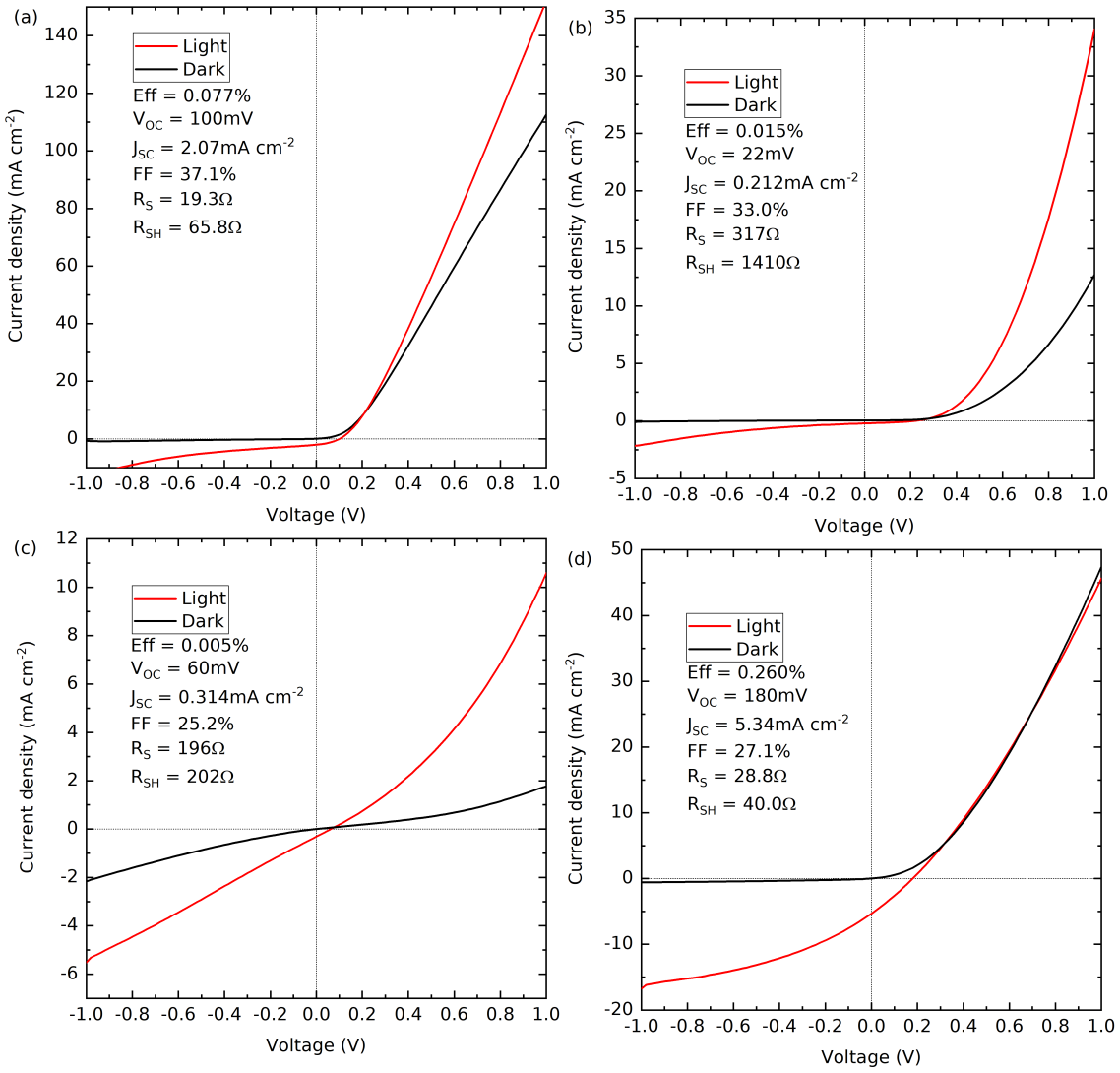

Figure 5.18: *Current density vs voltage measurements in light and dark for devices (a) FTO/CdS/Ag:GeSe/Au, (b) FTO/CdS/u:GeSe/Au, (c) FTO/CdS/Sb_2Se_3/Ag:GeSe/Au, and (d) FTO/CdS/Sb_2Se_3/u:GeSe/Au where Ag is for silver doped samples and u is undoped samples.*

Device	Efficiency (%)	V_{OC} mV	J_{SC} mA cm^{-2}	FF %
FTO/CdS/Ag:GeSe/Au	0.06±0.02	90±20	1.9±0.2	32±5
FTO/CdS/u:GeSe/Au	0.007±0.005	120±60	0.4±0.3	27±4
FTO/CdS/Sb_2Se_3/Ag:GeSe/Au	0.003±0.001	50±10	0.25±0.04	24±2
FTO/CdS/Sb_2Se_3/u:GeSe/Au	0.116±0.06	170±20	3.5±1.2	26.8±1.4

Table 5.5: *Average solar cell performance for the four different device structure when optimised. Errors presented are the standard deviation of all working contacts device performance.*

devices with the associated solar cell performance. Table 5.5 shows the average device parameters of all working contacts for the devices.

Figure 5.18(a) and 5.18(b) show the JV curves for the devices with no interfacial layer that have either Ag-doped or undoped GeSe, respectively. Both cells show a good diode shape in the dark but overall cell performance is compromised by low current. Furthermore, both have low V_{OC} and limited fill factors due to high series and low shunt resistance. EQE measurements were performed on both samples (see Figure 5.19) to diagnose the cause of the low currents. No signal could be measured for the Ag-doped GeSe, but for the undoped GeSe the EQE shows a peak near to the CdS band gap energy (around 525 nm). This suggests a very narrow collection region, with potential causes being low carrier lifetime, a narrow depletion region, or a thin material and thus low optical absorption. Given the acceptor densities reported here and the optical properties of GeSe, the second and third are unlikely.

Figure 5.18(c) and 5.18(d) show the devices with an Sb_2Se_3 interfacial layer that have either Ag-doped or undoped GeSe, respectively. The Ag-doped device with the Sb_2Se_3 interfacial layer is an extreme S-shape in the dark JV compared with the other devices, suggesting a fundamental issue with the device. The origin of this is uncertain, but it could be due to interdiffusion of the films or the formation of an unwanted electrical barrier.

Figure 5.18(d) shows the undoped device with the Sb_2Se_3 interfacial layer. The diode shape is broadly similar in light and in the dark, but significantly higher current and voltage are produced under illumination, producing a power conversion efficiency of 0.260 %. This may be due to an improvement in the built-in field of the interface, but the fill factor is again low due to high series and low shunt resistance. There is no S-shape feature in forward bias, suggesting the issues do not stem from an interfacial barrier and performance may instead be limited by the absorber material itself. EQE results support this conclusion, again showing a peak near to the CdS band gap energy. As discussed above, this is likely linked to low carrier lifetime.

The inclusion of the Sb_2Se_3 interfacial layer improves device performance for the

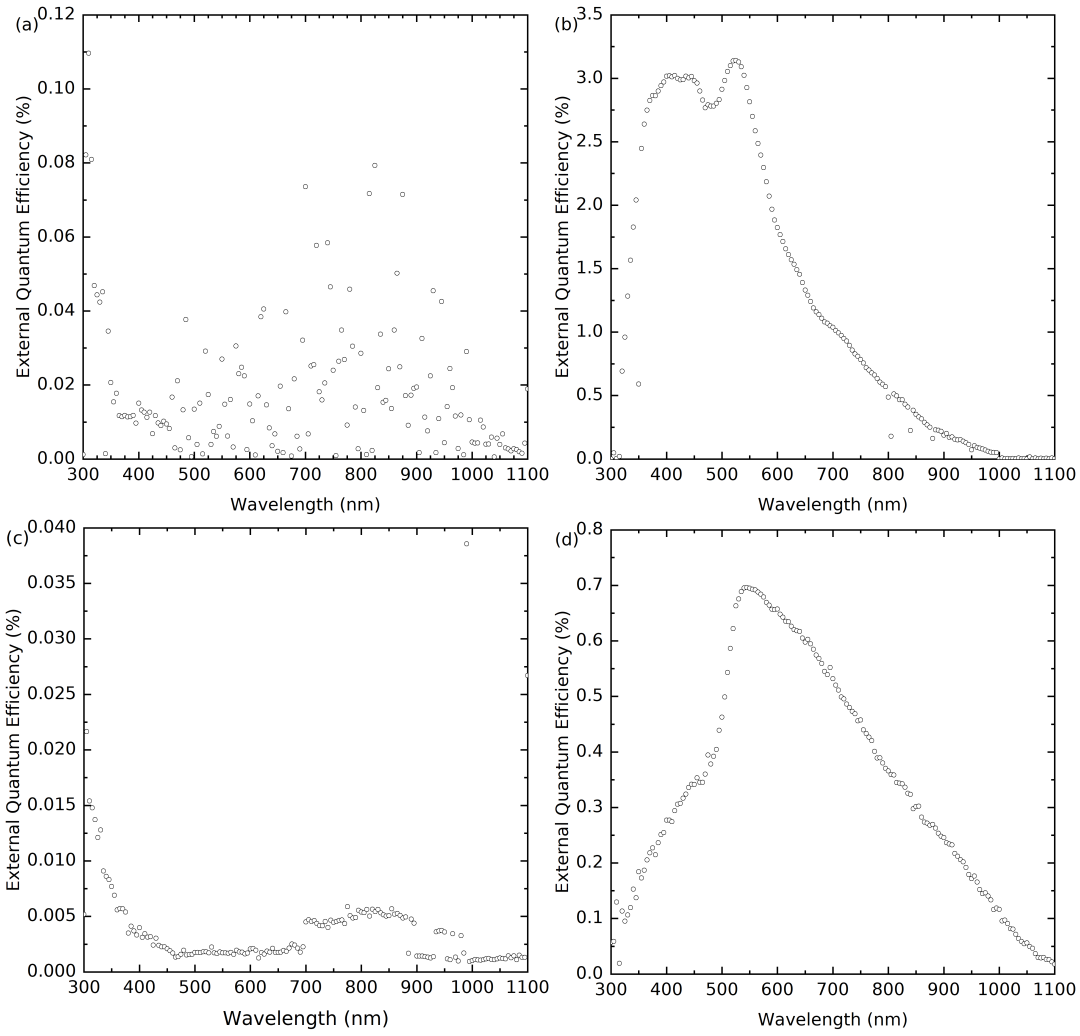

Figure 5.19: *External quantum efficiency measurements for devices (a) FTO/CdS/Ag:GeSe/Au, (b) FTO/CdS/u:GeSe/Au, (c) FTO/CdS/Sb_2Se_3/Ag:GeSe/Au, and (d) CdS/Sb_2Se_3/u:GeSe/Au where Ag is for silver doped samples and u is undoped samples.*

undoped GeSe, rising from 0.015% efficiency to 0.260 % efficiency. This is consistent with the previous record efficiency device result by Liu *et al.* for GeSe, which had a rise from 1.4% to 5.2% with the inclusion of the Sb_2Se_3 interfacial layer.[167] What is also consistent with their findings is that the inclusion of Sb_2Se_3 interfacial layer gives greater prominence to the (111) orientation relative to the (100) orientation in the XRD. Furthermore, the solar cells presented by Chen *et al.* that achieved maximum efficiencies of 0.27 % are strongly (100) orientated with no indication of (111) orientation. Xue *et al.* achieved 1.48 % efficiency with prominent (111) as well as (100) orientation. In combination, the literature appears to indicate having (111) orientation present is beneficial for improved device performance.

Conduction in the nanoribbon structure Sb_2Se_3 is known to be anisotropic, with the highest conductivity being along the covelently bonded ribbons. [162, 164] Similarly, since GeSe is a 2D material, it might be expected that if the sheets were perpendicular to the substrate in a PV device there would be some benefit to performance. However, in the (100) orientation the sheets are parallel to the substrate, which the Sb_2Se_3 literature would suggest is the least preferred to improve conductivity. This could explain why the cell performance, particularly the current, improves with the incorporation of the (111) orientation due to the improved conductivity along the sheets.

5.5 Conclusion

In conclusion, x-ray photoemission spectroscopy has been used to measure the secondary electron cutoffs and valence band offsets to determine ionisation potentials of 5.74 eV and 5.48 eV for germanium sulfide and germanium selenide, respectively. This gave the positions of the valence band maxima relative to vacuum level, and the conduction band minima were then deduced using the band gaps from the previous Chapter. The band alignments were compared to potential window layers for photovoltaic devices, and this comparison suggests CdS and TiO_2 as potential partner materials. Our measurements also clearly show that the ionisation potential of GeS is lower than in comparable materials, which we ascribe to the presence of stereochemically active lone pairs and the associated antibonding states at the valence band maximum. Using a combination of x-ray photoemission and hard x-ray photoemission spectroscopy, in conjunction with hybrid density-functional theory calculations, we have presented direct evidence for these active lone pairs in both GeS and GeSe, with interesting implications for the revised lone pair model and for related areas of research, such as Ge-based perovskites. The calculated electronic density of states of the midpoint $GeS_{0.5}Se_{0.5}$ was also found to match well with photoemission spectra, and reveals the presence of Ge 4s lone pairs at the valence band

edge as observed for the GeS and GeSe endpoints.

Ag-doped GeSe bulk crystals have successfully been synthesised by a melt growth method with no secondary phases resulting from the Ag incorporation. The CV, photoemission results and associated Poisson equation modelling show that the incorporated Ag led to the carrier concentration increasing from 5.2×10^{15} cm^{-3} to 1.9×10^{16} cm^{-3}. However, this is significantly lower than the Ag-content in the source materials of 1.6×10^{18} atoms cm^{-3} estimated from ICP-OES. Undoped and Ag-doped GeSe films were deposited onto both FTO/CdS and FTO/CdS/Sb_2Se_3, which were later processed into solar cells. The Ag-doped and undoped GeSe films with no Sb_2Se_3 interfacial layer exhibit similar XRD patterns with the (100) orientation dominating. The inclusion of the Sb_2Se_3 interfacial layer leads to the (111) orientation being more prominent. The two cell structures with no interfacial layer show a reasonable diode shape in the dark, but low overall cell performance in the light due to low current. The proposed causes are linked to either a narrow depletion region and/or a low carrier lifetime. The cell structure with Ag-doped GeSe with an Sb_2Se_3 interfacial layer did not work in the light or dark, with CV measurements suggesting a barrier at the interface. The cell structure with undoped GeSe and an Sb_2Se_3 interfacial layer shows the best device performance, with an efficiency of 0.260 %. This improvement in efficiency with the Sb_2Se_3 interfacial layer is consistent with increases proportion of (111) orientation, as also found in a previous study.[167] Despite the low device performance for the Ag-doped samples, the feasibility of Ag doping has been demonstrated and improved hole concentration should lead to improved device performance if low carrier lifetime and the interface barrier for the devices can be resolved.

Chapter 6

Properties and band alignments of $Sb_2(S,Se)_3$ alloys

6.1 Introduction

As discussed in Chapter 2, $Sb_2(S_xSe_{1-x})_3$ is more established than GeS_xSe_{1-x} as a lone pair material with applications in PV. In this Chapter, nine crystals of $Sb_2(S_xSe_{1-x})_3$ have been grown to investigate the structural properties of the series. The crystals were subsequently used as source material to deposit nine equivalent thin films via thermal evaporation. These films have been used to study the optical properties of the series. Five samples have been used to show how the band alignment with two common window layers, CdS and TiO_2 varies across the solid solution series, studied using the Kraut method. The experimentally determined structural and optical properties have been compared to the same properties calculated by DFT.

6.2 Literature review

6.2.1 Lattice parameters

The material has a nanoribbon structure, were covalently bonded nanoribbons along the [001] direction are held together by van der Waals interactions. Previous studies of the crystal structure of $Sb_2(S_xSe_{1-x})_3$ have shown lattice parameters which vary linearly with change in composition, as expected from Vegard's law. [313, 314] The lattice parameters, labelled in Figure 6.1 were determined as a is 11.63(1)Å to 11.24(1)Å, b is 11.78(1)Å to 11.33(2)Å, and c is 3.98(2)Å to 3.86(1)Å, for Sb_2S_3 to Sb_2Se_3, respectively. [315–320] These studies all use powder x-ray diffraction (XRD) or grazing incidence x-ray diffraction (GIXRD) to measure the lattice parameters. Theoretical studies of the lattice parameter change with composition of

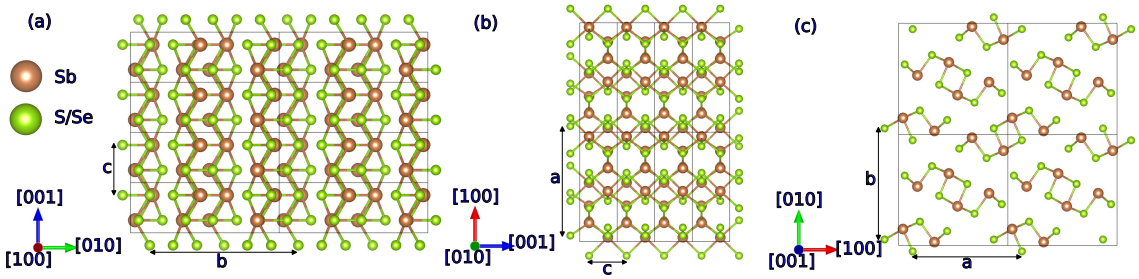

Figure 6.1: *The crystal structure of Sb_2Se_3 with lattice parameters a, b and c labelled. Here the outward facing face is [100], [010] and [001] are shown in (a), (b) and (c), respectively. [157, 323]*

$Sb_2(S_xSe_{1-x})_3$ have been limited: one shows an unsystematic and noisy variation of (overestimates) lattice parameters with temperature, whereas the second shows the lattice parameters of the end points matching known experimental literature values and a linear change in the bond length between the two end points.[321, 322]

6.2.2 Optical studies

When investigating a material for photovoltaic applications, one of the most important features is the band gap. For a single junction solar cell, the detailed balance limit suggests the ideal band gap is between 1.3-1.5 eV. [241] Meanwhile, for a two junction tandem solar-cell, the ideal wider band gap companion semiconductor for a silicon solar cell is between 1.6 and 2.3 eV. [142] A number of studies suggest the Sb_2S_3 band gap is indirect in the region of 1.70-1.74 eV but with multiple direct onsets within 0.1 eV. [162, 324–329] For Sb_2Se_3, the smallest direct transition has been shown to be direct and is 1.18 eV at room temperature, with multiple direct and indirect band gaps near to the onset of optical absorption. [330] For a compound such as $Sb_2(S_xSe_{1-x})_3$, the band gap typically varies linearly or bows with composition following the equation:

$$E_g(x) = E_g^0 x + E_g^1(1-x) - bx(1-x) \tag{6.1}$$

where E_g(x), E_g^0 and E_g^1 are the band gaps of $Sb_2(S_xSe_{1-x})_3$, Sb_2Se_3, and Sb_2S_3, respectively. x and b are the composition of interest and the bowing parameter, respectively. Previous studies of $Sb_2(S_xSe_{1-x})_3$ compounds suggest a small bowing parameter, in the region of 0.048 to 0.3096, which is consistent with other solid solution series as S and Se have similar electronegativity. [313, 316, 318, 331, 332] Other solid solution series with larger differences in electronegativity are known to have larger bowing parameter, such as ZnO_xS_{1-x} and $GaN_{1-x}Sb_x$ with bowing parameters of 3.0 and 2.7, respectively. [238, 239] All previous studies of the $Sb_2(S_xSe_{1-x})_3$ solid solution system have reported an incorrect band gap for at least one of the

end point compositions. This makes there reported band gap bowing parameters questionable. Fully understanding how the band gap varies will allow for the composition to be chosen in a way that will suit the specific application of interest. One theoretical study shows the band gaps decreasing from 1.30 eV to around 1.22 eV at $Sb_2(S_{0.25}Se_{0.75})_3$ before rising back up to 1.30 eV and staying consistent across the rest of the series. [322] This seems unlikely and is not supported experimentally. A second theoretical study shows a band gap bowing in a way similar to equation 1, with E_g^0, E_g^1 and b being predicted to be 1.17 eV, 1.64 eV and 0.266 eV, respectively. [333]

6.2.3 Band alignments

As well as the band gap, another important property for photovoltaic application is the conduction band alignment between the window and the absorption layer. [133] If the conduction band of the window layer is above that of the absorber layer, then it is said to have a positive conduction band offset (CBO) which is a spike-like barrier. If the CBO is negative instead, then the junction is said to be cliff-like. A large spike-like barrier leads to a barrier forming at the interface which will limit the short circuit current (J_{SC}). A cliff-like barrier increases the back-transfer carrier recombination, as well as reducing the built-in voltage, which will lower the open circuit voltage (V_{OC}).

There have been a number of previous band alignments proposed for the $Sb_2(S_xSe_{1-x})_3$ solid solutions with both common window layers CdS and TiO_2. Early studies of the band alignment of $Sb_2(S_xSe_{1-x})_3$ show a small and flat negative CBO of 0.5 eV and 0.2 eV with TiO_2 and CdS, respectively, throughout the alloy series. [334–338] This result is based on studies of the band alignments of the end points. For Sb_2Se_3, the results come from a cyclic voltammetry study whereas for Sb_2S_3, the VBM is calculated with density functional theory and the experimentally known band gap is added to find the CBM. [339–341] A common approach is to use photoemission spectroscopy to find the VBM relative to vacuum level by measuring the valence band position and the secondary electron cut-off, with the band gap then added on to determine the CBM. [287] All previous photoemission studies on $Sb_2(S_xSe_{1-x})_3$ have been done with ultraviolet photoemission spectroscopy (UPS). One involved a systematic study of five compositions from $Sb_2(S_{0.6}Se_{0.4})_3$ to Sb_2S_3 which showed the value, relative to the vacuum level, of the VBM varying linearly from -5.12 eV to -5.30 eV with the CBM staying consistent at -3.6 eV. [342] The position of the VBM is consistent with other measurements, though the band gaps are not known well, as discussed above, which leads to discepencies in the CBM positions. [343–346] Furthermore, using these techniques to find band alignments relies upon a consistently

known value for the VBM and CBM, relative to the vacuum level, for both CdS and TiO_2 which does not seem to be consistent within the $Sb_2(S_xSe_{1-x})_3$ literature.

A more comprehensive, but challenging, way of using photoemission to measure the band alignment is the Kraut method. [347] This technique uses multiple measurements to directly quantify the offset between two materials, having the advantage over other techniques that it takes into account charge transfer between the two materials and, additionally, involve measurements of thick layers of the two materials. A thin film of one of the materials is required to be deposited onto the second, thin enough that a photoemission measurement can detect photoelectrons from the bottom film. This two layer sample is called referred to as a bilayer below. In this study, the band alignment between the window layers (CdS or TiO_2) and the absorber layer ($Sb_2(S_xSe_{1-x})_3$) were measured and calculated using the Kraut method. The window layer in this study was always be the bottom layer (material A) whereas the absorber layer was the top layer (material B). The equation in the Kraut method is:

$$\Delta E_V = (E^B_{CL} - E^B_V) - (E^A_{CL} - E^A_V) + \Delta E_{CL} \tag{6.2}$$

where ΔE_V is the VBO between material A and B using a core level and valence band position, E_{CL} and E_V respectively. ΔE_{CL} is the difference between the core levels in the bilayer sample (i.e. $\Delta E_{CL} = E^{A-M}_{CL} - E^{B-M}_{CL}$).

As discussed above, previous studies of band alignments for the $Sb_2(S_xSe_{1-x})_3$ solid solution series used UPS. However, the inelastic mean free path (IMFP) of photoelectrons generated by UPS is less than 1 nm whereas standard lab-based x-ray photoemission spectroscopy (XPS) gives an IMFP of ∼3 nm. The Beer-Lambert law states that 95% of the photoelectrons will be generated within the first three IMFP of the surface. This limits the ability to use UPS or XPS for the Kraut method to detect the bottom film in the ΔE_{CL} measurement, as they cannot detect the bottom film unless the top film is sufficiently thin (≤5 nm). An alternative photoemission technique, hard XPS (HAXPES) uses high energy x-rays generated from synchrotron, from which the photoelectrons have an IMFP of 9 nm. This allows for the top film to be thicker (∼20 nm) and thus are more representative of the films used in actual cells.

6.3 Experimental methods

Crystals were prepared by a melt growth technique. Stoichiometric amounts of Sb, S and Se (all with 5N purity, Alfa Aesar) were sealed in an evacuated quartz tube at a pressure $\leq 10^{-4}$ mbar. The mixtures were melted at 625°C for 24 hours, then

cooled to 350°C at a rate of 0.3°C min^{-1} where the mixture was held for 100 hours, before finally being cooled to room temperature.

CdS films were deposited on SnO_2:F-coated soda lime glass substrate (TEC15, NSG Group) by RF-magnetron sputtering at 1.32 W cm^{-2}, 5 mTorr of Ar gas and a substrate temperature of 200°C for 30 minutes to give a film with thickness 100 nm for all devices. To deposit TiO_2 on TEC15, two spin coats of titanium isoproxide in ethanol (0.3M) at 3000 rpm for 30 seconds were deposited on TEC15 in a glove box. A drying stage (120°C for 10 minutes) after each spin coat was performed in the glove box, and a final anneal in air at 500°C for 30 minutes. Five thin films with compositions across the $Sb_2(S_xSe_{1-x})_3$ series, including the two end points, were deposited via thermal evaporation at a rate of 2Å/s onto either CdS or TiO_2 coated substrates to a total thickness of 18-20 nm, allowing core levels of both the $Sb_2(S_xSe_{1-x})_3$ layer and the CdS or TiO2 substrate to be observed in HAXPES measurements. A thicker $Sb_2(S_xSe_{1-x})_3$ layer (150 nm) was also deposited directly onto TEC15 substrates for each composition for thick film measurements. Film thickness was monitored using a quartz microbalance calibrated with an Ambios XP-200 surface profilometer. Films were then annealed at 325°C for 30 minutes in an N_2 atmosphere.

Samples were prepared for ICP-OES by dissolving ∼10 mg of the grown crystals ground to powder in a solution containing 1 ml HCl (37 wt%) and 2 ml HNO_3, which was subsequently diluted to 4 vol.% acid concentration in deionised water for measurement. ICP-OES was measured on solutions using an Agilent 5110 ICP-OES spectrometer to test for selenium and sulfur. The emission intensity was linearly calibrated at five known levels of concentration for each emission wavelength. For selenium the emission wavelengths measured were 196.026 nm and 206.279 nm, and for sulfur the emission wavelengths measured were 180.669 nm, 181.972 nm and 182.562 nm. Samples of deionised water and diluted acid were also analysed to determine any background levels of the relevant elements in the solution.

The phase and purity of both powder and polycrystalline films were confirmed using a Rigaku Smartlab x-ray diffractometer, with a rotating copper anode, under ambient conditions. Monochromated incident radiation (Cu Kα_1) was used to perform θ:2θ scans carried out between 20° and 80° at 0.5° min^{-1} in parallel beam geometry for both powder and film measurements.

HAXPES measurements were collected at beamline I09 at the Diamond Light Source facility, UK in a standard ultrahigh vacuum (UHV) chamber with a pressure of $< 1\times10^{-10}$ mbar. A Si(004) channel-cut crystal, following a double-crystal Si(111) monochromator, was used to select x-rays from the source (hv = 5.921 keV). Measurements were made using a Scienta Omicron EW4000 high-energy analyzer with an acceptance angle of ±28°. Calibration was performed using a gold sample,

x	a (Å) ±0.03	b (Å) ±0.02	c (Å) ±0.005	Volume (Å^3) ±0.5	Band gap (eV) ±0.02
0	11.66	11.79	3.971	546.1	1.19
0.136±0.003	11.57	11.75	3.955	537.7	1.23
0.231±0.003	11.55	11.70	3.939	532.0	1.27
0.330±0.007	11.52	11.65	3.923	526.7	1.31
0.477±0.004	11.43	11.59	3.908	517.9	1.39
0.651±0.002	11.39	11.49	3.877	507.4	1.47
0.706±0.006	11.38	11.48	3.869	505.1	1.49
0.814±0.009	11.34	11.44	3.844	499.2	1.58
1	11.25	11.35	3.832	489.5	1.71

Table 6.1: *All compositions of $Sb_2(S_xSe_{1-x})_3$ (measured by ICP-OES) with the lattice parameters (measured using powder XRD) and the band gap (measured using the films by UV-VIS spectrophotomer).*

enabling the energy resolution of 0.25 eV to be determined by fitting the Fermi edge with a Fermi-Dirac function convolved with Gaussian and Lorentzian peaks. The uncertainty in energies from HAXPES is ±0.03 eV for core level peaks.

Fittings were done using the CASA XPS software using a Shirley background and a computational combination of a Gaussian and Lorentzian which allows for the separate contributions from instrumental and lifetime broadening to be accounted for. The full width half maximum of the doublets are constrained to be equal as is standard, except the Ti 2p doublet which is unconstrained because of the Coster-Kronig effect. [348, 349] The area ratios are typically 2:1 and 3:2 for p and d orbitals, respectively. However, the area ratios are known to change for higher x-ray energies so were ratios were taken for each orbital from previous photoionization cross-section calculations. [180]

All DFT calculations presented here use the optB86b-vdW functional to determine the structure of each of the structures. [350] The structures were then applied to HSE06 to calculate electronic and optical properties. [187] More details are available in Reference [351].

6.4 Results and discussion

6.4.1 Structural properties

ICP-OES was used to determine the sulfur to selenium ratio of the solid solutions. The calculation method is shown in the supplementary information and the compositions are shown in Table 6.1. Using ICP-OES enables the S:Se ratio to be determined to an accuracy in the range 0.3-2.9%. This is much better than the typ-

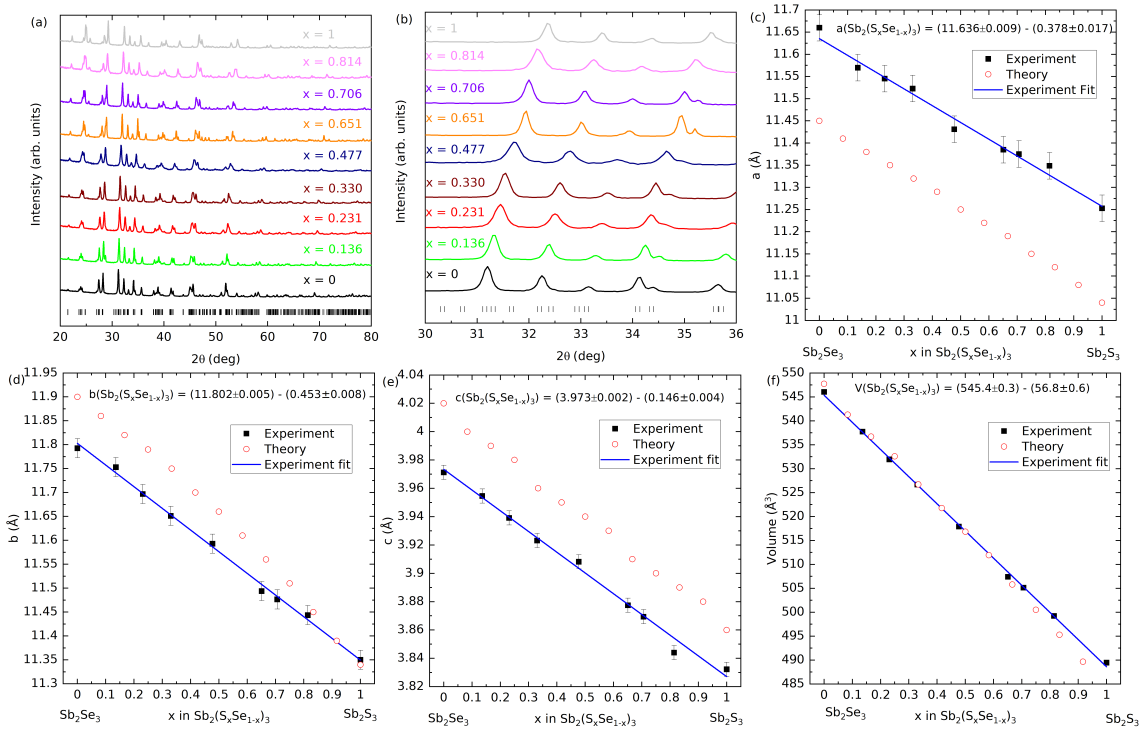

Figure 6.2: *(a) The powder XRD measurement for all compositions of $Sb_2(S_xSe_{1-x})_3$ used in this study, with the 30° to 36° region in (b). Included in both (a) and (b) are the Bragg peak positions of Sb_2Se_3 from previous literature. [323] These results are then used to find the lattice parameter values a, b, c, and volume which are shown (c), (d), (e), and (f), respectively.*

ical measurements with energy-dispersive x-ray spectroscopy (EDX) which is subject to systematic errors that can lead to inaccurate determinations of major element compositions, in some cases up to several tens of percent depending on the sample composition and correction algorithm used.

Figure 6.2(a) shows the powder XRD measured on all ground up bulk crystals. The Bragg peak positions are taken from a previously published study on the crystal structure of Sb_2Se_3, which agree well with our experimental data. [323] In Figure 6.2(b), the powder XRD is zoomed in at 30° to 36° which shows reflections 212, 013, 113, 402, 204, and 312 at 2θ values of 31.11°, 32.16°, 33.07°, 34.05°, 34.32°, and 35.56°, for Sb_2Se_3 respectively. All reflections shift continuously from one end point to the other, providing strong evidence the crystals have grown as a solid solution.

Powder XRD was used to calculate the lattice parameters using reflections 211, 301, and 240 as discussed in our study of GeSe. [352] For reference the a, b and c lattice parameters are indicated with regards to the ribbon direction on the structure diagram in Figure 6.1. XRD analysis results are presented in Table 6.1 and shown as a function of x graphically in Figure 6.2(c)-6.2(f). The lattice parameters of Sb_2S_3 and Sb_2Se_3 agree well with the previously published reports, and the lattice parameters of the solid solutions linearly vary between the two end points, as

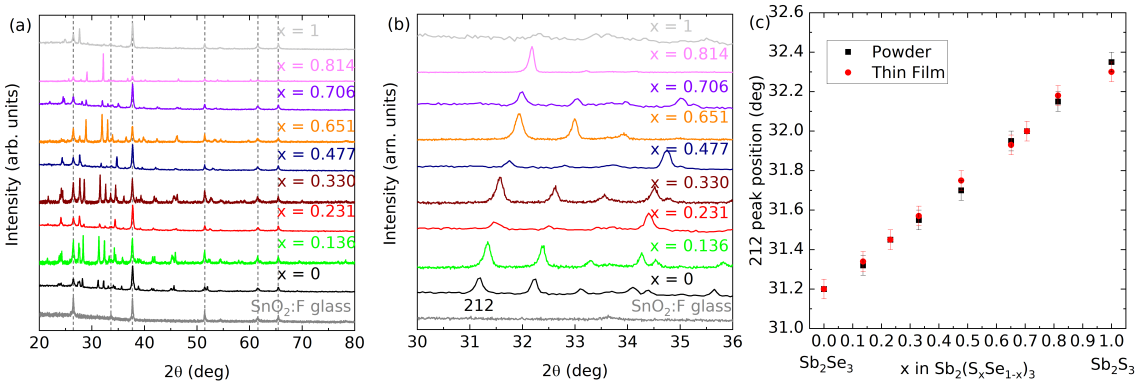

Figure 6.3: *(a) Thin film XRD measurement of the thick film sample with the measurements zoomed into the region of 30° to 36° in (b). (c) The position of the 212 reflection in powder and thin film XRD is compared for the each composition.*

expected. [323, 353] The results shown have linear fits of:

$$a(x) = 11.636 \pm 0.009 - (0.378 \pm 0.017)x \tag{6.3}$$

$$b(x) = 11.802 \pm 0.005 - (0.453 \pm 0.008)x \tag{6.4}$$

$$c(x) = 3.973 \pm 0.002 - (0.146 \pm 0.004)x \tag{6.5}$$

$$V(x) = 545.4 \pm 0.3 - (56.8 \pm 0.6)x \tag{6.6}$$

where the lattice parameters are in Å and the cell volume is in Å^3. These fits agree well with the $Sb_2(S_xSe_{1-x})_3$ results published previously. [315–320]

Furthermore, comparisons are made in Figure 6.2(c) to 6.2(f) between the lattice parameters measured here and the lattice parameters calculated by DFT. The theory underestimates the lattice parameter a by around 0.20-0.25 Å and overestimates the lattice parameter c by around 0.03-0.05 Å. The theory overestimates lattice parameter b at the Se-rich end of $Sb_2(S_xSe_{1-x})_3$ series but converges to the experimentally determined value at the S-rich end of the series. As shown in 6.2(f), the experimentally measured and theoretically calculated lattice volumes agree well.

6.4.2 Thin film XRD

All bulk crystals previously discussed were used as source materials for depositing thin films of the materials using thermal evaporation. The deposition was followed by a 325°C thermal anneal for 30 minutes under N_2 to convert the initially amorphous layers into polycrystalline thin films. Figure 6.3(a) shows the thin film XRD for all films including the thick film samples for the HAXPES measurements below. The dashed lines indicate the XRD peak positions of the fluorine-doped tin oxide (F:SnO_2) substrate which provides a significant proportion of the intensity as

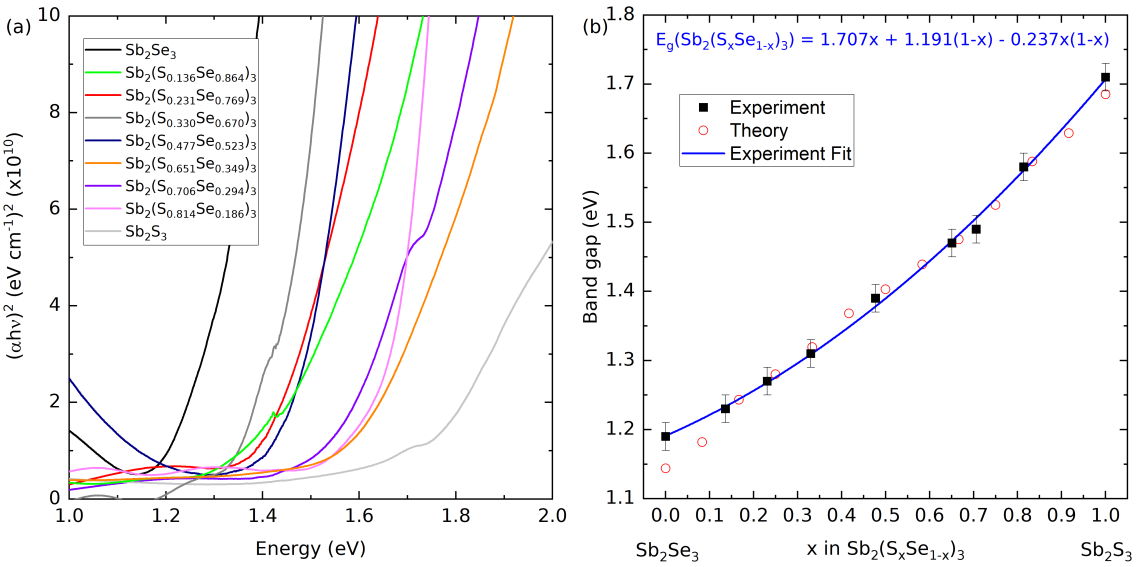

Figure 6.4: *(a) $(\alpha h\nu)^2$ vs $h\nu$ to show the measured direct band gaps. (b) The band gap vs x in $Sb_2(S_xSe_{1-x})_3$ is shown with the experimental fit.*

the films are only ∼150-500 nm thick. Shown in Figure 6.3(b) is the region 30° to 36° which shows the reflection 212 (labelled for Sb_2Se_3) shifting linearly from one end point composition to the other. In Figure 6.3(c) the 212 reflection position in both the powder and thin film XRD are shown. The reflection positions are consistent for the powder and thin film providing evidence that the material evaporated congruently and the deposited film is the same composition as the source material.

6.4.3 Optical properties

The optical properties of the $Sb_2(S_xSe_{1-x})_3$ series were then determined from measurements of the thin films. When using absorption spectroscopy to measure the band gap, it is normal to plot either $(\alpha h\nu)^2$ or $(\alpha h\nu)^{\frac{1}{2}}$ for a direct or indirect band gap, respectively. We perform the analysis assuming a direct band gap as for absorption spectroscopy of materials which have very close direct and indirect transitions (like Sb_2S_3 and Sb_2Se_3) as the direct transitions will dominate the absorption as shown in prior work. [225]

Figure 6.4(a) plots the $(\alpha h\nu)^2$ vs $h\nu$ to show how the smallest direct band transition was measured for compositions $x = 0$, 0.231, 0.477, 0.706 and 1, the remaining compositions are provided in the supplementary information. For materials like Sb_2S_3 and Sb_2Se_3 which have multiple transitions near to the band gap, $(\alpha h\nu)^2$ will be nonlinear at the onset. This nonlinear onset introduces a degree of subjectivity to the fitting range used for the standard Tauc analysis, and is therefore considered unreliable for this solid solution series. Instead, third derivative analysis is used to identify the lowest direct band gap, an approach well established for modulation

reflectance optical spectroscopies [236], and also has some benefit for identifying features in optical absorption data. [237] The smallest direct transitions are shown in Figure 6.4(b) and included in Table 6.1. The fit for the smallest direct transitions of $Sb_2(S_xSe_{1-x})_3$ (E_g(x)) is given by equation:

$$E_g(x) = 1.707x + 1.191(1-x) - 0.237x(1-x) \tag{6.7}$$

where the values 1.707, 1.191, and 0.237 are the Sb_2S_3 smallest direct transition, Sb_2Se_3 smallest direct transition, and bowing parameter, respectively. Unlike previous reports studying the band gap change across the full solid solution series, both end points agree well with the literature for Sb_2S_3 and Sb_2Se_3. The bowing parameter is small which is sensible given the similar electronegativity and atomic size of sulfur and selenium. From a photovoltaic (PV) perspective, the ideal band gap for a single junction device absorber would be between 1.3-1.5 eV. [241] These results show the ideal composition for PV to lie between $Sb_2(S_{0.3}Se_{0.7})_3$ and $Sb_2(S_{0.7}Se_{0.3})_3$.

The experimental results and theoretical calculations are compared on Figure 6.4(b). Previous studies suggest that the Sb_2Se_3 has a band gap of 1.32 eV at 0 K. [330] Theoretical band gaps are calculated at 0 K and so the two should not be directly compared. However, the two show excellent agreement with the only divergence coming at the Se-rich end of the solid solution series, which shows the calculated band gaps to be lower than those measured in the experiment. This agreement suggests that the theory is predicting how the band gap is varying with composition well but there is a systematic underestimate of the band gap for all compositions.

6.4.4 Band alignment

Finally, HAXPES measurements were performed on five thick samples of $Sb_2(S_xSe_{1-x})_3$ with compositions x = 0, 0.231, 0.477, 0.706 and 1, as well as thick samples of CdS and TiO_2. Furthermore, bilayer samples having both $Sb_2(S_xSe_{1-x})_3$ and the window layer were measured for the five compositions with each window layer type. All these measurements combined were then be used to calculate the band alignments of every composition with both window layers. An example of how the calculations were performed for $Sb_2(S_{0.231}Se_{0.769})_3$ with both window layers CdS and TiO_2 is included in Figure 6.5. As described in the introduction, the Kraut equation assigns material A and B as the window layer and $Sb_2(S_{0.231}Se_{0.769})_3$ films, respectively. Figure 6.5(d) and 6.5(e) show E^B_{CL} and E^B_V, respectively, for both band alignment calculations. For calculating the band alignment of CdS and $Sb_2(S_{0.231}Se_{0.769})_3$, Figure 6.5(b), 6.5(c), and 6.5(a) show E^A_{CL}, E^A_V, and ΔE_{CL}, respectively. For calculating the band alignment of TiO_2 and $Sb_2(S_{0.231}Se_{0.769})_3$, Figure 6.5(f), 6.5(g), and 6.5(h)

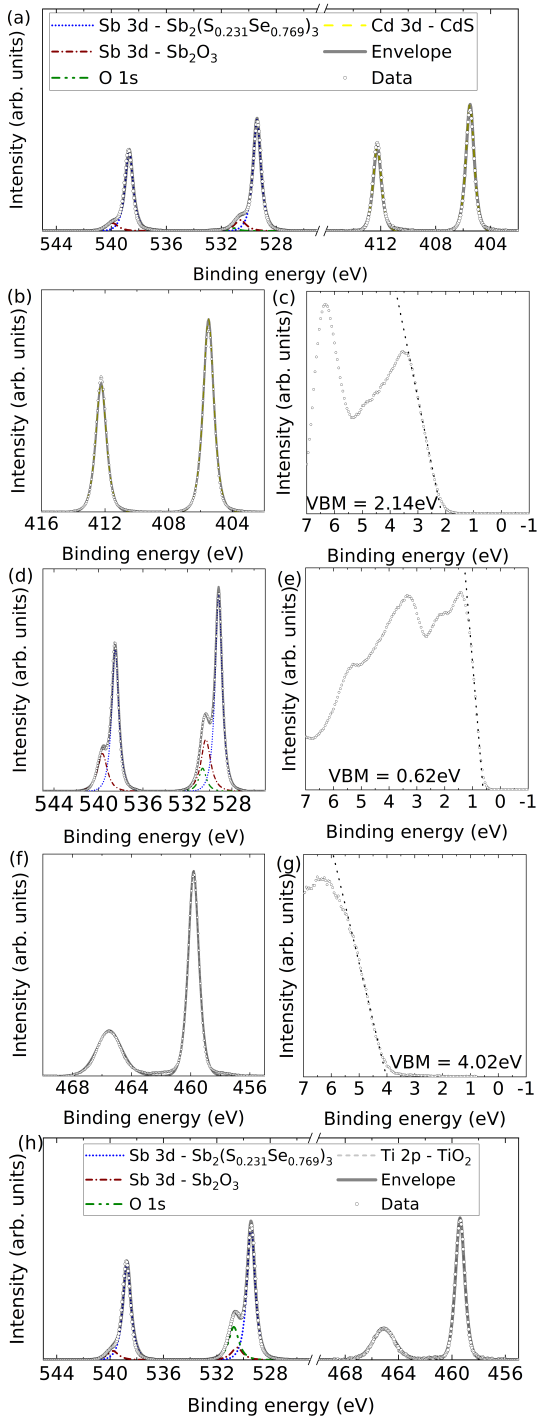

Figure 6.5: *(a) Sd 3d and Cb 3d core level for the $CdS/Sb_2(S_{0.231}Se_{0.769})_3$ bilayer. (b) and (c) are the Cd 3d and valence band position, respectively, for the CdS thick film sample. (d) and (e) are the Sb 3d and valence band position, respectively, for the $Sb_2(S_{0.231}Se_{0.769})_3$ thick film sample. (f) and (g) show the Ti 2p and valence band position, respectively, for the TiO_2 thick film sample. (h) Sb 3d and Ti 2p core level for the $TiO_2/Sb_2(S_{0.231}Se_{0.769})_3$ bilayer sample, respectively.*

Kraut parameter	$TiO_2/Sb_2(S_{0.231}Se_{0.769})_3$ (eV)	$CdS/Sb_2(S_{0.231}Se_{0.769})_3$ (eV)
E_{CL}^A	459.81	405.51
E_V^A	4.02	2.14
E_{CL}^B	529.19	529.19
E_V^B	0.62	0.62
E_{CL}^{A-M}	459.40	405.51
E_{CL}^{B-M}	529.44	529.44

Table 6.2: *Fitted values from core levels and valence band maximum positions in Figure 6.5 used to calculate the Kraut-method band alignments for TiO_2 and CdS with $Sb_2(S_{0.231}Se_{0.769})_3$. For the TiO_2 and $Sb_2(S_{0.231}Se_{0.769})_3$ Kraut-method band alignment, E_{CL}^A and E_V^A are the Ti $2p_{\frac{3}{2}}$ and the valence band position from the thick TiO_2 sample, respectively. For that same band alignment, E_{CL}^B and E_V^B are the Sb $3d_{\frac{5}{2}}$ and the valence band position, respectively, while the E_{CL}^{A-M} and E_{CL}^{B-M} are the same core levels but in the interfacial sample. Similarly, for the CdS and $Sb_2(S_{0.231}Se_{0.769})_3$ Kraut-method band alignment, E_{CL}^A and E_V^A are the Cd $3d_{\frac{5}{2}}$ and the valence band position, respectively. E_{CL}^B and E_V^B are the same as the previous band alignment, while E_{CL}^{A-M} and E_{CL}^{B-M} are the Cd $3d_{\frac{5}{2}}$ and Sb $3d_{\frac{5}{2}}$ in the interfacial sample, respectively.*

show E_{CL}^A, E_V^A, and ΔE_{CL}, respectively.

The fittings in Figure 6.5(a) and 6.5(b) show the Cd 3d core level spectra and Figure 6.5(f) and 6.5(h) show the fittings for the Ti 2p core level spectra. None show any evidence of any contamination. Sb 3d spectra are shown in Figure 6.5(a), 6.5(d) and 6.5(h) with the fittings showing $Sb_2(S_{0.231}Se_{0.769})_3$ dominating the signal but with some Sb_2O_3 and the O 1s also present.

The cation core level peak positions of the $Sb_2(S_{0.231}Se_{0.769})_3$, CdS, and TiO_2 were used, see Table 6.2, for the Kraut method VBO determination. The VBO for $Sb_2(S_{0.231}Se_{0.769})_3$ with CdS and TiO_2 were found to be -1.28 eV and -2.74 eV, respectively. The CBO were then calculated by adding on the window layer band gap and then subtracting the band gap of $Sb_2(S_{0.231}Se_{0.769})_3$. The CBO for $Sb_2(S_{0.231}Se_{0.769})_3$ with CdS and TiO_2 were found to be -0.81 eV and -0.13 eV, respectively. Please see Section 2.3 and Figure 2.5 for more details about a negative CBO.

Performing the same calculations for Sb_2S_3, $Sb_2(S_{0.484}Se_{0.516})_3$, $Sb_2(S_{0.706}Se_{0.294})_3$ and Sb_2Se_3 allowed for the change in VBO and CBO to be found across the composition range. Note that no value for the offset between CdS and $Sb_2(S_{0.706}Se_{0.294})_3$ is included because the sample of $CdS/Sb_2(S_{0.706}Se_{0.294})_3$ charged during photoemission measurements so ΔE_{CL} could not be found. Multimeter readings across this sample show it to be highly resistive explaining its charging behaviour.

For both CdS and TiO_2, in Figure 6.6(a), the VBO is shown to decrease (becom-

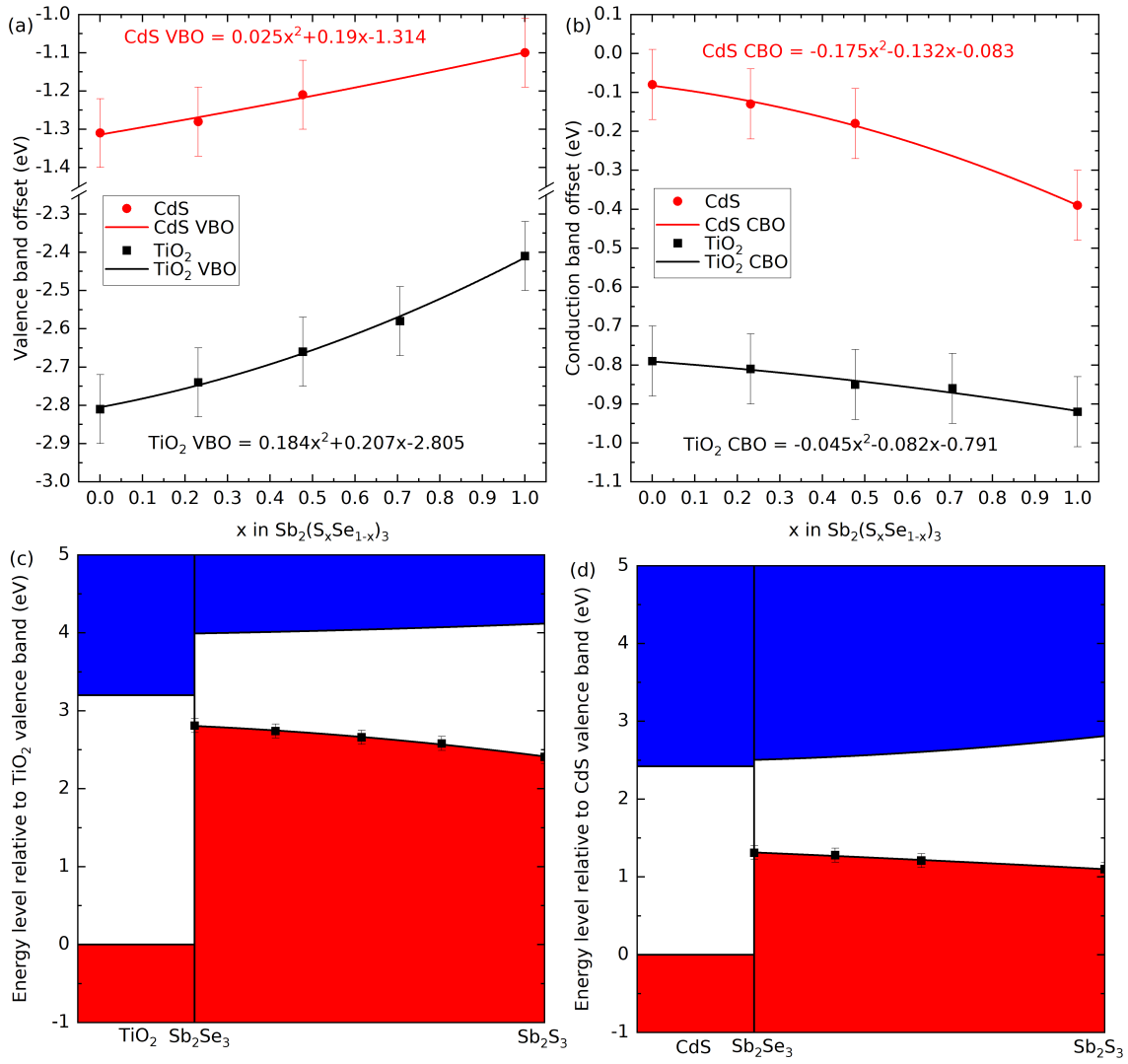

Figure 6.6: *(a) The Kraut method-determined valence band offsets (VBO) for all compositions with both TiO_2 and CdS and a linear fit is applied to show the change in VBO across the composition range. (b) Shows the calculated conduction band offsets (CBO) using the band gaps found in Figure 6.4(b), again with a linear fit to show the change across the composition range. The calculated band diagrams for the composition range with TiO_2 and CdS is shown in (c) and (d), respectively.*

ing less negative) as the sulfur content increases and thus the Sb chalcogenide solid solution valence band moves down as the S-content increases. In Figure 6.6(b), the CBO is shown to increase (more negative) as the sulfur content increases, and this again corresponds to the conduction band moving up as the S-content increases.

The VBO for $Sb_2(S_xSe_{1-x})_3$ with TiO_2 is shown in Figure 6.6(a) to bow across the composition range whereas it is shown in Figure 6.6(b) the CBO bowing parameter is close to zero, suggesting the change in CBO across the Sb chalcogenide solid solution series is essentially linear. On the other hand, the VBO for $Sb_2(S_xSe_{1-x})_3$ with CdS is shown in Figure 6.6(a) to have a bowing parameter close to zero, suggesting the VBO change is essentially linear. The CBO is shown in Figure 6.6(b) between $Sb_2(S_xSe_{1-x})_3$ and CdS is shown to bow across the composition range. The two band alignments are illustrated in Figure 6.6(c) and 6.6(d) for TiO_2 and CdS, respectively, with the measured VBO data points shown.

It is worth noting that with the Kraut method we are measuring the band alignment for ~20 nm $Sb_2(S_xSe_{1-x})_3$ films with the window layers rather than the natural band alignment. Unlike natural band alignment measurement, the Kraut-method band alignment measurements take into account the charge transfer between the two materials. Previously published work comparing the natural and Kraut-method band alignments of the Sb_2Se_3 end point with both CdS and TiO_2 shows minimal difference between the two measurements for Sb_2Se_3 with CdS, but the offset between Sb_2Se_3 and TiO_2 is found to be larger for Kraut-method (0.82 eV) rather than natural band alignment (0.11 eV). [133] The electronegativities for all the cations, Ti, Cd and Sb, are similar, with values of 1.54, 1.69 and 2.05, respectively. However, the electronegativity of 3.44 for the anion O, is considerably larger than the electronegativities of 2.58 and 2.55 for the other anions of S and Se, respectively. This larger electronegativity for the oxygen in TiO_2 could lead to a larger charge transfer between Sb_2Se_3 and TiO_2 than Sb_2Se_3 and CdS. [354, 355]

The band alignment results suggest that the CBO for all Sb-chalcogenide solid solutions is smaller for CdS than for TiO_2, meaning an improved built-in voltage at the interface. Therefore, solely from a band-alignment perspective, for PV, CdS rather than TiO_2 is the preferred window layer for $Sb_2(S_xSe_{1-x})_3$. However, this must be balanced with other considerations. For example, there are greater parasitic losses associated with CdS than TiO_2 due to the smaller band gap of CdS (2.4 eV) compared with TiO_2 (3.2 eV). Additionally, there is evidence of intermixing between CdS and Sb_2Se_3 which some have suggested make TiO_2 the better window layer. [169]

Furthermore, the band alignments with both CdS and TiO_2 suggest that the Se-rich end of the $Sb_2(S_xSe_{1-x})_3$ solid solution series will have lower losses associated with the band alignment. However, the results from the band gap measurements

suggest that the ideal composition for PV, based on the detailed balanced limit, is between $Sb_2(S_{0.3}Se_{0.7})_3$ and $Sb_2(S_{0.7}Se_{0.3})_3$. These result shows how compromises are needed when designing $Sb_2(S_xSe_{1-x})_3$ solar cells. Future work will be required to assess how these compromises are made to maximise the efficiencies of the cells with these results providing an excellent framework for making those decisions.

6.5 Conclusion

Nine different compositions of $Sb_2(S_xSe_{1-x})_3$ bulk crystals have been grown using a melt growth technique. The composition of each has been measured using ICP-OES. The bulk crystals were used as source material for thermal evaporation of each of the solid solutions. The films were confirmed to have compositions consistent with the crystals using XRD. The experimental results were compared to theoretical calculations performed using a supercell model of the solid solution using density functional theory.

Powder XRD was used to find the lattice parameters and were shown to vary linearly across the composition range. The theory underestimates lattice parameters a and overestimates lattice parameter c, but the overall volume of the lattice is in good agreement with experiment.

The smallest direct band gap for $Sb_2(S_xSe_{1-x})_3$ is found to vary according to $E_g(x)$=1.707x+1.191(1-x)-0.237x(1-x). The experimental and theoretical band gap values show excellent agreement for the band gap.

The band alignments of five compositions of $Sb_2(S_xSe_{1-x})_3$ with the common window layers CdS and TiO_2 are performed using HAXPES and analysed using the Kraut method. It is found that the VBO decreases for both window layers and the CBO increases for both window layers. The bow in the band gap presents itself in the VBO for the TiO_2 with $Sb_2(S_xSe_{1-x})_3$ whereas the bow in the band gap presents itself in the CBO for the TiO_2 with $Sb_2(S_xSe_{1-x})_3$. The CBO for all Sb-chalcogenide solid solutions with CdS is lower than with TiO_2, suggesting that there will be lower losses associated with the band alignment if CdS is used. From a PV perspective, the band-alignment measurements suggest the Se-rich end of the $Sb_2(S_xSe_{1-x})_3$ series will have lower losses, but this finding must be balanced with the optical results which suggest an ideal composition between $Sb_2(S_{0.3}Se_{0.7})_3$ and $Sb_2(S_{0.7}Se_{0.3})_3$ when choosing the composition of the absorber layer within solar cells.

Chapter 7

Conclusions and Future Work

7.1 Conclusions

The aim of this project was to understand the GeS_xSe_{1-x} and $Sb_2(S_xSe_{1-x})_3$ alloy series in more depth, with a view to future applications in photovoltaics.

In Chapter 4, the growth of nine compositions of the GeS_xSe_{1-x} alloy series was reported and they where used to study the thermal, structural and optical properties. The melting point is shown to bow between the two end points with a minimum of 626°C at $GeS_{0.766}Se_{0.234}$. The lattice parameters decrease linearly with increasing sulfur content. Experimentally-determined direct optical band gaps were found to vary approximately linearly with increasing sulfur content from 1.30 eV for GeSe to 1.64 eV for GeS. These experimental studies are supported by first-principles modelling of the thermodynamics and physical properties of the alloys. The model indicates entropically-driven near-ideal mixing. The predicted lattice parameters agree well with measurements for the GeSe endpoint but deviate somewhat at S-rich compositions. The calculated band gaps are underestimated compared to optical characterisation but show a very similar trend as a function of composition.

Chapter 4 includes a case study of the GeSe fundamental absorption onset which is found to be 1.30 eV at room temperature, close to the optimum value according to the detailed balance limit, in contrast to previous reports of an indirect fundamental transition of 1.10 eV. The measured absorption spectra and first-principles joint density of states are mutually consistent, both exhibiting an additional distinct onset ∼0.3 eV above the fundamental absorption edge. The band gap values obtained from first-principles calculations converge, as the level of theory and corresponding computational cost increases, to 1.33 eV from the quasiparticle self-consistent GW method, including the solution to the Bethe-Salpeter equation. This agrees with the 0 K value determined from temperature-dependent optical absorption measurements. Relaxed structures based on hybrid functionals reveal a direct fundamental

transition in contrast to previous reports. The optoelectronic properties of GeSe are resolved with the system described as a direct band gap semiconductor with a 1.30 eV room temperature band gap. The high level of agreement between experiment and theory encourages the application of this computational methodology to other van der Waals materials.

In Chapter 5, the preparation of GeS and GeSe bulk crystals is reported. The same melt growth technique was used as for the samples in Chapter 4. XPS was used to determine ionisation potentials of 5.74 and 5.48 eV for GeS and GeSe respectively. These values were used with the previously-measured band gaps to establish the natural band alignments with potential window layers for photovoltaic devices and to identify CdS and TiO_2 as sensible choices. The ionisation potential of GeS is found to be smaller than in comparable materials. Using XPS and HAXPES measurements in conjunction with density-functional theory calculations, we demonstrate that stereochemically active Ge $4s$ lone pairs are present at the valence-band maxima. Our work thus provides direct evidence for active lone pairs in GeS and GeSe, with important implications for the applications of these and related materials such as Ge-based perovskites.

Additionally in Chapter 5, GeSe bulk crystals, thin films and solar cells were investigated with a focus on acceptor-doping with silver and the use of an Sb_2Se_3 interfacial layer. The Ag-doping of GeSe occurred by the same stoichiometric melt growth technique that created the GeS_xSe_{1-x} bulk crystals. A combination of capacitance voltage measurements, photoemission spectroscopy and surface space-charge calculations indicated Ag-doping increased the hole density from 5.2×10^{15} cm^{-3} to 1.9×10^{16} cm^{-3}. The melt-grown material was used as the source for thermally evaporated GeSe films within solar cells. The cell structure with the highest efficiency of 0.260 % was FTO/CdS/Sb_2Se_3/undoped-GeSe/Au compared with solar cells without the Sb_2Se_3 interfacial layer or with the Ag-doped GeSe.

In Chapter 6, the preparation of nine compositions of $Sb_2(S_xSe_{1-x})_3$ bulk crystals is reported. These where used to study the structual and optical properties. The lattice parameters were shown in the experiment to decrease linearly with increased sulfur content. The experimentally determined band gap was shown to vary between 1.19 eV and 1.71 eV for Sb_2Se_3 and Sb_2S_3, respectively, with a bowing parameter of 0.237. The experimental results for the lattice parameters and band gaps were compared with theoretical models for the Sb-chalcogenide alloy series. They were shown to be in good agreement with each other. The band alignment between the $Sb_2(S_xSe_{1-x})_3$ series and common window layers CdS and TiO_2 was also studied. The results show that the alignment between $Sb_2(S_xSe_{1-x})_3$ and CdS has a smaller conduction band offset than $Sb_2(S_xSe_{1-x})_3$ and TiO_2, suggesting CdS is the preferred window layer from a band alignment perspective. The band alignment results also

suggest that the Se-rich end of the Sb-chalcogenide alloy series would lead to less current losses, but this result must be considered alongside the band gap results which suggest the ideal composition (x) is between 0.3 and 0.7, so compromises must be made.

7.2 Future Work

There is planned further work for both material series. For the GeS_xSe_{1-x} alloy series, there are plans to compare the Raman and infrared modes with theory to investigate how well the theory reproduces the experimentally observed changes with composition. The main work for this alloy series though is to progress the device performance. The possible reasons for the discrepancies between our device results and those of the record efficiency devices are discussed in Chapter 5. We speculate that one possible reason is the difference in the crystal orientation of the GeSe within the device. If we deposited onto a heated substrate, then we could possibly get a different orientation. The closed space sublimated (CSS) set up will be ideal for doing this alternative deposition technique. This technique has the advantage of already being used at industrial scale for thin film solar cells.

For the $Sb_2(S_xSe_{1-x})_3$ alloy series, the proposed future work will go further in comparing the theory and experiment. There are plans to compare the valence band photoemission results with the nearest calculated alloy's density of states using the same approach as in Chapter 5. Furthermore, the group performing the calculations hope to use a novel methodology to calculate the real band alignment offset between the different compositions and the chosen window layers. The ability to calculate band alignments between two materials would be beneficial for PV and multiple other applications. There is also ongoing work to fabricate CSS $Sb_2(S_xSe_{1-x})_3$ PV devices using different compositions and investigating different dopants. Increases in the power conversion efficiency of devices employing absorbers from the $Sb_2(S_xSe_{1-x})_3$ alloy series are regularly being reported and further work will certainly be done to increase them even more.

Bibliography

[1] D. W. Kweku, O. Bismark, A. Maxwell, K. A. Desmond, K. B. Danso, E. A. Oti-Mensah, A. T. Quachie, and B. B. Adormaa. Greenhouse effect: greenhouse gases and their impact on global warming. *Journal of Scientific Research and Reports*, 17:1–9, 2018.

[2] Working Group I. The physical science basis. Technical report, Intergovernmental Panel on Climate Change, 2021.

[3] C. P. Morice, J. J. Kennedy, N. A. Rayner, J. P. Winn, E. Hogan, R. E. Killick, R. J. H. Dunn, T. J. Osborn, P. D. Jones, and I. R. Simpson. An updated assessment of near-surface temperature change from 1850: The HadCRUT5 data set. *Journal of Geophysical Research: Atmospheres*, 126(3), 2021.

[4] R. S. Vose, B. Huang, X. Yin, D. Arndt, D. R. Easterling, J. H. Lawrimore, M. J. Menne, A. Sanchez-Lugo, and H. M. Zhang. Implementing full spatial coverage in NOAA's global temperature analysis. *Geophysical Research Letters*, 48(4), 2021.

[5] R. A. Rohde and Z. Hausfather. The berkeley earth land/ocean temperature record. *Earth System Science Data*, 12(4):3469–3479, 2020.

[6] C. Kadow, D. M. Hall, and U. Ulbrich. Artificial intelligence reconstructs missing climate information. *Nature Geoscience*, 13(6), 2020.

[7] W. Sun, Y. Yang, L. Chao, W. Dong, B. Huang, P. Jones, and Q. Li. Description of the china global merged surface temperature version 2.0. *Earth System Science Data*, 14(4):1677–1693, 2022.

[8] K. Matthes, B. Funke, M. E. Andersson, L. Barnard, J. Beer, P. Charbonneau, M. A. Clilverd, T. Dudok de Wit, M. Haberreiter, A. Hendry, C. H. Jackman, M. Kretzschmar, T. Kruschke, M. Kunze, U. Langematz, D. R. Marsh, A. C. Maycock, S. Misios, C. J. Rodger, A. A. Scaife, A. Seppälä, M. Shangguan, M. Sinnhuber, K. Tourpali, I. Usoskin, M. van de Kamp, P. T. Verronen, and S. Versick. Solar forcing for CMIP6 (v3.2). *Geoscientific Model Development*, 10(6):2247–2302, 2017.

[9] J. Hansen, R. Ruedy, M. Sato, and K. Lo. Global surface temperature change. *Reviews of Geophysics*, 48(4), 2010.

[10] N. J. L. Lenssen, G. A. Schmidt, J. E. Hansen, M. J. Menne, A. Persin, R. Ruedy, and D. Zyss. Improvements in the GISTEMP uncertainty model. *Journal of Geophysical Research: Atmospheres*, 124(12):6307–6326, 2019.

[11] J. Ahn, E. J. Brook, A. Schmittner, and K. Kreutz. Abrupt change in atmospheric CO_2 during the last ice age. *Geophysical Research Letters*, 39(18), 2012.

[12] J. Ahn and E. J. Brook. Siple dome ice reveals two modes of millennial CO_2 change during the last ice age. *Nat. Commun.*, 5(3723), 2014.

[13] T.K. Bauska, F. Joos, A.C. Mix, R. Roth, J. Ahn, and E.J. Brook. Links between atmospheric carbon dioxide, the land carbon reservoir and climate over the past millennium. *Nature Geosci.*, 8, 2015.

[14] S. A. Marcott, T. K. Bauska, C. Buizert, E. J. Steig, J. L. Rosen, K. M. Cuffey, T. J. Fudge, J. P. Severinghaus, J. Ahn, M. L. Kalk, J. R. McConnell, T. Sowers, K. C. Taylor, J. W. C. White, and E. J. Brook. Centennial-scale changes in the global carbon cycle during the last deglaciation. *Nature*, 514, 2014.

[15] M. Rubino, D. M. Etheridge, D. P. Thornton, R. Howden, C. E. Allison, R. J. Francey, R. L. Langenfelds, L. P. Steele, C. M. Trudinger, D. A. Spencer, M. A. J. Curran, T. D. van Ommen, and A. M. Smith. Revised records of atmospheric trace gases CO_2, CH_4, N_2O, and δ^{13}c-CO_2 over the last 2000 years from law dome, antarctica. *Earth System Science Data*, 11(2):473–492, 2019.

[16] M. Kageyama, S. Albani, P. Braconnot, S. P. Harrison, P. O. Hopcroft, R. F. Ivanovic, F. Lambert, O. Marti, W. R. Peltier, J.-Y. Peterschmitt, D. M. Roche, L. Tarasov, X. Zhang, E. C. Brady, A. M. Haywood, A. N. LeGrande, D. J. Lunt, N. M. Mahowald, U. Mikolajewicz, K. H. Nisancioglu, B. L. Otto-Bliesner, H. Renssen, R. A. Tomas, Q. Zhang, A. Abe-Ouchi, P. J. Bartlein, J. Cao, Q. Li, G. Lohmann, R. Ohgaito, X. Shi, E. Volodin, K. Yoshida, X. Zhang, and W. Zheng. The PMIP4 contribution to CMIP6 – part 4: Scientific objectives and experimental design of the PMIP4-CMIP6 last glacial maximum experiments and PMIP4 sensitivity experiments. *Geoscientific Model Development*, 10(11):4035–4055, 2017.

[17] L. Mitchell, E. Brook, J. L. Lee, C. Buizert, and T. Sowers. Constraints on the

late holocene anthropogenic contribution to the atmospheric methane budget. *Science*, 342(6161):964–966, 2013.

[18] A. Kao, X. Jiang, L. Li, H. Su, and Y. Yung. Precipitation, circulation, and cloud variability over the past two decades. *Earth and Space Science*, 4(9):597–606, 2017.

[19] C. Liu and R. P. Allan. Observed and simulated precipitation responses in wet and dry regions 1850-2100. *Environmental Research Letters*, 8(034002), 2013.

[20] D. Polson and G. C. Hegerl. Strengthening contrast between precipitation in tropical wet and dry regions. *Geophysical Research Letters*, 44(1):365–373, 2017.

[21] U. Cortesi, J. H. Trammell, X. Jiang, L. Li, M. Liang, M. Li, J. Zhou, E. Fetzer, and Y. Yung. Investigating of precipitation variations over wet and dry areas from observation and model. *Advances in Meteorology*, 2015(981092), 2015.

[22] H. Ellis-Peterson. Dozens dead in mumbai after 'monstrous' monsoon rains cause landslide. `https://www.theguardian.com/world/2021/jul/19/deaths-mumbai-monsoon-rains-landslide-india`, Jul 2021. Online; 02 May 2022.

[23] F. C. Curreiro, J. A. Patz, J. B. Rose, and S. Lele. The association between extreme precipitation and waterborne disease in the united states, 1984-1994. *American Journal of Public Health*, 91(8), 2001.

[24] R. Below, E. Grover-Kopec, and M. Dilley. Documenting drought-related disasters: A global reassessment. *The Journal of Environment & Development*, 16(3):328–344, 2007.

[25] N. H. Ojeh and A. F. Victor-Orivoh. Natural hazards and crop yields in oleh, south-south Nigeria: Flooding in perspective. *J. Earth Sci. Clim. Change*, 5(2):181, 2014.

[26] P. Cias, M. Reichstein, N. Viovy, A. Granier, J. Ogee, V. Allard, M. Aubinet, N. Buchmann, C. Bernhofer, A. Carrara, F. Chevallier, N. De Noblet, A. D. Friend, P. Friedlingstein, T. Grunwald, B. Heinsech, P. Keronen, A. Knohl, G. Krinner, D. Loustau, G. Manca, G. Matteucci, F. Miglietta, J. M. Ourcival, D. Papale, K. Pilegaard, S. Rambal, G. Seufert, J. F. Soussana, M. J. Sanz, E. D. Schulze, T. Vesala, and R. Valentini. Europe-wide reduction in primary productivity caused by the heat and drought in 2003. *Nature*, 437:529–533, 2005.

[27] A. Analitis, I. Georgiadis, and K. Katsouyanni. Forest fires are associated with elevated mortality in a dense urban setting. *Occupational and Environmental Medicine*, 69(3):158–162, 2012.

[28] M. J. B. Zeppel, J. V. Wilks, and J. D. Lewis. Impacts of extreme precipitation and seasonal changes in precipitation on plants. *Biogeosciences*, 11(11):3083–3093, 2014.

[29] A. K. Knapp, C. Beier, D. D. Briske, A. T. Classen, Y. Luo, M. Reichstein, M. D. Smith, S. D. Smith, J. E. Bell, P. A. Fay, J. L. Heisler, S. W. Leavitt, R. Sherry, B. Smith, and E. Weng. Consequences of more extreme precipitation regimes for terrestrial ecosystems. *BioScience*, 58(9):811–821, 2008.

[30] J. A. Foley, G. P. Asner, M. Heil Costa, M. T. Coe, R. DeFries, H. K. Gibbs, E. A. Howard, S. Olson, J. Patz, N. Ramankutty, and P. Snyder. Amazonia revealed: forest degradation and loss of ecosystem goods and services in the amazon basin. *Frontiers in Ecology and the Environment*, 5(1):25–32, 2007.

[31] C. M. Yule. Loss of biodiversity and ecosystems functioning in Indo-Malayan peat swamp forests. *Biodiversity and Conservation*, 19:393–409, 2010.

[32] J. Knies, P. Cabedo-Sanz, S. T. Belt, S. Baranwal, S. Fietz, and A. Rosell-Mele. The emergence of modern sea ice cover in the arctic ocean. *Nature Communications*, 5(5608), 2014.

[33] C. Clotten, R. Stein, K. Fahl, and S. De Schepper. Seasonal sea ice cover during the warm pliocene: Evidence from the Iceland sea (ODP site 907). *Earth and Planetary Science Letters*, 481:61–72, 2018.

[34] R. Feng, B. L. Otto-Bliesner, Y. Xu, E. Brady, T. Fletcher, and A. Ballantyne. Contributions of aerosol-cloud interactions to mid-piacenzian seasonally sea ice-free arctic ocean. *Geophysical Research Letters*, 46(16):9920–9929, 2019.

[35] F. W. Howell, A. M. Haywood, B. L. Otto-Bliesner, F. Bragg, W.-L. Chan, M. A. Chandler, C. Contoux, Y. Kamae, A. Abe-Ouchi, N. A. Rosenbloom, C. Stepanek, and Z. Zhang. Arctic sea ice simulation in the pliomip ensemble. *Climate of the Past*, 12(3):749–767, 2016.

[36] F. Li, M.-J. Gaillard, X. Cao, U. Herzschuh, S. Sugita, P. E. Tarasov, M. Wagner, Q. Xu, J. Ni, W. Wang, Y. Zhao, C. An, A. H. W. Beusen, F. Chen, Z. Feng, C. G. M. Klein Goldewijk, X. Huang, Y. Li, Y. Li, H. Liu, A. Sun,

Y. Yao, Z. Zheng, and X. Jia. Towards quantification of holocene anthropogenic land-cover change in temperate china: A review in the light of pollen-based reveals reconstructions of regional plant cover. *Earth-Science Reviews*, 203:103119, 2020.

[37] A. Spolaor, P. Vallelonga, C. Turetta, N. Maffezzoli, G. Cozzi, J. Gabrieli, C. Barbante, K. Goto-Azuma, A. Saiz-Lopez, C. A. Cuevas, and D. Dahl-Jensen. Canadian Arctic sea ice reconstructed from bromine in the Greenland NEEM ice core. *Scientific reports*, 6(33925), 2016.

[38] O. N. Solomina, R. S. Bradley, D. A. Hodgson, S. Ivy-Ochs, V. Jomelli, A. N. Mackintosh, A. Nesje, L. A. Owen, H. Wanner, G. C. Wiles, and N. E. Young. Holocene glacier fluctuations. *Quaternary Science Reviews*, 111:9–34, 2015.

[39] O. N. Solomina, R. S. Bradley, V. Jomelli, A. Geirsdottir, D. S. Kaufman, J. Koch, N. P. McKay, M. Masiokas, G. Miller, A. Nesje, K. Nicolussi, L. A. Owen, A. E. Putnam, H. Wanner, G. Wiles, and B. Yang. Glacier fluctuations during the past 2000 years. *Quaternary Science Reviews*, 149:61–90, 2016.

[40] S. L. Chown, A. Clarke, C. I. Fraser, S. C. Cary, K. L. Moon, and M. A. McGeoch. The changing form of antarctic biodiversity. *Nature*, 522:431–438, 2015.

[41] P. Convey and M. I. Stevens. Antarctic biodiversity. *Science*, 317(5846):1877–1878, 2007.

[42] B. Bereiter, S. Shackelton, D. Baggenstos, K. Kawamura, and J. Severinghaus. Mean global ocean temperatures during the last glacial transition. *Nature*, 553:39–44, 2018.

[43] S. Shackleton, B. Bereiter, D. Baggenstos, T. K. Bauska, E. J. Brook, S. A. Marcott, and J. P. Severinghaus. Is the noble gas-based rate of ocean warming during the younger dryas overestimated? *Geophysical Research Letters*, 46(11):5928–5936, 2019.

[44] G. C. Johnson and J. M. Lyman. Warming trends increasingly dominate global ocean. *Nature Climate Change*, 10:757–761, 2020.

[45] K. von Schuckmann, L. Cheng, M. D. Palmer, J. Hansen, C. Tassone, V. Aich, S. Adusumilli, H. Beltrami, T. Boyer, F. J. Cuesta-Valero, D. Desbruyères, C. Domingues, A. García-García, P. Gentine, J. Gilson, M. Gorfer, L. Haimberger, M. Ishii, G. C. Johnson, R. Killick, B. A. King, G. Kirchengast,

N. Kolodziejczyk, J. Lyman, B. Marzeion, M. Mayer, M. Monier, D. P. Monselesan, S. Purkey, D. Roemmich, A. Schweiger, S. I. Seneviratne, A. Shepherd, D. A. Slater, A. K. Steiner, F. Straneo, M.-L. Timmermans, and S. E. Wijffels. Heat stored in the earth system: where does the energy go? *Earth System Science Data*, 12(3):2013–2041, 2020.

[46] A. Bagnell and T. DeVries. Correcting biases in historical bathythermograph data using artificial neural networks. *Journal of Atmospheric and Oceanic Technology*, 37(10), 2020.

[47] L. Cheng, K. E. Trenberth, N. Gruber, J. P. Abraham, J. T. Fasullo, G. Li, M. E. Mann, X. Zhao, and J. Zhu. Improved estimates of changes in upper ocean salinity and the hydrological cycle. *Journal of Climate*, 33(23), 2020.

[48] V. Gouretski, J. Kennedy, T. Boyer, and A. Köhl. Consistent near-surface ocean warming since 1900 in two largely independent observing networks. *Geophysical Research Letters*, 39(19), 2012.

[49] T. P. Leahy, F. P. Llopis, M. D. Palmer, and N. H. Robinson. Using neural networks to correct historical climate observations. *Journal of Atmospheric and Oceanic Technology*, 35(10), 2018.

[50] M. D. Palmer, T. Boyer, R. Cowley, S. Kizu, F. Reseghetti, T. Suzuki, and A. Thresher. An algorithm for classifying unknown expendable bathythermograph (XBT) instruments based on existing metadata. *Journal of Atmospheric and Oceanic Technology*, 35(3):429–440, 2018.

[51] M. D. Palmer, C. M. Domingues, A. B. A. Slangen, and F. Boeira Dias. An esnemble approach to quantify global mean sea-level rise over the 20th century from the tide gauge reconstructions. *Environmental Research Letters*, 16(4), 2021.

[52] M. Ablain, B. Meyssignac, L. Zawadzki, R. Jugier, A. Ribes, G. Spada, J. Benveniste, A. Cazenave, and N. Picot. Uncertainty in satellite estimates of global mean sea-level changes, trend and acceleration. *Earth System Science Data*, 11(3):1189–1202, 2019.

[53] X. Chen, X. Zhang, J. A. Church, C. S. Watson, M. A. King, D. Monselesan, B. Legresy, and C. Harig. The increasing rate of global mean sea-level rise during 1993-2014. *Nature Climate Change*, 7:492–495, 2017.

[54] C. S. Watson, N. J. White, J. A. Church, M. A. King, R. J. Burgette, and B. Legresy. Unabated global mean sea-level rise over the satellite altimeter era. *Nature Climate Change*, 5:565–568, 2015.

[55] R. S. Nerem, B. D. Beckley, J. T. Fasullo, B. D. Hamlington, D. Masters, and G. T. Mitchum. Climate-change-driven accelerated sea-level rise detected in the altimeter era. *Proceedings of the National Academy of Sciences*, 115(9):2022–2025, 2018.

[56] Hurd C. L., A. Lenton, B. Tilbrook, and P. W. Boyd. Current understanding and challenges for oceans in a higher-CO_2 world. *Nature Climate Change*, 8:686–694, 2018.

[57] S. K. Lauvset, N. Gruber, P. Landschützer, A. Olsen, and J. Tjiputra. Trends and drivers in global surface ocean pH over the past 3 decades. *Biogeosciences*, 12(5):1285–1298, 2015.

[58] D. C. E. Bakker, B. Pfeil, C. S. Landa, N. Metzl, K. M. O'Brien, A. Olsen, K. Smith, C. Cosca, S. Harasawa, S. D. Jones, S. Nakaoka, Y. Nojiri, U. Schuster, T. Steinhoff, C. Sweeney, T. Takahashi, B. Tilbrook, C. Wada, R. Wanninkhof, S. R. Alin, C. F. Balestrini, L. Barbero, N. R. Bates, A. A. Bianchi, F. Bonou, J. Boutin, Y. Bozec, E. F. Burger, W.-J. Cai, R. D. Castle, L. Chen, M. Chierici, K. Currie, W. Evans, C. Featherstone, R. A. Feely, A. Fransson, C. Goyet, N. Greenwood, L. Gregor, S. Hankin, N. J. Hardman-Mountford, J. Harlay, J. Hauck, M. Hoppema, M. P. Humphreys, C. W. Hunt, B. Huss, J. S. P. Ibánhez, T. Johannessen, R. Keeling, V. Kitidis, A. Körtzinger, A. Kozyr, E. Krasakopoulou, A. Kuwata, P. Landschützer, S. K. Lauvset, N. Lefèvre, C. Lo Monaco, A. Manke, J. T. Mathis, L. Merlivat, F. J. Millero, P. M. S. Monteiro, D. R. Munro, A. Murata, T. Newberger, A. M. Omar, T. Ono, K. Paterson, D. Pearce, D. Pierrot, L. L. Robbins, S. Saito, J. Salisbury, R. Schlitzer, B. Schneider, R. Schweitzer, R. Sieger, I. Skjelvan, K. F. Sullivan, S. C. Sutherland, A. J. Sutton, K. Tadokoro, M. Telszewski, M. Tuma, S. M. A. C. van Heuven, D. Vandemark, B. Ward, A. J. Watson, and S. Xu. A multi-decade record of high-quality fCO_2 data in version 3 of the surface ocean CO_2 atlas (SOCAT). *Earth System Science Data*, 8(2):383–413, 2016.

[59] L. Gregor and N. Gruber. OceanSODA-ETHZ: a global gridded data set of the surface ocean carbonate system for seasonal to decadal studies of ocean acidification. *Earth System Science Data*, 13(2):777–808, 2021.

[60] B. Talukder, N. Ganguli, R. Matthew, G. W. vanLoon, K. W. Hipel, and J. Orbinski. Climate change-accelerated ocean biodiversity loss & associated planetary health impacts. *The Journal of Climate Change and Health*, 6:100114, 2022.

[61] B. Worm, E. B. Barbier, N. Beaumont, J. E. Duffy, C. Folke, B. S. Halpern, J. B. C. Jackson, H. K. Lotze, F. Micheli, S. R. Palumbi, E. Sala, K. A. Selkoe, J. J. Stachowicz, and R. Watson. Impacts of biodiversity loss on ocean ecosystem services. *Science*, 314(5800):787–790, 2006.

[62] S. Murawski, R. Methot, and G. Tromble. Biodiversity loss in the ocean: How bad is it? *Science*, 316(5829):1281–1284, 2007.

[63] IEA. Greenhouse gas emissions from energy data explorer - analysis. `https://www.iea.org/articles/greenhouse-gas-emissions-from-energy-data-explorer`. Online; accessed 05 May 2022.

[64] Shell International B.V. The energy transformation scenarios. Technical report, Shell International B.V., 2021.

[65] British Petroleum Company. Bp statistical review of world energy version 70. Technical report, British Petroleum Company, 2021.

[66] T. Wilberforce, A. G. Olabi, E. T. Sayed, K. Elsaid, and M. A. Abdelkareem. Progress in carbon capture technologies. *Science of The Total Environment*, 761:143203, 2021.

[67] C. B. Agaton. Application of real options in carbon capture and storage literature: Valuation techniques and research hotspots. *Science of The Total Environment*, 795:148683, 2021.

[68] Drax. Drax commences major turbine upgrade to drive down cost of biomass power generation. `https://www.drax.com/press_release/drax-commences-major-turbine-upgrade-to-drive-down-cost-of/`, Aug 2021. Online; Accessed 04 May 2022.

[69] G. Zanchi, N. Pena, and N. Bird. Is woody bioenergy carbon neutral? A comparative assessment of emissions from consumption of woody bioenergy and fossil fuel. *GCB Bioenergy*, 4(6):761–772, 2012.

[70] P. Vanhala, A. Repo, and J. Liski. Forest bioenergy at the cost of carbon sequestration? *Current Opinion in Environmental Sustainability*, 5(1):41–46, 2013.

[71] R. Sedjo and X. Tian. Does Wood Bioenergy Increase Carbon Stocks in Forests? *Journal of Forestry*, 110(6):304–311, 2012.

[72] G. M. Souza, M. V. R. Ballester, C. H. de Brito Cruz, H. Chum, B. Dale, V. H. Dale, E. C. M. Fernandes, T. Foust, A. Karp, L. Lynd, R. Maciel Filho, A. Milanez, F. Nigro, P. Osseweijer, L. M. Verdade, R. L. Victoria, and L. Van der Wielen. The role of bioenergy in a climate-changing world. *Environmental Development*, 23:57–64, 2017.

[73] J. Popp, Z. Lakner, M. Harangi-Rákos, and M. Fári. The effect of bioenergy expansion: Food, energy, and environment. *Renewable and Sustainable Energy Reviews*, 32:559–578, 2014.

[74] T. Weiss. Uniformity or polarization? The nuclear power debate in Japanese newspapers and political coalitions, 1973–2014. *Contemporary Japan*, 33(1):57–122, 2021.

[75] E. Gisquet. Tragic choices at Fukushima Daiichi nuclear power plant. *Natural Hazards Review*, 22(3), 2021.

[76] R. Braithwaite. Chernobyl: A 'normal' accident? *Survival*, 61(5):149–158, 2019.

[77] J. Vujić, D. P. Antić, and Z. Vukmirović. Environmental impact and cost analysis of coal versus nuclear power: The U.S. case. *Energy*, 45(1):31–42, 2012.

[78] Working Group III. Apendix III in climate change 2014: Mitigation of climate change. Technical report, Intergorvernmental Panel on Climate Change, 2014.

[79] J. M. Pearce. Limitations of nuclear power as a sustainable energy source. *Sustainability*, 4(6):1173–1187, 2012.

[80] M. V. Ramana. Technical and social problems of nuclear waste. *WIREs Energy and Environment*, 7(4), 2018.

[81] D. Bosbach, F. Brandt, A. Bukaemskiy, G. Deissmann, P. Kegler, M. Klinkenberg, P. M. Kowalski, G. Modolo, I. Niemeyer, S. Neumeier, and V. Vinograd. Research for the safe management of nuclear waste at forschungszentrum jülich: Materials chemistry and solid solution aspects. *Advanced Engineering Materials*, 22(6), 2020.

[82] World Nuclear Association. Storage and disposal of radioactive waste. `https://world-nuclear.org/information-library/nuclear-fuel-cycle/nuclear-waste/storage-and-disposal-of-radioactive-waste.aspx`, May 2021. Online; accessed 02 May 2022.

[83] International Atomic Energy Agency. World statistics. https://pris.iaea.org/PRIS/WorldStatistics/OperationalReactorsByCountry.aspx, Apr 2022. Online; accesed 04 May 2022.

[84] S. Raikar and S. Adamson. 13 - renewable energy finance in the international context. In Santosh Raikar and Seabron Adamson, editors, *Renewable Energy Finance*, pages 185–220. Academic Press, 2020.

[85] Hinkley point 'will cost public double the amount it should'. https://www.theweek.co.uk/60778/hinkley-point-will-cost-public-double-the-amount-it-should, Jun 2017. Online; accessed 02 May 2022.

[86] A. Vaughan. Brexit will delay new british nuclear power stations, warn experts. https://www.theguardian.com/business/2017/jan/27/uk-exit-eu-atomic-treaty-brexit-euratom-hinkley-point-c, Jan 2017. Online; accessed 03 May 2022.

[87] J. I. Pérez-Díaz, M. Chazarra, J. García-González, G. Cavazzini, and A. Stoppato. Trends and challenges in the operation of pumped-storage hydropower plants. *Renewable and Sustainable Energy Reviews*, 44:767–784, 2015.

[88] B. Xu, D. Chen, M. Venkateshkumar, Y. Xiao, Y. Yue, Y. Xing, and P. Li. Modeling a pumped storage hydropower integrated to a hybrid power system with solar-wind power and its stability analysis. *Applied Energy*, 248:446–462, 2019.

[89] W.-L. Liao, D. S. Bhargava, and J. Das. Some effects of dams on wildlife. *Environmental Conservation*, 15(1):68–70, 1988.

[90] J. A. McNeely. How dams and wildlife can coexist: Natural habitats, agriculture, and major water resource development projects in tropical asia. *Conservation Biology*, 1(3):228–238, 1987.

[91] N. Uddin and K. Uddin. Hydropower dams, environment and politics. *Journal of International Affairs*, 2(1), 2018.

[92] P. M. Fearnside. Environmental and social impacts of hydroelectric dams in Brazilian Amazonia: Implications for the aluminum industry. *World Development*, 77:48–65, 2016.

[93] D. Égré and P. Senécal. Social impact assessments of large dams throughout the world: lessons learned over two decades. *Impact Assessment and Project Appraisal*, 21(3):215–224, 2003.

[94] J. Kirchherr and K. J. Charles. The social impacts of dams: A new framework for scholarly analysis. *Environmental Impact Assessment Review*, 60:99–114, 2016.

[95] R. K. Paisley. International watercourses, international water law and central asia. *Central Asian Journal of Water Research*, 4(2):1–26, 2019.

[96] T. Meshel. Swinning against the current: Revisiting the principles of international water law in the resolution of fresh water disputes. *Harvard International Law Journal*, 61(184), 2020.

[97] Peter H. Gleick. Water and conflict: Fresh water resources and international security. *International Security*, 18(1):79–112, 1993.

[98] S. Milne. How water shortages are brewing wars, Aug 2021. Online; accessed 04 May 2022.

[99] J. R. Starr. Water wars. *Foreign Policy*, 82:17–36, 1991.

[100] R. M. Almeida, Q. Shi, J. M. Gomes-Selman, X. Wu, Y. Xue, H. Angarita, N. Barros, B. R. Forsberg, R. Garcia-Villacorta, S. K. Hamilton, J. M. Melack, M. Montoya, G. Perez, S. A. Sethi, C. P. Gomes, and A. S. Flecker. Reducing greenhouse gas emissions of amazon hydropower with strategic dam planning. *Nature Communications*, 10(4281), 2019.

[101] J. A. Harrison, Y. T. Prairie, S. Mercier-Blais, and C. Soued. Year-2020 global distribution and pathways of reservoir methane and carbon dioxide emissions according to the greenhouse gas from reservoirs (g-res) model. *Global Biogeochemical Cycles*, 35(6), 2021.

[102] E. Barbier. Geothermal energy technology and current status: an overview. *Renewable and Sustainable Energy Reviews*, 6(1):3–65, 2002.

[103] J. F. Kunze. Utilizing geothermal resources below 150°c (300°f). *J. Energy Resour. Technol.*, 101(2):124–127, 1979.

[104] I. Stober and K. Bucher. *Uses of Geothermal Energy*, pages 43–79. Springer International Publishing, 2021.

[105] L. Xia and Y. Zhang. An overview of world geothermal power generation and a case study on China-the resource and market perspective. *Renewable and Sustainable Energy Reviews*, 112:411–423, 2019.

[106] J. Busby and R. Terrington. Assessment of the resource base for engineered geothermal systems in Great Britain. *Geothermal Energy*, 5(1), 2017.

[107] J. Busby. Geothermal energy in sedimentary basins in the UK. *Hydrogeology Journal*, 22(1), 2014.

[108] D. Giardini. Geothermal quake risks must be faced. *Nature*, 462, 2009.

[109] W. L. Ellsworth. Injection-induced earthquakes. *Science*, 341(6142), 2013.

[110] A. J. Brand, J. Peinke, and J. Mann. Turbulence and wind turbines. *Journal of Physics: Conference Series*, 318(7), 2011.

[111] B. J. Rygg. Wind power—an assault on local landscapes or an opportunity for modernization? *Energy Policy*, 48:167–175, 2012.

[112] S. Wang and S. Wang. Impacts of wind energy on environment: A review. *Renewable and Sustainable Energy Reviews*, 49:437–443, 2015.

[113] C. T. Thien, H. N. Quoc, A. T. Nguyen, and M. Tran. *Analysis and prediction of noise pollution from wind turbines: A case study of Loi Hai wind power plant (Ninh Thuan, Vietnam)*, pages 805–816. Springer International Publishing, 2022.

[114] N. E. Chowdhury, M. A. Shakib, F. Xu, S. Salehin, M. Rashidul Islam, and A. A. Bhuiyan. Adverse environmental impacts of wind farm installations and alternative research pathways to their mitigation. *Cleaner Engineering and Technology*, 7, 2022.

[115] K. S. Smallwood, L. Rugge, and M. L. Morrison. Influence of behavior on bird mortality in wind energy developments. *The Journal of Wildlife Management*, 73(7):1082–1098, 2009.

[116] K. S. Smallwood. Comparing bird and bat fatality-rate estimates among north american wind-energy projects. *Wildlife Society Bulletin*, 37(1):19–33, 2013.

[117] T. R. Ayodele and A. S. O. Ogunjuyigbe. Mitigation of wind power intermittency: Storage technology approach. *Renewable and Sustainable Energy Reviews*, 44:447–456, 2015.

[118] K. De Vos and J. Driesen. Balancing management mechanisms for intermittent power sources - a case study for wind power in Belgium. In *2009 6th International Conference on the European Energy Market*, pages 1–6, 2009.

[119] A. Soroudi, B. Mohammadi-Ivatloo, and A. Rabiee. *Energy Hub Management with Intermittent Wind Power*, pages 413–438. Springer Singapore, 2014.

[120] M. Jabir, H. Azil Illias, S. Raza, and H. Mokhlis. Intermittent smoothing approaches for wind power output: A review. *Energies*, 10(10):1572, 2017.

[121] Energy & Industrial Strategy Department for Business. Energy trends: UK renewables. `https://www.gov.uk/government/statistics/energy-trends-section-6-renewables`. Online; accessed 13 June 2022.

[122] J. C. Goldschmidt, L. Wagner, R. Pietzcker, and L. Friedrich. Technological learning for resource efficient terawatt scale photovoltaics. *Energy Environ. Sci.*, 14:5147–5160, 2021.

[123] M. Ram, D. Bogdanov, A. Aghahosseini, A. Gulagi, S. A. Oyewo, M. Child, U. Caldera, K. Sadocskaia, J. Farfan, L. S. N. S. Barbosa, M. Fasihi, S. Khalili, C. Breyer, and H.-J. Fell. Global energy system based on 100% renewable energy - power, heat, transport and desalination. Technical report, Lappeenranta University of Technology and Energy Watch Group, 2019.

[124] D. Cahen and A. Kahn. Electron energetics at surfaces and interfaces: Concepts and experiments. *Advanced Materials*, 15(4):271–277, 2003.

[125] C. R. M. Grovenor. *Microelectronic Materials*. CRC Press, 1989.

[126] C. Cavallotti, F. Rossi, S. Ravasio, and M. Masi. A kinetic analysis of the growth and doping kinetics of the sic chemical vapor deposition process. *Industrial & Engineering Chemistry Research*, 53(22):9076–9087, 2014.

[127] L. Thomas, T. D. C. Hobson, L. J. Phillips, K. J. Cheetham, N. Tarbuck, L. A. H. Jones, M. J. Smiles, C. H. Don, P. K. Thakur, M. Isaacs, H. Shiel, S. Campbell, V. Barrioz, V. Dhanak, T. D. Veal, J. D. Major, and K. Durose. Insights into post-growth doping and proposals for cdte:in photovoltaic devices. *Journal of Physics: Energy*, 4(4):045001, 2022.

[128] W. Shockley and H. J. Queisser. Detailed balance limit of efficiency of p-n junction solar cells. *Journal of Applied Physics*, 32(3):510–519, 1961.

[129] S. Rühle. Tabulated values of the shockley-queisser limit for single junction solar cells. *Solar Energy*, 130:139–147, 2016.

[130] S. K. Wallace, K. T. Butler, Y. Hinuma, and A. Walsh. Finding a junction partner for candidate solar cell absorbers enargite and bournonite from electronic band and lattice matching. *Journal of Applied Physics*, 125(5):055703, 2019.

[131] J. M. Kephart, J. W. McCamy, Z. Ma, A. Ganjoo, F. M. Alamgir, and W. S. Sampath. Band alignment of front contact layers for high-efficiency cdte solar cells. *Solar Energy Materials and Solar Cells*, 157:266–275, 2016.

[132] C. Ding, Y. Zhang, F. Liu, Y. Kitabatake, S. Hayase, T. Toyoda, K. Yoshino, T. Minemoto, K. Katayama, and Q. Shen. Effect of the conduction band offset on interfacial recombination behavior of the planar perovskite solar cells. *Nano Energy*, 53:17–26, 2018.

[133] H. Shiel, O. S. Hutter, L. J. Phillips, J. E. N. Swallow, L. A. H. Jones, T. J. Featherstone, M. J. Smiles, P. K. Thakur, T.-L. Lee, V. R. Dhanak, J. D. Major, and T. D. Veal. Natural band alignments and band offsets of Sb_2Se_3 solar cells. *ACS Applied Energy Materials*, 3(12):11617–11626, 2020.

[134] E. Becquerel. *La Lumiere, SES causes et ses effects*. Firmin Didot fr'eres, 1867.

[135] W. Smith. Effect of light on selenium during the passage of an electric current. *Nature*, 7(303), 1873.

[136] W. G. Adams and R. E. Day. V. the action of light on selenium. *Proceedings of the Royal Society of London*, 25(171-178):113–117, 1877.

[137] J. Perlin and M. Z. Jacobson. *Let it shine: The 6,000-year story of Solar Energy*. New World Library, 2022.

[138] D. M. Chapin, C. S. Fuller, and G. L. Pearson. A new silicon p-n junction photocell for converting solar radiation into electrical power. *Journal of Applied Physics*, 25(5):676–677, 1954.

[139] K. Yoshikawa, H. Kawasaki, W. Yoshida, T. Irie, K. Konishi, K. Nakano, T. Uto, D. Adachi, M. Kanematsu, H. Uzu, and K. Yamamoto. Silicon heterojunction solar cell with interdigitated back contacts for a photoconversion efficiency over 26%. *Nature Energy*, 2(17032), 2017.

[140] M. A. Green, E. D. Dunlop, J. Hohl-Ebinger, M. Yoshita, N. Kopidakis, and X. Hao. Solar cell efficiency tables (version 56). *Progress in Photovoltaics: Research and Applications*, 28(7):629–638, 2020.

[141] G. J. Hayes and B. M. Clemens. Laser liftoff of gallium arsenide thin films. *MRS Communications*, 5(1):1–5, 2015.

[142] A. De Vos. Detailed balance limit of the efficiency of tandem solar cells. *Journal of Physics D: Applied Physics*, 13(5):839–846, 1980.

[143] R. M. France, J. F. Geisz, T. Song, W. Olavarria, M. Young, A. Kibbler, and M. A. Steiner. Triple-junction solar cells with 39.5% terrestrial and 34.2% space efficiency enabled by thick quantum well superlattices. *Joule*, 6(5):1121–1135, 2022.

[144] J. F. Geisz, R. M. France, K. L. Schulte, M. A. Steiner, A. G. Norman, H. L. Guthrey, M. R. Young, T. Song, and T. Moriaty. Six-junction III-V solar cells with 47.1% conversion efficiency under 143 suns concentration. *Nature Energy*, 5:326–335, 2020.

[145] R. Xue, J. Zhang, Y. Li, and Y. Li. Organic solar cell materials toward commercialization. *Small*, 14(1801793), 2018.

[146] L. Wang, C. Guo, X. Zhang, S. Cheng, D. Li, J. Cai, C. Chen, Y. Fu, J. Zhou, H. Qin, D. Liu, and T. Wang. Alkyl chain tuning of non-fullerene electron acceptors toward 18.2% efficiency binary organic solar cells. *Chemistry of Materials*, 33(22):8854–8862, 2021.

[147] A. Kojima, K. Teshima, Y. Shirai, and T. Miyasaka. Organometal halide perovskites as visible-light sensitizers for photovoltaic cells. *Journal of the American Chemical Society*, 131(17):6050–6051, 2009.

[148] H. Min, D. Y. Lee, J. Kim, G. Kim, K. S. Lee, J. Kim, M. J. Paik, Y. K. Kim, K. S. Kim, M. G. Kim, T. J. Shin, and S. Il Seok. Perovskite solar cells with atomically coherent interlayers on sno$_2$ electrodes. *Nature*, 598(7881):444–450, 2021.

[149] A. M. Ganose, C. N. Savory, and D. O. Scanlon. Beyond methylammonium lead iodide: prospects for the emergent field of ns^2 containing solar absorbers. *Chem. Commun.*, 53:20–44, 2017.

[150] L. E. Orgel. 769. the stereochemistry of b subgroup metals. part ii. the inert pair. *J. Chem. Soc.*, pages 3815–3819, 1959.

[151] J.D. Dunitz and L.E. Orgel. *Stereochemistry of Ionic Solids*, volume 2 of *Advances in Inorganic Chemistry and Radiochemistry*, pages 1–60. Academic Press, 1960.

[152] A. Walsh, D. J. Payne, R. G. Egdell, and G. W. Watson. Stereochemistry of post-transition metal oxides: revision of the classical lone pair model. *Chem. Soc. Rev.*, 40:4455–4463, 2011.

[153] R. E. Brandt, V. Stevanović, D. S. Ginley, and T. Buonassisi. Identifying defect-tolerant semiconductors with high minority-carrier lifetimes: beyond hybrid lead halide perovskites. *MRS Communications*, 5:275, 2015.

[154] Q. Fu, X. Tang, B. Huang, T. Hu, L. Tan, L. Chen, and Y. Chen. Recent progress on the long-term stability of perovskite solar cells. *Advanced Science*, 5(5):1700387, 2018.

[155] C. Candelise, M. Winskel, and R. Gross. Implications for CdTe and CIGS technologies production costs of indium and tellurium scarcity. *Prog. Photovoltaics*, 20:816–831, 2012.

[156] S. Battersby. The solar cell of the future. *Proc. Nat. Acad. Sci.*, 116:7–10, 2019.

[157] K. Momma and F. Izumi. Vesta 3 for three-dimensional visualization of crystal, volumetric and morphology data. *J. Appl. Crystallogr.*, 44:1272–1276, 2011.

[158] G. W. C. Kaye, T. H. Laby, John G. Noyes, G. F. Phillips, O. Jones, and Jim Asher. Tables of physical & chemical constants (16th edition, 1995). section 3.1.3 abundances of the elements. kaye & laby online. version 1.0 (2005). `https://web.archive.org/web/20190518224615/http://www.kayelaby.npl.co.uk/chemistry/3_1/3_1_3.html` (accessed Feb 11, 2021).

[159] C. H. Don, H. Shiel, T. D. C. Hobson, C. N. Savory, J. E. N. Swallow, M. J. Smiles, L. A. H. Jones, T. J. Featherstone, P. K. Thakur, T.-L. Lee, K. Durose, J. D. Major, V. R. Dhanak, D. O. Scanlon, and T. D. Veal. Sb $5s^2$ lone pairs and band alignment of Sb_2Se_3: a photoemission and density functional theory study. *J. Mater. Chem. C*, 8:12615–12622, 2020.

[160] A. Zakutayev, J. D. Major, X. Hao, A. Walsh, J. Tang, T. K. Todorov, L. H. Wong, and E. Saucedo. Emerging inorganic solar cell efficiency tables (version 2). *Journal of Physics: Energy*, 3(3):032003, 2021.

[161] T. D. C. Hobson and K. Durose. Protocols for the miller indexing of Sb_2Se_3 and a non-x-ray method of orienting its single crystals. *Materials Science in Semiconductor Processing*, 127:105691, 2021.

[162] Y. Zhou, L. Wang, S. Chen, S. Qin, X. Liu, J. Chen, D.-J. Xue, M. Luo, Y. Cao, Y. Cheng, E. H. Sargent, and J. Tang. Thin-film Sb_2Se_3 photovoltaics with oriented one-dimensional ribbons and benign grain boundaries. *Nature Photonics*, 9:409–415, 2015.

[163] X. Wang, Z. Li, S. R. Kavanagh, A. M. Ganose, and A. Walsh. Lone pair driven anisotropy in antimony chalcogenide semiconductors. *Phys. Chem. Chem. Phys.*, 24:7195–7202, 2022.

[164] L. Wang, D. B. Li, K. Li, C. Chen, H. X. Deng, L. Gao, Y. Zhao, F. Jiang, L. Li, F. Huang, Y. He, H. Song, G. Niu, and J. Tang. Stable 6%-efficient Sb_2Se_3 solar cells with a ZnO buffer layer. *Nature Energy*, 2:17046, 2017.

[165] W. H. Zachariasen. The crystal lattice of germano sulphide, GeS. *Phys. Rev.*, 40:917–922, Jun 1932.

[166] A. Okazaki. The crystal structure of germanium selenide GeSe. *Journal of Physical Society of Japan*, 13(10):1151–1155, 1958.

[167] S.-C. Liu, C.-M. Dai, Y. Min, Y. Hou, A. H. Proppe, Y. Zhou, C. Chen, S. Chen, J. Tang, and D.-J. Xue. An antibonding valence band maximum enables defect-tolerant and stable GeSe photovoltaics. *Nature Communications*, 12(1):670, 2021.

[168] T. Baines, L. Bowen, B. G. Mendis, and J. D. Major. Microscopic analysis of interdiffusion and void formation in CdTe(1-x)Sex and CdTe layers. *ACS Applied Materials & Interfaces*, 12(34):38070–38075, 2020.

[169] L. J. Phillips, C. N. Savory, O. S. Hutter, P. J. Yates, H. Shiel, S. Mariotti, L. Bowen, M. Birkett, K. Durose, D. O. Scanlon, and J. D. Major. Current enhancement via a TiO_2 window layer for CSS Sb_2Se_3 solar cells: Performance limits and high V_{oc}. *IEEE Journal of Photovoltaics*, 9(2):544–551, 2019.

[170] J. D. Major, L. J. Phillips, M. Al Turkestani, L. Bowen, T. J. Whittles, V. R. Dhanak, and K. Durose. P3HT as a pinhole blocking back contact for CdTe thin film solar cells. *Solar Energy Materials and Solar Cells*, 172:1–10, 2017.

[171] W. Friedrich, P. Knipping, and M. Laue. Interferenz-erscheinungen bei röntgenstrahlen. *Bayerische Akad d. Wiss. zu München, Sitzunger, math.-phys. Kl.*, 2(336), 1912.

[172] W. H. Bragg and W. L. Bragg. The reflection of X-rays by crystals. *Proc. R. Soc. Lond. A.*, 88(1), 1913.

[173] C. F. Holder and R. E. Schaak. Tutorial on powder x-ray diffraction for characterizing nanoscale materials. *ACS Nano*, 13(7):7359–7365, 2019.

[174] G.B. Harris. X. quantitative measurement of preferred orientation in rolled uranium bars. *The London, Edinburgh, and Dublin Philosophical Magazine and Journal of Science*, 43(336):113–123, 1952.

[175] T.-L. Lee and D. A. Duncan. A two-color beamline for electron spectroscopies at Diamond Light Source. *Synchrotron Radiation News*, 31(4):16–22, 2018.

[176] J. F. Moulder and J. Chastain. *Handbook of X-ray Photoelectron Spectroscopy: A Reference Book of Standard Spectra for Identification and Interpretation of XPS Data*. Physical Electronics Division, Perkin-Elmer Corporation, 1992.

[177] A. Proctor and P. M. A. Sherwood. Data analysis techniques in x-ray photoelectron spectroscopy. *Analytical Chemistry*, 54(1):13–19, 1982.

[178] J. Végh. The shirley background revised. *Journal of Electron Spectroscopy and Related Phenomena*, 151(3):159–164, 2006.

[179] S. Tanuma, C. Powell, and D. Penn. Calculation of electron inelastic mean free paths (IMFPs) VII. reliability of the TPP-2M IMFP predictive equation. *Surface and Interface Analysis*, 35:268 – 275, 2003.

[180] J. H. Scofield. Theoretical photoionization cross sections from 1 to 1500 kev. *Technical Report URCL - 51326*, 1973.

[181] P. Day. *Electronic Structure and Magnetism of Inorganic Compounds*, volume 3. Royal Society of Chemistry, 2007.

[182] L. A. H. Jones, W. M. Linhart, N. Fleck, J. E. N. Swallow, P. A. E. Murgatroyd, H. Shiel, T. J. Featherstone, M. J. Smiles, P. K. Thakur, T. L. Lee, L. J. Hardwick, J. Alaria, F. Jäckel, R. Kudrawiec, L. A. Burton, A. Walsh, J. M. Skelton, T. D. Veal, and V. R. Dhanak. Sn $5s^2$ lone pairs and the electronic structure of tin sulphides: A photoreflectance, high-energy photoemission, and theoretical investigation. *Phys. Rev. Materials*, 4:074602, 2020.

[183] D. J. Payne, R. G. Egdell, D. S. L. Law, P-A Glans, T Learmonth, K. E. Smith, J. Guo, A. Walsh, and G. W. Watson. Experimental and theoretical study of the electronic structures of α-PbO and β-PbO_2. *J. Mater. Chem.*, 17:267–277, 2007.

[184] M. Born and R. Oppenheimer. Zur quantentheorie der molekeln. *Annalen der Physik*, 389(20), 1927.

[185] P. Hohenberg and W. Kohn. Inhomogeneous electron gas. *Phys. Rev.*, 136:B864–B871, 1964.

[186] J. Perdew, K. Burke, and M. Ernzerhof. Generalized Gradient Approximation Made Simple. *Phys. Rev. Lett.*, 77(18):3865–3868, 1996.

[187] J. Heyd, G. E. Scuseria, and M. Ernzerhof. Hybrid functionals based on a screened Coulomb potential. *J. Chem. Phys.*, 118(18):8207–8215, 2003.

[188] S. Grimme. Accurate description of van der Waals complexes by density functional theory including empirical corrections. *J. Comp. Chem.*, 25:1463–1473, 2004.

[189] Bruker. *A 510/Q-T User Instructions.*

[190] J. Hllibrand and R. D. Gold. *Determination of the impurity distribution in junction diodes from capacitance-voltage measurements*, pages 191–198. World Scientific, 1991.

[191] M. Cristea. Capacitance-voltage profiling techniques for characterization of semiconductor materials and devices. *Emerging Trends in Electrical, Electronics & Instrumentation Engineering*, 1:3, 2010.

[192] N. C. Marcheva. Physikalisch-chemische eigenschaften der halbleiter im system ges_x se_{1-x}. *Monatshefte für Chemie*, 110:35–38, 1979.

[193] G. K. Solanki, D. B. Patel, S. Unadkat, T. Patel, and N. N. Gosai. Structural characterization of $ges_{0.5}se_{0.5}$ crystals grown by vapour transport technique. *Chalcogenide Letters*, 6:257–263, 2009.

[194] G. K. Solanki, D. B. Patel, S. Unadkat, and M. K. Agarwal. Synthesis and characterization of germanium monosulphide (ges) single crystals grown using different transporting agents. *Pramana*, 74:813–825, 2010.

[195] G. K. Solanki, D. B. Patel, S. Unadkat, N. N. Gosai, and Y. G. Mansur. Growth, structural and high pressure study of $ges_{0.25}se_{0.75}$ and $ges_{0.75}se_{0.25}$ single crystals. *Advanced Materials Research*, 665:37–42, 4 2013.

[196] S. Unadkat and R. Patel. Synthesis and characterizations of $ges_{0.5}se_{0.5}$ (i_2) single crystals. *Research & Reviews: A Journal of Embedded System & Applications*, 7:10–16, 01 2019.

[197] H. S. Im, Y. Myung, K. Park, C. S. Jung, Y. R. Lim, D. M. Jang, and J. Park. Ternary alloy nanocrystals of tin and germanium chalcogenides. *RSC Advances*, 4:15695–15701, 2014.

[198] A. M. Elkorashy. Indirect forbidden fundamental absorption edge in germanium selenide single crystals. *Phys. Stat. Sol. (b)*, 135:707–713, 1986.

[199] A. M. Elkorashy. Photoconductivity in germanium selenide single crystals. *Phys. Stat. Sol. (b)*, 152:249–259, 1989.

[200] S. V. Vlachos, A. P. Lambros, A. Thanailakis, and N. A. Economou. Anisotropic indirect absorption edge in gese. *Phys. Stat. Sol. (b)*, 76:727–735, 1976.

[201] Y. Kim and I. Choi. Optical and electrical properties of gese and snse single crystals. *J. Korean Phys. Soc.*, 72(2):238–242, 2018.

[202] D. D. Vaughn, D. Sun, S. M. Levin, A. J. Biacchi, T. S. Mayer, and R. E. Schaak. Colloidal synthesis and electrical properties of gese nanobelts. *Chem. Mater.*, 24:3643–3649, 2012.

[203] F. Lukeš. Optical and photoelectric properties of gese in the energy range 0.5-1.5ev. *Czechoslovak J. Phys. B*, 18:784–794, 1968.

[204] D. D. Vaughn, R. J. Patel, M. A. Hickner, and R. E. Schaak. Single-crystal colloidal nanosheets of GeS and GeSe. *J. Am. Chem. Soc.*, 132(43):15170–15172, 2010.

[205] S.-C. Liu, Y. Mi, D.-J. Xue, Y.-X. Chen, C. He, X. Liu, J.-S. Hu, and L.-J. Wan. Investigation of physical and electronic properties of GeSe for photovoltaic applications. *Advanced Electronic Materials*, 3:1700141:1–7, 2017.

[206] V. R. Katti, P. A. Govindacharyulu, and D. N. Bose. Electrical and optical properties of amorphous semiconducting GeSe and GeSbSe films. *Thin Solid Films*, 14:143–148, 1972.

[207] C. R. Kannewurf and R. J. Cashman. Optical absorption and photoconductivity in germanium selenide. *J. Phys. Chem. Solids*, 22:293–298, 1961.

[208] P. Mishra, H. Lohani, A. K. Kundu, R. Patel, G. K. Solanki, K. S. R. Menon, and B. R. Sekhar. Electronic structure of germanium selenide investigated using ultra-violet photoelectron spectroscopy. *Semicond. Sci. Technol.*, 30:075001:1–8, 2015.

[209] F. M. Gashimzade, D. G. Guliev, D. A. Guseinova, and V. Y. Shteinshrayber. Band-structure calculation for a_4b_6 layered crystals by the equivalent-orbit linear combination of atomic orbitals method. *J. Phys.: Condens. Matter*, 4:1081–1091, 1992.

[210] G. Valiukonis, F. M. Gashimzade, D. A. Guseinova, G. Krivaitė, A. M. Kulibekov, G. S. Orudzhev, and A. Šileika. Reflectance and thermoreflectance spectra and energy band structure of GeSe crystals. *Phys. Stat. Sol. (b)*, 117:81–92, 1983.

[211] G. Ciucci, A. Guarnieri, G.L. Masserini, and L. Quartapelle. Atomic pseudopotentials for orthorhombic IV-VI compounds. *Solid State Communications*, 29(2):75–80, jan 1979.

[212] L. Makinistian and E. A. Albanesi. *Ab initio* calculations of the electronic and optical properties of germanium selenide. *J. Phys.: Condens. Matter*, 19:186211:1–24, 2007.

[213] B. Chen, Y. Ruan, J. Li, W. Wang, X. Liu, H. Cai L. Yao, J.-M. Zhang, S. Chen, and G. Chen. Highly orientated gese thin film: self-assembly growth via the sandwiching post-annealing treatment and its solar cell performance. *Nanoscale*, 11:3968–3978, 2019.

[214] P. Ramasamy, D. Kwak, D. H. Lim, H. S. Ra, and J. S. Lee. Solution synthesis of GeS and GeSe nanosheets for high-sensitivity photodetectors. *J. Mater. Chem. C*, 4:479–4, 2016.

[215] A. M. Elkorashy. Photoconductivity in single-crystal germanium sulphide. *Journal of Physics: Condensed Matter*, 2(28):6195–6205, 1990.

[216] R. Eymard and A. Otto. Optical and electron-energy-loss spectroscopy of ges, gese, sns, and snse single crystals. *Physics Review B*, 16:1616–1623, 1977.

[217] A. V. Krukau, O. A. Vydrov, A. F. Izmaylov, and G. E. Scuseria. Influence of the exchange screening parameter on the performance of screened hybrid functionals. *The Journal of Chemical Physics*, 125(22):224106, 2006.

[218] J. M. Skelton. Transformer. `https://github.com/JMSkelton/Transformer`, 2018.

[219] T. Kotani, M. van Schilfgaarde, and S. V. Faleev. Quasiparticle self-consistent GW method: A basis for the independent-particle approximation. *Phys. Rev. B*, 76(16):165106:1–24, 2007.

[220] J. Buckeridge and D. O. Scanlon. Electronic band structure and optical properties of boron arsenide. *Phys. Rev. Mater.*, 3(5):051601:1–7, may 2019.

[221] B. Cunningham, M. Grüning, P. Azarhoosh, D. Pashov, and M. van Schilfgaarde. Effect of ladder diagrams on optical absorption spectra in a quasiparticle self-consistent GW framework. *Phys. Rev. Mater.*, 2(3):034603:1–12, mar 2018.

[222] H. Wiedemeier and P. A. Siemers. The thermal expansion and high temperature transformation of GeSe. *Zeitschrift für anorganische und allgemeine Chemie*, 411(1):90–96, 1975.

[223] H. Wiedemeier and P. A. Siemers. The temperature-composition phase diagram of the GeSe-GeTe system. In John L. Margrave, editor, *Modern High Temperature Science*, pages 395–408. Humana Press, 1984.

[224] F. O. von Rohr, H. Ji, F. A. Cevallos, T. Gao, N. P. Ong, and R. J. Cava. High-pressure synthesis and characterization of β-gese-a six-membered-ring semiconductor in an uncommon boat conformation. *Journal of American Chemical Society*, 139(7):2771–2777, 2017.

[225] P. A. E. Murgatroyd, M. J. Smiles, C. N. Savory, T. P. Shalvey, J. E. N. Swallow, N. Fleck, C. M. Robertson, F. Jäckel, J. Alaria, J. D. Major, D. O. Scanlon, and T. D. Veal. Gese: Optical spectroscopy and theoretical study of a van der Waals solar absorber. *Chemistry of Materials*, 32(7):3245–3253, 2020.

[226] B. B. Sharma and F. R. Chavada. Variation of lattice parameter with temperature and thermal expansion of the compound Cu_2SnSe_3. *physica status solidi (a)*, 14(2):639–642, 1972.

[227] B. Chen, Y. Ruan, J. Li, W. Wang, X. Liu, H. Cai, L. Yao, J.-M. Zhang, S. Chen, and G. Chen. Highly oriented GeSe thin film: self-assembly growth via the sandwiching post-annealing treatment and its solar cell performance. *Nanoscale*, 11:3968–3978, 2019.

[228] W. Zi, F. Mu, X. Lu, Y. Cao, Y. Xie, L. Fang, N. Cheng, Z. Zhao, and Z. Xiao. Post-annealing treatment of α-GeSe thin films for photovoltaic application. *Solar Energy*, 199:837–843, 2020.

[229] B. Chen, G. Chen, W. Wang, H. Cai, L. Yao, S. Chen, and Z. Huang. Magnetron sputtering deposition of GeSe thin films for solar cells. *Solar Energy*, 176:98–103, 2018.

[230] D.-J. Xue, S.-C. Liu, C.-M. Dai, S. Chen, C. He, L. Zhao, J.-S. Hu, and L.-J. Wan. GeSe thin-film solar cells fabricated by self-regulated rapid thermal sublimation. *Journal of the American Chemical Society*, 139(2):958–965, 2017.

[231] S.-C. Liu, Y. Yang, X. Zhang, L.-B. Huang, J.-K. Sun, B. Guan, X. Li, D.-J. Xue, and J.-S. Hu. Tuning the optical absorption property of GeSe thin films by annealing treatment. *physica status solidi (RRL) - Rapid Research Letters*, 12(12):1800370, 2018.

[232] S.-C. Liu, Y. Mi, D.-J. Xue, Y.-X. Chen, C. He, X. Liu, J.-S. Hu, and L.-J. Wan. Investigation of physical and electronic properties of GeSe for photovoltaic applications. *Advanced Electronic Materials*, 3(11):1700141, 2017.

[233] Y. P. Varshni. Temperature dependence of the energy gap in semiconductors. *Physica*, 34:149–154, 1967.

[234] A. Zanatta. Revisiting the optical bandgap of semiconductors and the proposal of a unified methodology to its determination. *Sci. Rep.*, 9:11225, 2019.

[235] M. Lingg, A. Spescha, S. G. Haass, R. Carron, S. Buecheler, and A. N. Tiwari. Structural and electronic properties of $CdTe_{1-x}Se_x$ films and their application in solar cells. *Science and Technology of Advanced Materials*, 19:683–692, 2018.

[236] D. E. Aspnes. Third-derivative modulation spectroscopy with low-field electroreflectance. *Surface Science*, 37:418–442, 1973.

[237] J. Karpinska. Basic principles and analytical application of derivative spectrophotometry. In Jamal Uddin, editor, *Macro To Nano Spectroscopy*, chapter 13. IntechOpen, Rijeka, 2012.

[238] B. K. Meyer, A. Polity, B. Farangis, Y. He, D. Hasselkamp, Th. Krämer, and C. Wang. Structural properties and bandgap bowing of $ZnO_{1-x}S_x$ thin films deposited by reactive sputtering. *Applied Physics Letters*, 85(21):4929–4931, 2004.

[239] N. Segercrantz, K. M. Yu, M. Ting, W. L. Sarney, S. P. Svensson, S. V. Novikov, C. T. Foxon, and W. Walukiewicz. Electronic band structure of highly mismatched $GaN_{1-x}Sb_x$ alloys in a broad composition range. *Applied Physics Letters*, 107(14):142104, 2015.

[240] J. M. Frost, K. T. Butler, F. Brivio, C. H. Hendon, M. van Schilfgaarde, and A. Walsh. Atomistic origins of high-performance in hybrid halide perovskite solar cells. *Nano Letters*, 14(5):2584–2590, 2014.

[241] W. Shockley and H. J. Queisser. Detailed balance limit of efficiency of *p-n* junction solar cells. *J. Appl. Phys.*, 32:510–519, 1961.

[242] J. D. Wiley, W. J. Buckel, W. Braun, G. W. Fehrenbach, F. J. Himpsel, and E. E. Koch. Reflectivity of single-crystal GeS from 0.1 to 30 eV. *Phys. Rev. B*, 14:697–701, 1976.

[243] A. Kosakov, H. Neumann, and G. Leonhardt. Investigation of the band structure of germanium chalcogenides by means of photoelectron spectroscopy. *Journal of Electron Spectroscopy and Related Phenomena*, 12(2):181 – 189, 1977.

[244] R. B. Shalvoy, G. B. Fisher, and P. J. Stiles. X-ray photoemission studies of the valence bands of nine IV-VI compounds. *Phys. Rev. B*, 15:2021–2024, 1977.

[245] P. C. Kemeny, J. Azoulay, M. Cardona, and L. Ley. Photoelectron spectra of GeS, GeSe, SnS and SnSe and their relation to structural trends and phase transitions within the average-valence-<5> compounds. *Il Nuovo Cimento*, 39B(2):709–714, 1977.

[246] G. D. Davis, P. E. Viljoen, and M. G. Lagally. Comparison of site-specific valence band densities of states determined from auger spectra and XPS-determined valence band spectra in GeS (001) and GeSe (001). *Journal of Electron Spectroscopy and Related Phenomena*, 21(2):135 – 152, 1980.

[247] S. Hino, T. Takahashi, and Y. Harada. Thermally induced effects in amorphous $GeSe_2$ and GeSe films studied by ultraviolet photoelectron spectroscopy. *Solid State Communications*, 35(4):379 – 382, 1980.

[248] E.P. O'Reilly, J. Robertson, and M.J. Kelly. The structure of amorphous GeSe and GeTe. *Solid State Communications*, 38(7):565 – 568, 1981.

[249] E. P. O. O'Reilly. The electronic structure of Ge-Se and Ge-Te compounds. *Journal of Physics C: Solid State Physics*, 15(7):1449–1455, 1982.

[250] T. Takahashi and T. Sagawa. Photoemission study of local structure of amorphous gese. *Journal of Non-Crystalline Solids*, 53(1):195 – 199, 1982.

[251] J. Robertson and Eoin P. O'reilly. The detection of chemical order in non-crystalline alloys from their valence *s* bands. *Philosophical Magazine B*, 47(6):621–626, 1983.

[252] T. Takahashi and T. Sagawa. Photoemission (UPS and XPS) study of local structures of amorphous GeTe and GeSe films. *Journal of Non-Crystalline Solids*, 59-60:879 – 882, 1983.

[253] F. M. Gashimzade, D. G. Guliev, D. A. Guseinova, and V. Y. Shteinshrayber. Band-structure calculation for a^4b^6 layered crystals by the equivalent-orbital linear combination of atomic orbitals method. *Journal of Physics: Condensed Matter*, 4(4):1081–1091, 1992.

[254] S. Hosokawa, Y. Hari, T. Kouchi, I. Ono, H. Sato, M. Taniguchi, A. Hiraya, Y. Takata, N. Kosugi, and M. Watanabe. Electronic structures and local atomic configurations in amorphous GeSe and GeTe. *Journal of Physics: Condensed Matter*, 10(8):1931–1950, 1998.

[255] F. R. McFeely, S. Kowalczyk, L. Ley, R. A. Pollak, and D. A. Shirley. High-resolution x-ray-photoemission spectra of PbS, PbSe, and PbTe valence bands. *Phys. Rev. B*, 7:5228–5237, 1973.

[256] M. Schlüter, G. Martinez, and M. L. Cohen. Electronic charge densities in PbSe and PbTe. *Phys. Rev. B*, 11:3808–3813, 1975.

[257] U. V. Waghmare, N. A. Spaldin, H. C. Kandpal, and Ram Seshadri. First-principles indicators of metallicity and cation off-centricity in the IV-VI rock-salt chalcogenides of divalent Ge, Sn, and Pb. *Phys. Rev. B*, 67:125111, 2003.

[258] D. I. Bletskan, K. E. Glukhov, and V. M. Kabatsii. Influence of cation vacancies and Bi impurity on the electronic structure and photoelectric properties of orthorhombic GeS. *Journal of Optoelectronics and Advanced Materials*, 21:629–640, 2019.

[259] X. Kong, J. Deng, L. Li, Y. Liu, X. Ding, J. Sun, and J. Z. Liu. Tunable auxetic properties in group-IV monochalcogenide monolayers. *Phys. Rev. B*, 98:184104, 2018.

[260] S. Jia, H. Li, T. Gotoh, C. Longeaud, B. Zhang, J. Lyu, S. Lv, M. Zhu, Z. Song, Q. Liu, J. Robertson, and M. Liu. Ultrahigh drive current and large selectivity in GeS selector. *Nat. Commun.*, 11:4636, 2020.

[261] J.-V. Raty and M. Wuttig. The interplay between Peierls distortions and metavalent bonding in IV-VI compounds: comparing GeTe with related monochalcogenides. *Journal of Physics D: Applied Physics*, 53(23):234002, 2020.

[262] L. Makinistian and E. A. Albanesi. Ab initio calculations of the electronic and optical properties of germanium selenide. *Journal of Physics: Condensed Matter*, 19(18):186211, 2007.

[263] P. Mishra, H. Lohani, A. K. Kundu, R. Patel, G. K. Solanki, K. S. R. Menon, and B. R. Sekhar. Electronic structure of germanium selenide investigated using ultra-violet photo-electron spectroscopy. *Semiconductor Science and Technology*, 30(7):075001, 2015.

[264] S. N. Dutta and G. A. Jeffrey. On the structure of germanium selenide and related binary IV/VI compounds. *Inorganic Chemistry*, 4(9):1363–1366, 1965.

[265] M. Sist, C. Gatti, P. Nørby, S. Cenedese, H. Kasai, K. Kato, and B. B. Iversen. High-temperature crystal structure and chemical bonding in thermoelectric

germanium selenide (GeSe). *Chemistry - A European Journal*, 23(28):6888–6895, 2017.

[266] A. Walsh. Principles of chemical bonding and band gap engineering in hybrid organic–inorganic halide perovskites. *The Journal of Physical Chemistry C*, 119(11):5755–5760, 2015.

[267] D. B. Mitzi. Synthesis, crystal structure, and optical and thermal properties of $(C_4H_9NH_3)_2MI_4$ (m = Ge, Sn, Pb). *Chemistry of Materials*, 8(3):791–800, 1996.

[268] D. H. Fabini, R. Seshadri, and M. G. Kanatzidis. The underappreciated lone pair in halide perovskites underpins their unusual properties. *MRS Bulletin*, 45(6):467–477, 2020.

[269] T. Krishnamoorthy, H. Ding, C. Yan, W. L. Leong, T. Baikie, Z. Zhang, M. Sherburne, S. Li, M. Asta, N. Mathews, and S. G. Mhaisalkar. Lead-free germanium iodide perovskite materials for photovoltaic applications. *J. Mater. Chem. A*, 3:23829–23832, 2015.

[270] G. Qing-Tian, P. Qi-Wei, S. Wei, S. Xun, and F. Chang-Shui. $CsGeCl_3$: A new ir nonlinear material. *Progress in Crystal Growth and Characterization of Materials*, 40(1):89–95, 2000.

[271] Q. Gu, Q. Pan, X. Wu, W. Shi, and C. Fang. Study on a new IR nonlinear optics crystal $CsGeCl_3$. *Journal of Crystal Growth*, 212(3):605–607, 2000.

[272] L. C. Tang, J. Y. Huang, C. S. Chang, M. H. Lee, and L. Q. Liu. New infrared nonlinear optical crystal $CsGeBr_3$: synthesis, structure and powder second-harmonic generation properties. *Journal of Physics: Condensed Matter*, 17(46):7275, 2005.

[273] L.-C. Tang, C.-S. Chang, L.-C. Tang, and J. Y. Huang. Electronic structure and optical properties of rhombohedral $CsGeI_3$ crystal. *Journal of Physics: Condensed Matter*, 12(43):9129–9143, 2000.

[274] Y.-Q. Zhao, L.-J. Wu, B. Liu, L.-Z. Wang, P.-B. He, and M.-Q. Cai. Tuning superior solar cell performance of carrier mobility and absorption in perovskite $CH_3NH_3GeCl_3$: A density functional calculations. *Journal of Power Sources*, 313:96–103, 2016.

[275] C. C. Stoumpos, L. Frazer, D. J. Clark, Y. S. Kim, S. H. Rhim, A. J. Freeman, J. B. Ketterson, J. I. Jang, and M. G. Kanatzidis. Hybrid germanium iodide perovskite semiconductors: Active lone pairs, structural distortions, direct and

indirect energy gaps, and strong nonlinear optical properties. *Journal of the American Chemical Society*, 137(21):6804–6819, 2015.

[276] D. S. Kyriakos and A. N. Anagnosopoulos. Electrical conductivity of layered gese related to extended faults. *J. Appl. Phys.*, 58:3917–3920, 1985.

[277] D. D. Vaughn, R. J. Patel, M. A. Hickner, and R. E. Schaak. Single-crystal colloidal nanosheets of GeS and GeSe. *J. Am. Chem. Soc.*, 132(43):15170–15172, 2010.

[278] N. S. Avasarala, B. Govoreanu, K. Opsomer, W. Devulder, S. Clima, C. Detavernier, M. van der Veen, J. Van Houdt, M. Henys, L. Goux, and G. S. Kar. Doped GeSe materials for selector applications. In *2017 47th European Solid-State Device Research Conference (ESSDERC)*, pages 168–171, 2017.

[279] Z. Shu and Y. Cai. Substitutional doped GeSe: tunable oxidative states with strain engineering. *J. Mater. Chem. C*, 8:13655–13667, 2020.

[280] S.-C. Liu, Y. Yang, Z. Li, D.-J. Xue, and J.-S. Hu. GeSe thin-film solar cells. *Mater. Chem. Front.*, 4:775–787, 2020.

[281] G. Shi and E. Kioupakis. Anisotropic spin transport and strong visible-light absorbance in few-layer SnSe and GeSe. *Nano Letters*, 15(10):6926–6931, 2015.

[282] C. Xia, J. Du, W. Xiong, Y. Jia, Z. Wei, and J. Li. A type-II GeSe/SnS heterobilayer with a suitable direct gap, superior optical absorption and broad spectrum for photovoltaic applications. *J. Mater. Chem. A*, 5:13400–13410, 2017.

[283] X. Lv, W. Wei, C. Mu, B. Huang, and Y. Dai. Two-dimensional GeSe for high performance thin-film solar cells. *J. Mater. Chem. A*, 6:5032–5039, 2018.

[284] Y. Mao, C. Xu, J. Yuan, and H. Zhao. A two-dimensional GeSe/SnSe heterostructure for high performance thin-film solar cells. *J. Mater. Chem. A*, 7:11265–11271, 2019.

[285] G.-J. Hou, D.-L. Wang, R. Ali, Y.-R. Zhou, Z.-G. Zhu, and G. Su. $CH_3NH_3PbI_3$/GeSe bilayer heterojunction solar cell with high performance. *Solar Energy*, 159:142–148, 2018.

[286] J. P. Perdew, A. Ruzsinszky, G. I. Csonka, O. A. Vydrov, G. E. Scuseria, L. A. Constantin, X. Zhou, and K. Burke. Restoring the density-gradient expansion for exchange in solids and surfaces. *Phys. Rev. Lett.*, 100:136406, 2008.

[287] M. J. Smiles, J. M. Skelton, H. Shiel, L. A. H. Jones, J. E. N. Swallow, H. J. Edwards, P. A. E. Murgatroyd, T. J. Featherstone, P. K. Thakur, T.-L. Lee, V. R. Dhanak, and T. D. Veal. Ge $4s^2$ lone pairs and band alignments in GeS and GeSe for photovoltaics. *J. Mater. Chem. A*, 9:22440–22452, 2021.

[288] R. B. Shalvoy, G. B. Fisher, and P. J. Stiles. Bond ionicity and structural stability of some average-valence-five materials studied by x-ray photoemission. *Phys. Rev. B*, 15:1680–1697, 1977.

[289] G. Hollinger, P. Kumurdjian, J.M. Mackowski, P. Pertosa, L. Porte, and Tran Minh Duc. Esca study of molecular $GeS_{3-x}Te_xAs_2$ glasses. *Journal of Electron Spectroscopy and Related Phenomena*, 5(1):237–245, 1974.

[290] U. Tokihiro. X-ray photoelectron and anger electron spectroscopic studies of chemical shifts in amorphous Ge-Se system. *Jap. J. Appl. Phys.*, 22(9):1349–1352, 1983.

[291] R. Li, W. Xia, Y. Guo, and J. Xue. Systematic investigation of electrical contact barriers between different electrode metals and layered GeSe. *Applied Physics Letters*, 114(1):013505, 2019.

[292] T. J. Whittles, L. A. Burton, J. M. Skelton, A. Walsh, T. D. Veal, and V. R. Dhanak. Band alignments, valence bands, and core levels in the tin sulfides SnS, SnS_2, and Sn_2S_3: Experiment and theory. *Chemistry of Materials*, 28(11):3718–3726, 2016.

[293] T. J. Whittles, T. D. Veal, C. N. Savory, A. W. Welch, F. W. de Souza Lucas, J. T. Gibbon, M. Birkett, R. J. Potter, D. O. Scanlon, A. Zakutayev, and V. R. Dhanak. Core levels, band alignments, and valence-band states in $CuSbS_2$ for solar cell applications. *ACS Applied Materials & Interfaces*, 9(48):41916–41926, 2017.

[294] H. S. Im, Y. Myung, Y. J. Cho, C. H. Kim, H. S. Kim, S. H. Back, C. S. Jung, D. M. Jang, Y. R. Lim, J. Park, and J.-P. Ahn. Facile phase and composition tuned synthesis of tin chalcogenide nanocrystals. *RSC Adv.*, 3:10349–10354, 2013.

[295] F. A. Rasmussen and K. S. Thygesen. Computational 2D Materials Database: Electronic Structure of Transition-Metal Dichalcogenides and Oxides. *The Journal of Physical Chemistry C*, 119(23):13169–13183, 2015.

[296] Y. Xu and M. A.A. Schoonen. The absolute energy positions of conduction and valence bands of selected semiconducting minerals. *American Mineralogist*, 85(3-4):543–556, 2000.

[297] O. S. Hutter, L. J. Phillips, K. Durose, and J. D. Major. 6.6% efficient antimony selenide solar cells using grain structure control and an organic contact layer. *Solar Energy Materials and Solar Cells*, 188:177–181, 2018.

[298] S. K. Vasheghani Farahani, T. D. Veal, J. J. Mudd, D. O. Scanlon, G. W. Watson, O. Bierwagen, M. E. White, J. S. Speck, and C. F. McConville. Valence-band density of states and surface electron accumulation in epitaxial SnO_2 films. *Phys. Rev. B*, 90:155413, 2014.

[299] S. Mandal, K. Haule, K. M. Rabe, and D. Vanderbilt. Systematic beyond-DFT study of binary transition metal oxides. *npj Computational Materials*, 5:2057–3960, 2019.

[300] L. Ley, R. A. Pollak, F. R. McFeely, S. P. Kowalczyk, and D. A. Shirley. Total valence-band densities of states of III-V and II-VI compounds from x-ray photoemission spectroscopy. *Phys. Rev. B*, 9:600–621, 1974.

[301] B. Silvi and A. Savin. Classification of chemical bonds based on topological analysis of electron localization functions. *Nature*, 371:683–686, 1994.

[302] G. Henkelman, A. Arnaldsson, and H. Jónsson. A fast and robust algorithm for bader decomposition of charge density. *Computational Materials Science*, 36(3):354–360, 2006.

[303] J. B. Mann, T. L. Meek, and L. C. Allen. Configuration energies of the main group elements. *Journal of the American Chemical Society*, 122(12):2780–2783, 2000.

[304] G. W. Watson, S. C. Parker, and G. Kresse. Ab initio calculation of the origin of the distortion of α-PbO. *Phys. Rev. B*, 59:8481–8486, 1999.

[305] A. Walsh and G. W. Watson. Influence of the anion on lone pair formation in Sn(II) monochalcogenides: A DFT study. *The Journal of Physical Chemistry B*, 109(40):18868–18875, 2005.

[306] J. J. Carey, J. P. Allen, D. O. Scanlon, and G. W. Watson. The electronic structure of the antimony chalcogenide series: Prospects for optoelectronic applications. *Journal of Solid State Chemistry*, 213:116–125, 2014.

[307] Y.-Q. Zhao, L.-J. Wu, B. Liu, L.-Z. Wang, P.-B. He, and M.-Q. Cai. Tuning superior solar cell performance of carrier mobility and absorption in perovskite $CH_3NH_3GeCl_3$: A density functional calculations. *Journal of Power Sources*, 313:96–103, 2016.

[308] P. Pyykko. Relativistic effects in structural chemistry. *Chemical Reviews*, 88(3):563–594, 1988.

[309] L. C. Allen. Electronegativity is the average one-electron energy of the valence-shell electrons in ground-state free atoms. *Journal of the American Chemical Society*, 111(25):9003–9014, 1989.

[310] T. D. Veal, L. F. J. Piper, M. R. Phillips, M. H. Zareie, Hai Lu, W. J. Schaff, and C. F. McConville. Scanning tunnelling spectroscopy of quantized electron accumulation at $In_xGa_{1-x}N$ surfaces. *physica status solidi (a)*, 203(1):85–92, 2006.

[311] H.R. Chandrasekhar and U. Zwick. Raman scattering and infrared reflectivity in GeSe. *Solid State Communications*, 18(11):1509–1513, 1976.

[312] Q. Fan, J. Yang, J. Cao, and C. Liu. Thermoelectric performances for both p- and n-type GeSe. *R. soc. open sci.*, 8:6, 2021.

[313] B. Yang, D.-J. Xue, M. Leng, J. Zhong, L. Wang, H. Song, Y. Zhou, and J. Tang. Hydrazine solution processed Sb_2S_3, Sb_2Se_3 and $Sb_2(S_{1-x}Se_x)_3$ film: molecular precursor identification, film fabrication and band gap tuning. *Scientific Reports*, 5:10978, 2015.

[314] Z. Xia, J. Zhong, M. Leng, L. Hu, D.-J. Xue, B. Yang, Y. Zhou, X. Liu, S. Qin, Y.-B. Cheng, and J. Tang. Generalized water-processed metal chalcogenide complexes: Synthesis and applications. *Chemistry of Materials*, 27(23):8048–8057, 2015.

[315] D. Y. Suarez-Sandoval, M. T. S. Nair, and P. K. Nair. Photoconductive antimony sulfide-selenide thin films produced by heating a chemically deposited Se-Sb_2Se_3 layer. *Journal of The Electrochemical Society*, 153(2):C91, 2006.

[316] Z. Deng, M. Mansuripur, and A. J. Muscat. Simple colloidal synthesis of single-crystal Sb-Se-S nanotubes with composition dependent band-gap energy in the near-infrared. *Nano Letters*, 9(5):2015–2020, 2009.

[317] S. Heimann, W. Assenmacher, O. Prymak, and S. Schulz. Synthesis of binary Sb_2E_3 (E = S, Se) and ternary $Sb_2(S,Se)_3$ nanowires using tailor-made single-source precursors. *European Journal of Inorganic Chemistry*, 2015(14):2407–2415, 2015.

[318] C. L. McCarthy, D. H. Webber, E. C. Schueller, and R. L. Brutchey. Solution-phase conversion of bulk metal oxides to metal chalcogenides using a sim-

ple thiol-amine solvent mixture. *Angewandte Chemie International Edition*, 54(29):8378–8381, 2015.

[319] P. K. Nair, G. Vázquez García, E. Anais Zamudio Medina, L. Guerrero Martínez, O. Leyva Castrejón, J. Moctezuma Ortiz, and M. T. S. Nair. Antimony sulfide-selenide thin film solar cells produced from stibnite mineral. *Thin Solid Films*, 645:305–311, 2018.

[320] M. D. Khan, S. U. Awan, C. Zequine, C. Zhang, R. K. Gupta, and N. Revaprasadu. Controlled synthesis of $Sb_2(S_{1-x}Se_x)3$ ($0 \leq x \leq 1$) solid solution and the effect of composition variation on electrocatalytic energy conversion and storage. *ACS Applied Energy Materials*, 3(2):1448–1460, 2020.

[321] M. Huang, Z. Cai, and S. Chen. Quasi-one-dimensional $Sb_2(S,Se)_3$ alloys as bandgap-tunable and defect-tolerant photocatalytic semiconductors. *The Journal of Chemical Physics*, 153(1):014703, 2020.

[322] W. Qiu, C. Zhang, S. Cheng, Q. Zheng, X. Yu, H. Jia, and B. Wu. The crystal structure, electronic structure and photoelectric properties of a novel solar cells absorber material $Sb_2Se_{3-x}S_x$. *Journal of Solid State Chemistry*, 271:339–345, 2019.

[323] G. P. Voutsas, A. G. Papazoglou, P. J. Rentzeperis, and D. Siapkas. The crystal structure of antimony selenide, Sb_2Se_3. *Zeitschrift für Kristallographie - Crystalline Materials*, 171(1-4):261–268, 1985.

[324] S. Messina, M. T. S. Nair, and P. K. Nair. All-chemically deposited solar cells with antimony sulfide-selenide/lead sulfide thin film absorbers. *MRS Online Proceedings Library*, 1012(1223), 2007.

[325] H. Deng, S. Yuan, X. Yang, J. Zhang, J. Khan, Y. Zhao, M. Ishaq, Wanneng Ye, Y.-B. Cheng, H. Song, and J. Tang. High-throughput method to deposit continuous composition spread $Sb_2(Se_xS_{1-x})_3$ thin film for photovoltaic application. *Progress in Photovoltaics: Research and Applications*, 26(4):281–290, 2018.

[326] Z. S. EL. Mandouh and S. N. Salama. Some physical properties of evaporated thin films of antimony trisulphide. *Journal of Materials Science*, 25:1715–1718, 1990.

[327] O. Savadogo and K. C. Mandal. Characterizations of antimony tri-sulfide chemically deposited with silicotungstic acid. *Journal of The Electrochemical Society*, 139(1):L16–L18, 1992.

[328] I. Grozdanov. A simple and low-cost technique for electroless deposition of chalcogenide thin films. *Semiconductor Science and Technology*, 9(6):1234–1241, 1994.

[329] M. Y. Versavel and J. A. Haber. Structural and optical properties of amorphous and crystalline antimony sulfide thin-films. *Thin Solid Films*, 515(18):7171–7176, 2007.

[330] M. Birkett, W. M. Linhart, J. Stoner, L. J. Phillips, K. Durose, J. Alaria, J. D. Major, R. Kudrawiec, and T. D. Veal. Band gap temperature-dependence of close-space sublimation grown Sb_2Se_3 by photo-reflectance. *APL Materials*, 6(8):084901, 2018.

[331] E. A. El-Sayad. Compositional dependence of the optical properties of amorphous $Sb_2Se_{3-x}S_x$ thin films. *Journal of Non-Crystalline Solids*, 354(32):3806–3811, 2008.

[332] B. Yang, S. Qin, D.-J. Xue, C. Chen, Y.-s. He, D. Niu, H. Huang, and J. Tang. In situ sulfurization to generate $Sb_2(Se_{1-x}S_x)_3$ alloyed films and their application for photovoltaics. *Progress in Photovoltaics: Research and Applications*, 25(1):113–122, 2017.

[333] T. Jimenéz, D. Seuret-Jimenéz, O. Vigil-Galán, M. A. Basurto-Pensado, and M. Courel. $Sb_2(S_{1-x}Se_x)_3$ solar cells: the impact of radiative and non-radiative loss mechanisms. *Journal of Physics D: Applied Physics*, 51(43):435501, 2018.

[334] Y. C. Choi, Y. H. Lee, S. H. Im, J. H. Noh, T. N. Mandal, W. S. Yang, and S. I. Seok. Efficient inorganic-organic heterojunction solar cells employing $Sb_2(S_x/Se_{1-x})_3$ graded-composition sensitizers. *Advanced Energy Materials*, 4(7):1301680, 2014.

[335] Y. Zhang, J. Li, G. Jiang, W. Liu, S. Yang, C. Zhu, and T. Chen. Selenium-graded $Sb_2(S_{1-x}Se_x)_3$ for planar heterojunction solar cell delivering a certified power conversion efficiency of 5.71%. *Solar RRL*, 1(5):1700017, 2017.

[336] O. A. Jaramillo-Quintero, M. E. Rincón, G. Vásquez-García, and P. K. Nair. Influence of the electron buffer layer on the photovoltaic performance of planar $Sb_2(S_xSe_{1-x})_3$ solar cells. *Progress in Photovoltaics: Research and Applications*, 26(9):709–717, 2018.

[337] W. Wang, G. Chen, Z. Wang, K. Wang, S. Chen, Z. Huang, X. Wang, T. Chen, C. Zhu, and X. Kong. Full-inorganic $Sb_2(S,Se)_3$ solar cells using carbon as both hole selection material and electrode. *Electrochimica Acta*, 290:457–464, 2018.

[338] L. Yao, L. Lin, H. Liu, F. Wu, J. Li, S. Chen, Z. Huang, and G. Chen. Front and back contact engineering for high-efficient and low-cost hydrothermal derived $Sb_2(S, Se)_3$ solar cells by using FTO/SnO_2 and carbon. *Journal of Materials Science & Technology*, 58:130–137, 2020.

[339] J. H. Rhee, C.-C. Chung, and E. W.-G. Diau. A perspective of mesoscopic solar cells based on metal chalcogenide quantum dots and organometal-halide perovskites. *NPG Asia Materials*, 5(e68), 2013.

[340] N. Guijarro, T. Lutz, T. Lana-Villarreal, F. O'Mahony, R. Gómez, and S. A. Haque. Toward antimony selenide sensitized solar cells: Efficient charge photogeneration at spiro-OMeTAD/Sb_2Se_3/metal oxide heterojunctions. *The Journal of Physical Chemistry Letters*, 3(10):1351–1356, 2012.

[341] C. E. Patrick and F. Giustino. Structural and electronic properties of semiconductor-sensitized solar-cell interfaces. *Advanced Functional Materials*, 21(24):4663–4667, 2011.

[342] C. Wu, L. Zhang, H. Ding, H. Ju, X. Jin, X. Wang, C. Zhu, and T. Chen. Direct solution deposition of device quality $Sb_2S_{3-x}Se_x$ films for high efficiency solar cells. *Solar Energy Materials and Solar Cells*, 183:52–58, 2018.

[343] M. Ishaq, H. Deng, S. Yuan, H. Zhang, J. Khan, U. Farooq, H. Song, and J. Tang. Efficient double buffer layer $Sb_2(Se_xS_{1-x})_3$ thin film solar cell via single source evaporation. *Solar RRL*, 2(10):1800144, 2018.

[344] J. Cheng, R. Hu, K. Wang, X. Meng, Y. Li, X. Yang, X. Liao, L. Li, and K. B. Chong. Air-stable solar cells with 0.7V open-circuit voltage using selenized antimony sulfide absorbers prepared by hydrazine-free solution method. *Solar RRL*, 3(5):1800346, 2019.

[345] C. Jiang, J. Yao, P. Huang, R. Tang, X. Wang, X. Lei, H. Zeng, S. Chang, H. Zhong, H. Yao, C. Zhu, and T. Chen. Perovskite quantum dots exhibiting strong hole extraction capability for efficient inorganic thin film solar cells. *Cell Reports Physical Science*, 1(1):100001, 2020.

[346] W. Han, D. Gao, R. Tang, Y. Ma, C. Jiang, G. Li, T. Chen, and C. Zhu. Efficient $Sb_2(S,Se)_3$ solar modules enabled by hydrothermal deposition. *Solar RRL*, 5(3):2000750, 2021.

[347] E. A. Kraut, R. W. Grant, J. R. Waldrop, and S. P. Kowalczyk. Precise determination of the valence-band edge in x-ray photoemission spectra: Application to measurement of semiconductor interface potentials. *Phys. Rev. Lett.*, 44:1620–1623, 1980.

[348] D. Coster and R. De L. Kronig. New type of auger effect and its influence on the x-ray spectrum. *Physica*, 2(1):13–24, 1935.

[349] N. Mårtensson and R. Nyholm. Electron spectroscopic determinations of M and N core-hole lifetimes for the elements Nb—Te (z=41-52). *Phys. Rev. B*, 24:7121–7134, 1981.

[350] J. Klimeš, D. R. Bowler, and A. Michaelides. Van der Waals density functionals applied to solids. *Phys. Rev. B*, 83:195131, 2011.

[351] M. J. Smiles, S Kavanagh, C. Don, L. A. H Jones, T. P. Shalvey, L. Thomas, J. E. N. Swallow, J. D. Major, D. O. Scanlon, A. Walsh, and T. D. Veal. Band gaps and band alignments of $Sb_2(S,Se)_3$. unpublished, 2022.

[352] M. J. Smiles, T. P. Shalvey, L. Thomas, T. D. C. Hobson, L. A. H. Jones, L. J. Phillips, C. Don, T. Beesley, P. K. Thakur, T.-L. Lee, K. Durose, J. D. Major, and T. D. Veal. GeSe photovoltaics: doping, interfacial layer and devices. *Faraday Discuss.*, 2022.

[353] A. Kyono, M. Kimata, M. Matsuhisa, Y. Miyashita, and K. Okamoto. Low-temperature crystal structures of stibnite implying orbital overlap of Sb $5s^2$ inert pair electrons. *Physics and Chemistry of Minerals*, 29(4):254–260, 2002.

[354] W. Mönch. *Electronic Properties of Semiconductor Interfaces*, page 263. Springer, 1986.

[355] W. Mönch. *Semiconductor Surfaces and Interfaces*, page 548. Springer, 1993.